UNIVERSITÀ DEGLI STUDI DI PADOVA

Dipartimento di Fisica e Astronomia "Galileo Galilei"

Corso di Dottorato di Ricerca in Astronomia

Ciclo XXXIV

Modelling Magnetic and Thermal Evolution of Neutron Stars: a 3D Approach

Coordinator: Ch.mo Prof. Giovanni Carraro
Supervisor: Ch.mo Prof. Roberto Turolla
Co-Supervisor: Dr. Roberto Taverna

PhD Student: Davide De Grandis

Contents

List of Figures

Symbols

Vectorial quantities are printed in **bold**.

t	time
$\boldsymbol{E}$	electric field
$\boldsymbol{B}$	magnetic field
$\boldsymbol{J}$	electric current density
T	absolute temperature
τ_H	Hall timescale (see Eq. 2.20)
τ_O	Ohm timescale (see Eq. 2.20)
π	Archimede's constant, $3.14159265\ldots$
c	speed of light in a vacuum, $2.997\,924\,58 \times 10^{10}\,\mathrm{cm\,s^{-1}}$
e	elementary charge, $4.803\,206\,8 \times 10^{-10}\,\mathrm{esu}$
h	Planck's constant, $6.626\,075\,5 \times 10^{-27}\,\mathrm{erg\,s}$
$\hbar$	reduced Planck's constant, $h/2\pi$
k_B	Boltzmann's constant, $1.380\,658 \times 10^{16}\,\mathrm{erg\,K^{-1}}$
σ_S	Stefan's constant, $5.670\,51 \times 10^{-5}\,\mathrm{erg\,cm^{-2}\,K^{-4}\,s^{-1}}$
$M_\odot$	solar mass, $1.99 \times 10^{33}\,\mathrm{g}$
$R_\odot$	solar radius, $6.96 \times 10^{5}\,\mathrm{km}$
(r, θ, ϕ)	spherical coordinate (radius, colatitude, azimuth)
ℓ, m	degree and order of the spherical harmonic Y_ℓ^m
PF	pulsed fraction, see Eq. 4.1

Acronyms

AXP	anomalous X-ray pulsar
BB	blackbody
(e)MHD	(electron) magneto-hydrodynamics
EoS	equation of state
f.o.r.	frame of reference
FRB	fast radio burst
GR	general relativity (or relativistic)
GRB	gamma ray burst
HPC	high performance computing
LOS	line of sight
MRI	magneto-rotational instability
NS	neutron star
PNS	proto neutron star
SGR	soft gamma repeater
X(D)INS	X-ray (dim) isolated neutron star

Abstract

Neutron Stars (NSs) are the final state in the life of massive stars and get formed in a supernova event, when the collapse of the progenitor core is halted by the pressure of degenerate neutrons. As such, they are characterised by extremely high densities, comparable to the ones found in atomic nuclei, making them the most compact objects with a surface known in the Universe. One of their most distinctive traits is their extremely strong magnetic field, ranging from $\approx 10^8$ to $\approx 10^{15}$ G, that makes them also the most powerful magnets in the Universe. NSs are most often revealed through their pulsed radio emission, but the (faint) surface thermal emission given off as the star cools down has now been detected in the soft X-rays from a number of sources. Thermal radiation carries a wealth of information, bearing directly on the determination of the star age and radius. The study of the thermal evolution of NSs is therefore key in understanding the physics of NSs and is inherently interwoven with that of the star magnetic field. In fact, not only the magnetic field decay heats up the star, but the heat and current transport coefficients depend on both the temperature and magnetic field themselves. This Thesis investigates models of the coupled magneto-thermal evolution of NSs, addressing for the first time both the secular evolution and short-term phenomena within a three-dimensional numerical framework. Different field configurations with varying degrees of symmetry are studied in the long term, highlighting the different observational signatures they give rise to. Conversely, the study of transient phenomena is focused on the outbursts observed in *magnetars*, the most magnetised NSs. These are episodes of sudden flux enhancement, up to 1000 times the quiescent level, which last for months/years and can repeat from the same source. Outbursts are modelled as the unfolding of an episode of fast heat injection in a small crustal region, which is by its own nature an asymmetric situation. The novelty and relevance of this 3D approach in the interpretation of observations and with respect to the previous ones found in the literature, which relied on symmetry assumptions to reduce the dimensionality of the problem, is discussed.

Riassunto

Le Stelle di Neutroni (NS) costituiscono lo stato finale della vita di stelle massive, e vengono prodotte quando il collasso di una supernova viene bloccato dalla pressione di degenerazione dei neutroni. Di conseguenza, esse sono caratterizzate da densità estremamente alte, comparabili a quelle dei nuclei atomici, che le rendono gli oggetti con superficie più compatti conosciuti nell'Universo. Uno dei tratti maggiormente distintivi è il loro campo magnetico estremamente intenso, $\approx 10^8$–10^{15} G, che le rende anche i magneti più forti nell'Universo. Le NS sono rilevate tipicamente tramite la loro emissione radio pulsata, ma le loro (debole) emissione termica nei raggi X soffici è stata osservata in diverse sorgenti. L'emissione termica porta una varietà di informazioni, connesse direttamente alla determinazione dell'età e raggio della stella. Lo studio dell'evoluzione termica è quindi fondamentale per comprendere la fisica delle NS ed è inoltre collegato strettamente al campo magnetico. Infatti, non solo il campo magnetico decadendo scalda la stella, ma le proprietà di trasporto termico ed elettrico dipendono sia dalla temperatura che dal campo magnetico. Questa Tesi illustra modelli di evoluzione magneto-termica di NS descrivendone sia l'evoluzione secolare che quella a breve termine con un approccio numerico tridimensionale. Diverse configurazioni magnetiche con varî livelli di simmetria verranno studiate su lunghi periodi, evidenziando le caratteristiche osservative associabili a ciascuna di esse. Viceversa, lo studio dei fenomeni transienti sarà concentrato sugli episodi di outburst osservati da parte di alcune magnetar, le NS con il campo magnetico più intenso. Essi sono episodi di rapido innalzamento del flusso termico, fino a 1000 volte il livello di quiescenza, che durano mesi/anni e possono ripetersi dalla stessa sorgente. Gli outburst verranno studiati come lo sviluppo di episodi di iniezione rapida di calore in una zona localizzata della crosta, una situazione per propria natura asimmetrica. La novità e rilevanza di questo approccio 3D sono discusse sia in relazione ai lavori presenti in letteratura, basati su assunzioni di simmetria per ridurre la dimensionalità del problema, che all'interpretazione delle osservazioni.

Acknowledgements

The completion of this Thesis could not have been possible without the direct and indirect support and guidance of many people, to whom goes my gratitude. I hope that this work reflects the diverse roles they each had in it.

First, I want to thank my Supervisors, Prof. Roberto Turolla and Dr. Roberto Taverna, who after supervising my Bachelor and Master Theses accepted to follow my work also for the PhD one—third time's a charm. Thanks to them, I did not only gain a set of highly-specialised knowledge, but even more importantly I picked up the skills of the trade of a scientist, which I hope to make my own.

I owe particular gratitude to Dr. Toby S. Wood, who brought the `PARODY` code into the realm of Astrophysics and then guided me into its mechanics, supporting me continuously in building up new science onto his previous efforts. I thank Prof. Silvia Zane for the many discussions and the thoughtful scrutiny that greatly improved my results. I am also grateful for the opportunity of working on research articles with Prof. Konstantinos N. Gourgouliatos, Prof. Sergei B. Popov, Dr. Sandro Mereghetti, Dr. Michela Rigoselli and Dr. Andrei P. Igoshev, from each of whom I could learn something important. A special though goes to my high-school physics teacher, Antonio Tegon, who showed me what the passion for physics and astronomy is; even though he is not here to read this work any more, his teachings are for sure in it.

This work is based on quite computationally-heavy codes, which were run at several facilities. I thank Prof. Francesco Ancillotto for granting me the access to `GOLLUM`, Prof. Michele Liguori for granting me the access to the project he leads on `CloudVeneto` and again Prof. Zane for the access to the facilities `MYRIAD@UCL` and `GRACE@UCL`. I also thank the support services associated to all these machines.

I thank my friends and colleagues with whom I shared the experience of the PhD in exceptionally challenging times. The sharing of our experience about physics, coding and just the life of a research student was instrumental in making it to the end goal.

Infine, ringrazio la mia Famiglia per il supporto che mi ha sempre mostrato, soprattutto in questi ultimi anni che ci hanno posto davanti a molte e diverse difficoltà, e per avermi permesso di investire in un percorso di studi così lungo in un àmbito così astratto, dandomi piena fiducia rispetto alle mie scelte di carriera.

Introduction

Neutron stars are the endpoint of the life of a star too small to inexorably collapse into a black hole but big enough to break the degeneracy pressure of electrons, supporting white dwarfs. They are, instead, supported by the degeneracy pressure of neutrons, and hence could be conceptualised as atomic nuclei with the size of a city. This means that they are at the same time intrinsically quantum and general-relativistic objects; moreover, they are characterised by extremely strong magnetic fields, that make them the strongest magnets in the universe.

Hence, studying neutron stars requires the knowledge of a very wide range of physical phenomena, which must then be related to the real world observations, with the impossibility of performing controlled experiments which is the curse and the blessing of all astrophysics.

In this context, the interpretation of NS data must come from the comparison with sound theoretical models of their evolution. In particular, the defining quantities of a NS are its magnetic field and temperature. The importance of studying NS cooling as a means of addressing the properties of matter in extreme conditions was realised long ago (Tsuruta and Cameron, 1966), whereas only more recently the importance of considering the evolution of the field alongside it has been assessed (e.g. Urpin and Yakovlev, 1980; Geppert and Wiebicke, 1991). Finally, thanks also to the development of numerical techniques and facilities, models of coupled magnetic and thermal evolution were produced (Aguilera et al., 2009; Viganò, 2013). Until few years ago, however, works in this field could be divided into two categories: those which considered the coupled problems, but under some symmetry assumptions that made the equations two-dimensional (Viganò, 2013) and those that were able to solve the evolution of the magnetic field only in 3D (Wood et al., 2014; Gourgouliatos et al., 2016). More recently, a tool to finally solve the complete problem in 3D has become available (De Grandis et al., 2020; Igoshev et al., 2020, 2021; De Grandis et al., 2021). This Thesis will present the efforts and some of the results obtained using this novel approach.

The material will be organised as follows: in Chapter 1, the basic physics of NSs will be reviewed; in Chapter 2 the equations of the magnetic and thermal evolution will be written out; Chapter 3 will present the numerical tools that were used to solve them, as well as the ray-tracing code that was used to convert the output of magnetothermal simulations to observables; Chapter 4 will be devoted to the study of long-term magnetothermal evolution, with a particular focus on the first millennia, when the Hall effect dominates

the evolution; Chapter 5 will describe cases of localised heating in the crust, that are used to model the transient activity of magnetars; conclusions follow in Chapter 6.

Journal Articles Related to this Thesis

The results presented in this Thesis are contained in the following journal articles:

Davide De Grandis, Roberto Turolla, Toby S. Wood, Silvia Zane, Roberto Taverna, and Konstantinos N. Gourgouliatos. Three-dimensional Modeling of the Magnetothermal Evolution of Neutron Stars: Method and Test Cases. ApJ, 903(1):40, November 2020. doi:10.3847/1538-4357/abb6f9

Davide De Grandis, Roberto Taverna, Roberto Turolla, Andrea Gnarini, Sergei B. Popov, Silvia Zane, and Toby S. Wood. X-Ray Emission from Isolated Neutron Stars Revisited: 3D Magnetothermal Simulations. ApJ, 914(2):118, June 2021. doi: 10.3847/1538-4357/abfdac

Davide De Grandis, Roberto Turolla, Roberto Taverna, Elisa Lucchetta, Toby S. Wood, and Silvia Zane. Three-Dimensional Magneto-Thermal Simulations of Magnetar Outbursts. *Submitted to ApJ*

CHAPTER 1

Neutron Stars

Neutron stars will be the main focus of this work, hence this first chapter will be devoted to a general introduction of these objects. After a historical account on their theorisation and discovery, the main characteristics of the various NS classes (the *NS zoo*) will be presented, to then reviewing the fundamental physics underlying them. Finally, the present observational efforts around NSs will be reviewed, with a particular focus on magnetars and their transient activity.

1.1 From theory to discovery: a historical introduction

Despite the fact that Astronomy is the oldest of all sciences, the idea that stars do evolve and die is a fairly recent one, as its origin is intertwined with that of modern physics. In fact, an understanding of atomic and nuclear physics has been key in solving a fundamental—even if sometimes overlooked—problem of physics at the turn of the 20th century: what is the power source of the stars, including our sun, and how long can it last for. With mounting biological and geological evidence setting the age of our solar system to at least several millions and then billions years, classical physics and chemistry were unable to provide a viable mechanism for sustaining such a huge energy emission for such a long time.

Optical spectroscopy, initiated in 1814 by J. Fraunhofer, had shown that stars are made of a plasma of light elements emitting thermal radiation; by the end of the century, hundreds of spectra had been collected, and several stellar *spectral types* were sorted out. The peculiar case of o_2 Eridani (Adams, 1914) seemed to go against all the knowledge gathered in this way: it was a very dim star (compared to its companion in a binary system) with the spectral characteristics of a hot, bright star. As several such objects were identified, they were identified as the new class of *white dwarfs*. This apparent contradiction was solved by Fowler (1926) and Chandrasekhar (1931) by using some very recent tools provided by quantum mechanics: white dwarfs were not formed by a regular plasma like other stars, but by a gas of completely degenerate electrons (the *Fermi sea*), which made them extraordinarily dense. They thus became the first class of compact

objects to be discovered.

In this context, the idea of an astrophysical object composed of nuclear matter, which will become renown as a Neutron Star, predates by some years the discovery of the neutron itself by J. Chadwick in 1932. In fact, in 1931 L. D. Landau proposed a model of stellar structure in which the core was formed by extremely dense nuclear matter, postulating in this region

> a violation of the law of energy, which law, as Bohr has first pointed out, is no longer valid in the relativistic quantum theory, when the laws of ordinary quantum mechanics break down

(Landau, 1932, see Yakovlev et al. 2013 for a complete historical account of Landau's role in NS physics) in order to explain stellar radiation. Later on, Landau revised this model ascribing the energy release to the neutronisation of matter accreting onto the compact core (Landau, 1938). This proved not to be the case, as the nuclear fusion mechanism was established, but it firmly introduced the idea of compact objects in scientific literature (and was later on revived as the yet to be discovered Thorne-Żytkow objects Thorne and Zytkow 1977).

Shortly thereafter, NSs were theorised independently by F. Zwicky as a means to explain a completely different, and not manifestly related, phenomenon: supernovæ. In a 1934 work jointly written with W. Baade—the very discoverer of supernovæ as a separate class of phenomena, (Baade and Zwicky, 1934)—he introduced stars mainly composed of degenerate neutrons as astrophysical bodies in their own right. This is the first instance in which the term *neutron star* has been used. Supernovæ were then viewed as the product of the transition of an ordinary star to a NS, even though the causes of such event were not identified.

Even though this intuition is nowadays viewed as correct in its essential traits, it was treated with a fair degree of scepticism, since it was built on speculative rather than quantitative grounds. The stability of nuclear matter on macroscopic scales was an open problem, lying at the boundaries of physics at that time. In fact, not only the details of the nuclear force on large scales were (and to some extant still remain) poorly understood, but the extreme compactness of the proposed neutron object was such that a complete general-relativistic treatment was needed. The task of bringing together quantum nuclear physics and GR was taken on by the work by R. C. Tolman, J. R. Oppenheimer and G. M. Volkoff (Tolman, 1939; Oppenheimer and Volkoff, 1939), who by formulating and solving their famous equation (see Eq. 1.22) proved that a cluster of cold neutrons can indeed be stable under its own gravity, and produce objects of few solar masses and radii of tens of kilometres. In a sense, this disproved Landau's theory: calculations proved that a neutron core was not a viable element of the structure of main sequence stars, including the Sun. In fact, they concluded that its huge gravity would reduce the overall stellar radius in a way that was just incompatible with observations. On the other hand, the phrase *neutron cores* is still exclusively used in their works, and no reference to Baade and Zwicky is given. This is largely an example of personal prejudices getting in the way of the development of science; yet, the test of time stood in favour of Baade and Zwicky's ideas.

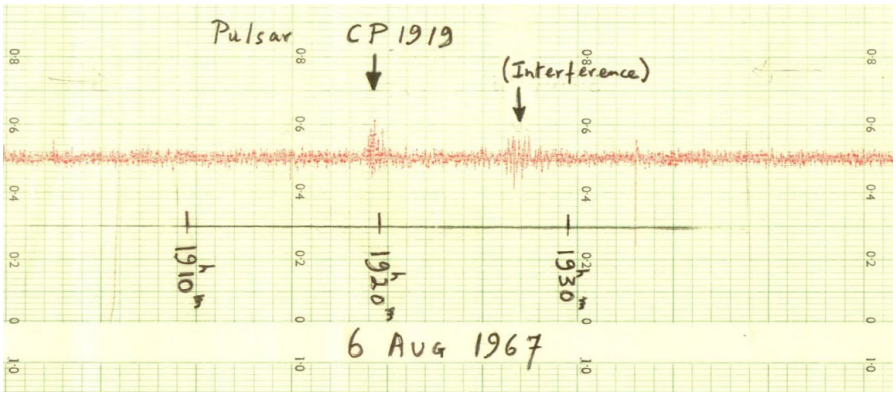

Figure 1.1: The first detection of a pulsar, obtained at Cambridge University by J. Bell. The pulsed nature of the source is not apparent here, yet, as it would have been observed later on in November 1967. Figure from `https://www.cam.ac.uk/stories/journeysofdiscovery-pulsars`, where an account of Bell's role and the controversy surrounding its recognition is given.

Before WWII and the subsequent Cold War diverted the attention of nuclear physicists to very different problems (just consider Oppenheimer's role as leader of the Manhattan project), one more piece of nuclear physics was to be linked to astrophysical phenomena. Neutrinos were theorised by W. Pauli in 1930 to explain the kinematics of β decay; in 1940, G. Gamow and M. Schoenberg realised their important role during a core collapse. In fact, in conditions of high density and temperature, energy is drained very quickly by the copious production of neutrinos through the URCA process (so dubbed paying homage to the eponymous Casino in Rio de Janeiro and its efficiency in draining gamblers' pockets). The efficiency of this process cast a doubt on the very possibility of forming a NS-like remnant, and was the object of the early NS thermal evolution studies. In the pioneering work by Tsuruta and Cameron (1966), the general traits of NS cooling were established, with the conclusion that neutrino cooling seemed so fast that only few very young objects were expected to be detectable. However, this was not entirely correct for at least two reasons: first, the URCA process is not the main cooling channel in most NSs; second, the most notable NS emission mechanism is not thermal (see later).

In the late 1950s and 1960s, new observations became available to finally unveil the existence of NSs in the physical universe. Zwicky's original idea of NSs as power sources for supernovæ found new pieces of evidence with the observations of the Crab Nebula, the remnant of the July 1054 supernova, as both a source of X-rays (e.g. Giacconi and Gursky, 1965) and of polarised light (Oort and Walraven, 1956), which also suggested the presence of a strong magnetic field (Shklovskii, 1953). To account for these discoveries, Wheeler (1966) and Pacini (1967) proposed a magnetised NS as the central object in SN remnants.

The final proof of the existence of NSs came from the other end of the electromagnetic spectrum, when in 1967 *radio pulsars* were discovered at Cambridge University (Hewish

et al., 1968, see Fig. 1.1). Quite interestingly, this very first paper linked the observed pulsating radio signal with a period of $\sim 1.3\,\mathrm{s}$ to compact objects, interpreting it as the result of the *radial* pulsations calculated by Meltzer and Thorne (1966). It was only a year later that Gold (1968) and Pacini (1968) introduced the idea of the "lighthouse effect". Again, fast rotation and strong magnetic fields were the key elements of the model, and they became the most prominent features associated to NSs alongside their high density.

1.2 Spin-down evolution

As already discussed, two of the most notable properties of a NS are its strong magnetisation and fast rotation. Taken together, they imply the presence of an accelerated electromagnetic field, which is known to radiate energy (e.g. Landau and Lifshitz, 1971).

In order to tackle this problem analytically, let us consider the classic model of a NS with a constant purely dipolar field with moment $\boldsymbol{\mathfrak{m}}$, whose axis forms an angle ξ with the rotation axis (e.g. Shapiro and Teukolsky, 1983). This does not actually imply a loss of generality[1]: only the dipolar component scales with distance slowly enough to be able to radiate energy to infinity. In a frame of reference where the vertical axis is parallel to the angular velocity $\boldsymbol{\Omega}$, the dipole moment can be written in cartesian coordinates as

$$\boldsymbol{\mathfrak{m}} = \frac{1}{2} B_d R_\star^3 \left(\sin\xi\, \sin\Omega t,\, \sin\xi\, \cos\Omega t, \cos\xi\right) \tag{1.1}$$

where B_d is the field strength at the poles, and $R_\star$ the radius of the NS. Then, the emitted energy is given by the Larmor formula,

$$\dot{E} = -\frac{2}{3c^2} \left|\ddot{\boldsymbol{\mathfrak{m}}}\right|^2 = -\frac{B_d^2 R_\star^6}{6c^3}\, \Omega^4\, \sin^2\xi \tag{1.2}$$

where the dot denotes time derivation and c is the speed of light. The energy emission hence depends on the rotation of the object and, therefore, originates from the loss of rotational kinetic energy. The expression in Eq. 1.2 must then be equated to the variation of rotational energy itself, $\dot{E}_{\mathrm{rot}} = I\Omega\dot{\Omega}$, where I is the NS moment of inertia. Rearranging this equation, one gets

$$\dot{\Omega} = -\frac{B_d^2 R_\star^6}{6Ic^3} \Omega^3 \sin^2\xi, \tag{1.3}$$

which, assuming that B_d, $R_\star$ and I are constant in time, can be integrated from $t = 0$ to the present time t, and rewritten as

$$t = \frac{1}{2} \frac{6Ic^3}{B_d^2 R_\star^6 \sin^2\xi\, \Omega^2(t)} \left(1 - \frac{\Omega^2(t)}{\Omega^2(0)}\right) \approx \frac{1}{2} \frac{6Ic^3}{B_d^2 R_\star^6 \sin^2\xi\, \Omega^2(t)} \tag{1.4}$$

[1] At least, as long as the star is considered to be *in vacuo*.

where the approximated relation holds for $\Omega(0) \gg \Omega(t)$. Plugging Eq. 1.3 back into this expression, one gets as an estimate of the elapsed time

$$t = -\frac{1}{2}\frac{\Omega}{\dot{\Omega}} = \frac{1}{2}\frac{P}{\dot{P}}, \tag{1.5}$$

where the period $P = 2\pi/\Omega$ was introduced, since it is the quantity which is directly measured. This simple expression is often used as a first gauge for the age of a NS, and is known as the *characteristic age*. For example, Groth (1975) found a characteristic age $t = 1243\,\mathrm{yr}$ for the Crab pulsar using data from 1972, i.e., 918 years after the SN explosion.

Introducing again the period, Eq. 1.3 can be rewritten as

$$P\dot{P} = \frac{4\pi^2 B_d^2 R_\star^6 \sin^2\xi}{6Ic^3}, \tag{1.6}$$

so that the field can be expressed in terms of observables as

$$B_d = \sqrt{\frac{6Ic^3}{4\pi^2 R_\star^6 \sin^2\xi} P\dot{P}} \approx 3.2 \times 10^{19}\sqrt{P\dot{P}}\,\mathrm{G} \tag{1.7}$$

where the numerical value has been obtained for the characteristic values $I \approx 10^{45}\,\mathrm{g\,cm^2}$, $R_\star \approx 10\,\mathrm{km}$, $\sin\xi \approx 1$ and for P measured in seconds. This is the so-called *spin-down field*, which serves as a first estimate of the magnetisation of a NS.

1.3 The $P\dot{P}$ diagram and the NS zoo

Since such important parameters as the age and magnetisation of a NS can be inferred (at least to a first approximation) from the period and its time derivative, a very natural idea is to represent NSs in the $P\dot{P}$ *diagram*, shown in Fig. 1.2. This is actually one of the most useful tools in NS physics, and is to a certain degree akin to the H-R diagram of stellar astronomy. In fact, several classes of NSs can be singled out in different regions of the diagram, the most important being:

radio pulsars by far the most represented category, filling the central part of the diagram with periods of 0.1–1 s and typical fields of $\approx 10^{12}\,\mathrm{G}$. They are mostly noted for their pulsed radio activity, although many are visible in other bands (mainly X- and γ-rays) as well (see e.g. Manchester et al., 2005);

magnetars found in the top right corner, implying strong spin-down field ($\gtrsim 10^{13}\,\mathrm{G}$) and young ($\approx$ kyr) age. They are bright in the X-rays and show transient activity in the form of high energy bursts and outbursts (see Sec. 1.4.1). These phenomena are thought to be powered by the fast dissipation of their strong magnetic field; this idea is corroborated by the discovery of the so-called *low-field magnetars*, sources with a dipole field in the PSR range but which show magnetar-like activity, powered by a strong field possibly hidden inside the crust and/or dominated by non-radiative multipoles (see e.g. Turolla et al., 2015; Kaspi and Beloborodov, 2017);

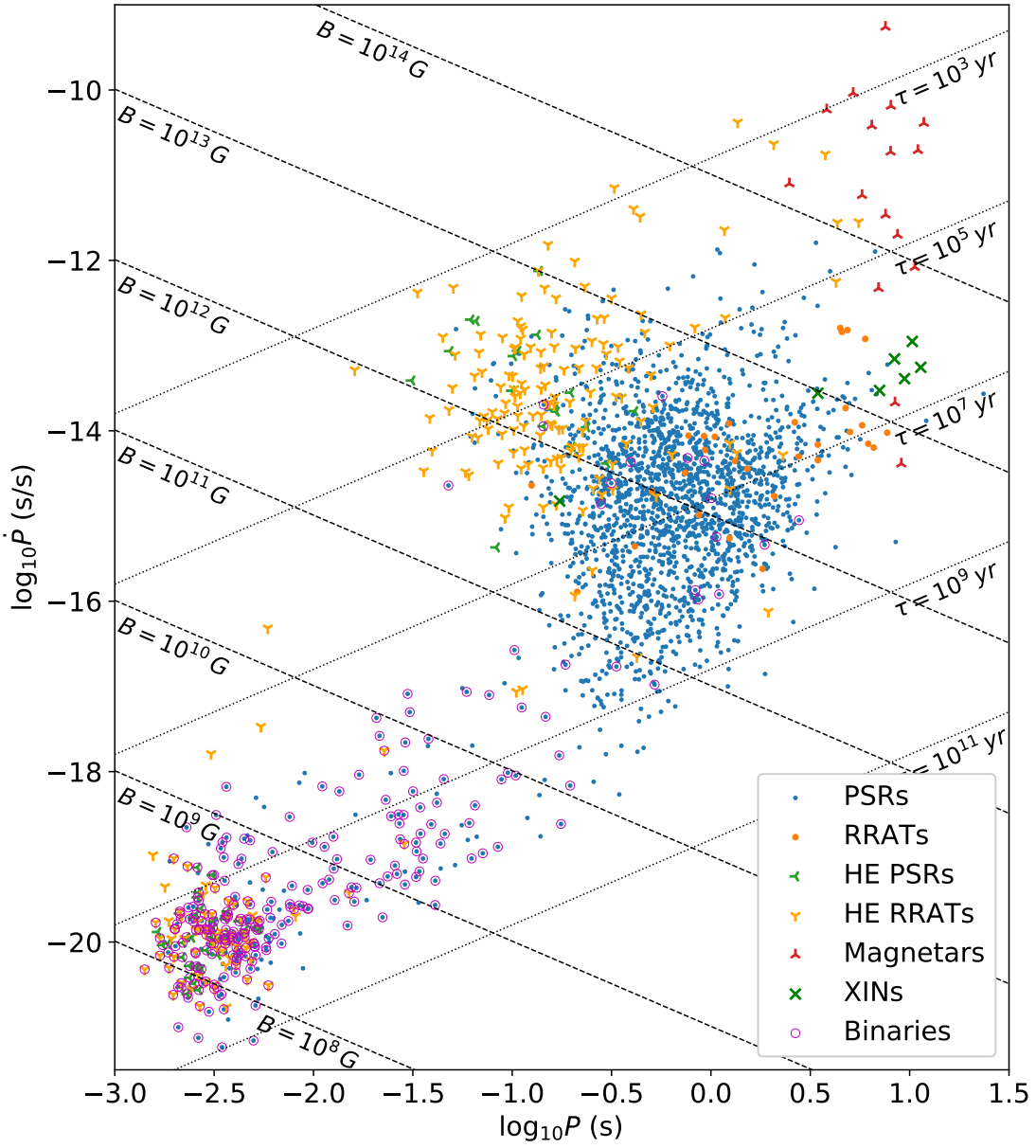

Figure 1.2: The $P\dot{P}$ diagram for the known NSs (data from the Australian Telescope National Facility Catalogue `https://www.atnf.csiro.au/research/pulsar/psrcat/expert.html`). The labels refer to the observational properties of the sources (PSRs=pulsars, RRATs= rotating radio transients, HE=high energy, XINs=X-ray isolated NSs); see Sec. 1.4.1 for a description of Magnetars; the purple circles indicate that the NS is part of a binary sistem. The dotted (dashed) lines are the loci of constant characteristic age (spin down field).

millisecond pulsars found in the bottom left part of the diagram, corresponding to short periods and low (by NS standards) fields $\approx 10^8$ G. The origin of the fast rotation lies in the spin-up by accretion from a companion star, to which they are almost always associated in a low mass X-ray binary. For this reason, they are dubbed *recycled pulsars* (see e.g. Patruno and Watts, 2021);

RRATs (rotating radio transients) emitting sporadic bright pulsar-like radio signals in a very irregular fashion, from which an underlying periodicity (and hence field estimate) can be nonetheless inferred (see e.g. McLaughlin et al., 2006);

XINs (X-ray isolated NSs) are a small class of isolated objects (so far seven of them are known, hence the nickname *magnificent seven*) which do not exhibit any radio emission and emit thermal X-rays; some optical counterparts are known. It has been suggested that they are old magnetars (see e.g. Turolla (2009) and Sec. 4.1.1);

CCOs (central compact objects) found at the centre of a SN remnant. They have quite low ($\lesssim 10^{11}$ G) dipolar magnetic fields, which is usually explained in terms of a burial of the field by the abundant accretion of SN debris (see e.g. De Luca, 2017).

This phenomenology, so variegated as to be called the *NS zoo*, posed the problem of whether, and to which extent, different classes of NSs are connected by evolutionary links. The current estimates of the SN rate in the Galaxy seem to be too low to explain the number of observed NSs, so that evolutionary links between different NS population, relying on mechanisms that are also able to significantly alter age estimates, are expected (e.g. Popov et al., 2006). This theoretical framework is the so-called *Grand Unification of NSs*, which is far to have been reached as yet. The study of magnetothermal evolution of NSs under different conditions plays a crucial role towards this goal (Viganò, 2013; Pons and Viganò, 2019).

1.4 Observing Neutron Stars

Radio emission remains to the present day the main mechanism through which most NSs are observed, with the bulk of them being part of the *radio pulsar* (PSR) class (see Sec. 1.3). In the past decades, radio telescopes all around the world have detected thousands of PSRs (see e.g. the catalogue at `https://www.atnf.csiro.au/research/pulsar/psrcat/`, Manchester et al. 2005, which to date contains 3282 objects), yet the interest in this topic is far from waning. The unique timing consistency of pulsars makes them extremely precise cosmic clocks, the ideal targets to test GR in a strong-field environment (e.g. Kramer et al., 2004), and even serve as detectors of gravitational waves when observed by a PTA (pulsar timing array, Hobbs et al. 2010).

In the light of this, it may come as a surprise that the exact mechanisms behind NS radio emission are still poorly understood (see e.g. Melrose, 2017). This not only amounts to a theoretical problem *per se*, but poses issues for the interpretation of new radio data.

The most prominent example is the current mystery surrounding *fast radio bursts* (FRBs Petroff et al., 2019), bright fast radio signals that have been linked to strongly magnetised NSs (e.g. Mereghetti et al., 2020) but still elude a convincing theoretical framework for their origin.

Nonetheless, there is more to NS emission than the radio band. In particular, many NSs are bright at high-energy end of the electromagnetic spectrum. Their thermal emission falls in the X-ray band, and is studied by means of satellite-based missions such as *Chandra* (Weisskopf et al., 2002), *XXM-Newton* (Jansen et al., 2001), *INTEGRAL* (van den Heuvel et al., 2021), *NICER* (Gendreau and Arzoumanian, 2017) and the upcoming missions *ATHENA* (Padovani et al., 2017) and *IXPE* (which in the very nearby future will add polarimetric capabilities to the spectroscopic ones, Weisskopf et al. 2016). X-rays are particularly important since the thermal emission gives almost direct information about the temperature at NS surfaces, and can in principle directly constrain the length of NS radii. Even harder radiation is detected by γ-ray missions like *Fermi* (Abdollahi et al., 2020) and ground-based Cherenkov telescopes like *MAGIC* (Aleksić et al., 2016), typically forming power-law tails formed by scattering processes in the magnetosphere.

Moreover, some objects show emission in the optical band—faint, yet detectable from ground based telescopes— and in the IR one. These can be produces as the tail of the thermal emission, or come from different mechanisms which are not well understood.

It is finally worth mentioning the paramount role of NSs in the dawning era of multimessenger astrophysics: it was the merging of two NSs that give rise to the first, and to date most spectacular, multimessenger event ever observed, GW-GRB 170817 (Abbott et al., 2017), in which the GW interferometers of the *LIGO-VIRGO* collaboration worked with almost every piece of more traditional astronomical instrumentation available to study the event in all the electromagnetic wavelengths. BH-NS and other NS-NS mergers are at the core of the science of present and next-generation ground based GW detectors, and continuous GW emission from deformed NSs is one of the targets of *LISA*. Neutron stars are also copious sources of neutrinos, which are one of the future targets for neutrino telescopes as *ICECUBE* (Ghadimi and Santander, 2021).

1.4.1 Transient Activity in Magnetars

Alongside their persistent emission, some NSs exhibit short term variations of their spectral and timing properties. Examples of these events are pulsar glitches (e.g. Manchester, 2018), the short radio pulses from RRATs and magnetar activity. In view of the phenomenology that will be further addressed in this work, this section will describe in some detail the activity from the latter class.

The very idea of ultra-magnetised objects was put forward in the 1990s (Thompson and Duncan, 1993) in order to explain the activity of soft gamma repeaters (SGRs), objects identified as the sources of bursts in the hard-X/soft-γ band that were at first linked to GRBs. As observations progressed, this paradigm was extended to another class of very energetic objects, anomalous X-ray pulsars (AXPs). Like ordinary pulsars, these NS emit thermally in the soft-X band, but with a much larger luminosity (10^{34}–$10^{36}\,\mathrm{erg\,s^{-1}}$). By

the 2000s, the fact that the two classes were different manifestation of a single kind of NS, characterised by an ultra-strong magnetic field, became widely accepted (e.g. Kaspi, 2003). In particular, short bursts were detected from already known AXPs, and measurements of the thermal luminosity of SGRs gave values in the same range of those of AXPs (Thompson, 2001, and references therein). Moreover, the pulsation time was observed to be quite long ($\approx$ 2–12 s), with a large period time derivative ($\approx 10^{-13}$–$10^{-11}\,\mathrm{s\,s^{-1}}$), placing the objects from both classes in the same region of the $P\dot{P}$ diagram, on the upper right, and directly suggesting the presence of extremely strong dipolar fields, 10^{13}–10^{15} G.

To this day, the most characteristic trait of magnetars remains their transient activity, which is also the way in which most of them are discovered. Broadly speaking, two well distinct types of transient phenomena can be identified:

Bursts rather short events (ranging from fractions to tens of seconds) of enhanced activity in the X- and γ-bands. They seldom come as one-off events, with most sources going between periods of intense repeated activity (to the point of emitting *burst storms* or *forests*, Israel et al. 2008) and periods of quiescence of up to several years. They can be further divided into:

- **Short bursts** lasting up to ~ 1 s with peak luminosity of 10^{39}–$10^{41}\,\mathrm{erg\,s^{-1}}$, are the most common; they have soft thermal spectra, but show no clear trends in the shapes of their lightcurves;
- **Intermediate bursts** lasting up to ~ 40 s, with peak luminosities of 10^{41}–$10^{43}\,\mathrm{erg\,s^{-1}}$. They are to some extent an up-scaled version of short bursts, but sometimes show slower decays, with a very variegated phenomenology;
- **Giant flares** exceptionally rare events (only three have been observed to date, each from a different object, with a fourth candidate being recently discovered Castro-Tirado et al. 2021) of extremely high energy output ($\approx 10^{44}$–10^{47} erg). They peak in less than a second, to then decay in several minutes.

Transient Magnetar Outbursts events in which a previously dim object enters a phase of enhanced X-ray flux, with a $\approx$ 100–1000$\times$ enhancement. Their rise time is of some hours, with a total duration of ≈ 1 yr. Such events were observed 23 times from 17 sources (see Fig. 1.3) from 2002 onwards (Ibrahim et al., 2004) and show a spectrum that is interpreted as one or more thermal components, with often a hard power-law tail. Since the hot thermal emission is observed to have a small radius $\lesssim 1$ km, these events are generally interpreted as the unfolding of the injection of a large quantity of heat in a small zone in the outer crust, which is probably of magnetic origin. An updated archive of the known outbursts can be found at `http://magnetars.ice.csic.es` (Coti Zelati et al., 2018)

Even though the exact mechanisms behind these phenomena are still debated, they are all thought to involve some kind of magnetic energy dissipation or at the very least to be magnetically driven. In this work, a particular focus will be given to the phenomenology of outbursts; in fact, they are thought to happen in NS crusts, making them the ideal study case for a magnetothermal code.

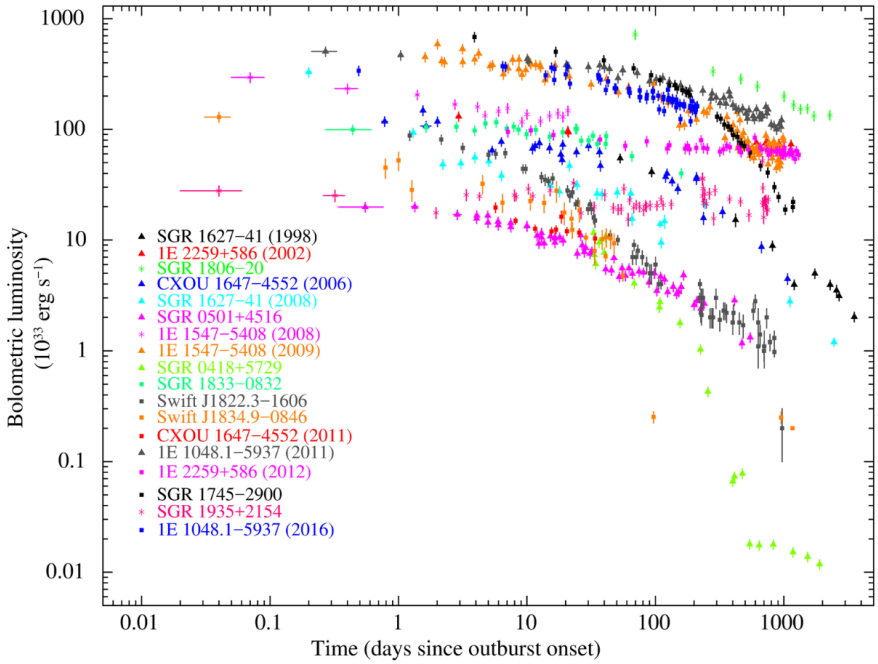

Figure 1.3: Lightcurves of the known magnetar outbursts up to 2018 (figure reproduced from Coti Zelati et al. 2018).

1.5 The Internal Structure

Notwithstanding their name, neutron stars are not entirely made of neutrons, which nevertheless are their main constituent. The exact structure of a NS depends on the properties of nuclear forces on macroscopic scales, a largely uncharted territory since ground based experiments can probe systems with at most hundreds of nucleons; this includes the thermodynamical stability of exotic phases of matter and the transition between them. As a general picture the structure of a NS can be divided in different layers as follows (e.g. Haensel et al., 2007):

atmosphere a thin (few cm) layer of gas, which however has a quite significant optical depth. It may be composed of metals (mostly iron peak elements), or H and He if the object underwent accretion. The very presence of an atmosphere is not certain in all cases: in highly magnetised, relatively cold objects, a gaseous state may not be stable and turn to a condensate surface (e.g. Potekhin et al., 2012);

ocean comprising the low density ($\lesssim 10^9\,\mathrm{g\,cm^{-3}}$) liquid layers. It is the layer where the highest radial gradients of temperature and density are found;

crust a layer composed of highly degenerate electrons embedded in a Coulomb crystal of metal nuclei, extending from the solidification of the ocean, which at typical NS temperatures happens at densities of the order of $\approx 10^9\,\mathrm{g\,cm^{-3}}$, up to $\approx 10^{14}\,\mathrm{g\,cm^{-3}}$.

As the density increases with depth, nuclei get more and more neutron rich, to the point that neutrons start to drip from nuclei; the corresponding *neutron drip density*, $\approx 4.3 \times 10^{11}\,\mathrm{g\,cm^{-3}}$, is taken to define the boundary between outer and inner crust. The crust extends for a depth of $\approx 1\,\mathrm{km}$, and contains $\approx 1\%$ of the total mass;

mantle the existence of a transition region between the solid crust and the liquid nucleon core is not certain. As nuclei grow more and more neutron rich it has been proposed that they may form mesoscopic structures of various shapes (the so-called *nuclear pasta*: rod-like spaghetti, flat lasagnas…), with highly anisotropic and peculiar properties (Ravenhall et al., 1983). The thermodynamical stability of such a phase is however uncertain;

outer core with a radius of $\approx 10\,\mathrm{km}$, it accounts for most of the NS mass. It is composed of a plasma of neutrons, protons, electrons and (in the innermost regions) muons ($npe\mu$ matter). It is believed to be in a superfluid/superconducting state for most of a NS life (see Sec. 3.1), and is able to act as a reservoir of thermal energy and angular momentum;

inner core in the innermost regions ($\lesssim 1\,\mathrm{km}$ from the centre, $\rho \gtrsim 10^{15}\,\mathrm{g\,cm^{-3}}$), the behaviour of matter is not known in detail. Under such conditions, the transition to exotic states may become possible, with the appearance of hyperons ($\Delta, \sigma^{\pm}, \Lambda^{\pm}$…) or even a quark-gluon plasma.

Since the bulk of the mass resides in the outer core, one can think of a NS as a huge atomic nucleus. To have a quantitative idea of the merit of this image, let us use the Weizsäcker semi-empirical formula for the binding energy B of a nucleus with Z protons and N neutrons (i.e., mass number $A = N + Z$),

$$B(N,Z) = a_{\mathrm{vol}}A - a_{\mathrm{surf}}A^{2/3} - a_{\mathrm{sym}}\frac{(N-Z)^2}{A} - a_{\mathrm{coul}}\frac{Z(Z-1)}{A^{1/3}} - \delta(N,Z) + \frac{3}{5}\frac{GM^2}{r_0 A^{1/3}} \quad (1.8)$$

where the coefficients are calculated by fitting the known nuclei, δ is a pairing term proportional to an empirically determined power of A and the last term describes the classical binding gravitational energy for a spherical body, having expressed the radius of a nucleus as $R = r_0 A^{1/3}$ with $r_0 = 1.2\,\mathrm{fm}$ (e.g. Bertulani, 2007). A nucleus will be gravitationally bound when the last term balances out the other ones. In the case of a large neutron rich "nucleus", $A \gg Z \gg 1$, we can only keep the first and third terms, yielding the relation between mass and neutron number,

$$A^{2/3} \approx \sqrt{\frac{3}{5}\frac{G}{r_0(a_{\mathrm{sym}} - a_{\mathrm{vol}})}}M. \quad (1.9)$$

For a reference value $M = 1.4M_{\odot}$, this gives $A \approx 10^{58}$, $R_{\star} = r_0 A^{1/3} \approx 30\,\mathrm{km}$. This radius is about double of what is predicted by accurate models and measured in the (few) observations, but this can still be viewed as a good result, considering that an

extrapolation by almost 60 orders of magnitude of 1930s results has been made. Many more details must be taken into account; first and foremost, the degeneracy of neutrons, which will be quickly reviewed in the next section.

1.5.1 Completely degenerate Fermi gases

In this section, the fundamental properties of degenerate systems of fermions are reviewed; this gives some hints about the composition of the nucleus, but will become useful also in the description of degenerate electrons in the crust, which will be at the core of the description of the crustal evolution equations in Ch. 2.

In the grand canonical ensemble, the thermodynamic potential of a system of N particles with internal energy U, entropy S, chemical potential μ at temperature T is given by (Landau and Lifshitz, 1969)

$$\Omega := U - TS - \mu N = -k_B T \log \sum_k \left[\exp(\mu - E_k)/k_B T\right]^{n_k} \tag{1.10}$$

where n_k denotes the number of particles in the k-th state with energy E_k.

The Pauli exclusion principle for fermion systems states that n_k can only take up the two values 0 and 1, so that

$$\Omega_k = -k_B T \log \left[1 + e^{(\mu - E_k)/k_B T}\right], \tag{1.11}$$

whence the average number of particles is found as

$$\bar{n}_k = -\frac{\partial \Omega}{\partial \mu} = \frac{1}{e^{(E_k - \mu)/k_B T} + 1} \tag{1.12}$$

which defines the *Fermi-Dirac* distribution. The total thermodynamic potential of the gas is found by summing Ω_k over all the possible states. In the limit $T \to 0$, this becomes a step function with value 1 below the threshold $E = \mu$, which is also known as the *Fermi energy* E_F. The normalisation of the distribution is provided by the total number of particles N, in a volume V. This normalisation on the $T = 0$ distribution can be imposed considering a large number of states, so that in the continuum limit one can integrate in the momentum space: the number of particles with momenta between p and $p + \mathrm{d}p$ is

$$2 \cdot \frac{4\pi p^2}{(2\pi\hbar)^3} V \mathrm{d}p \tag{1.13}$$

where we add the further factor 2 to account for spin degeneracy for spin 1/2 particles. Then, in the case of a step-like distribution the total number is

$$N = \frac{V}{\pi^2 \hbar^3} \int_0^{p_F} p^2 \mathrm{d}p = \frac{V p_F^3}{3\pi^2 \hbar^3} \tag{1.14}$$

where the *Fermi momentum* p_F is the one associated to the Fermi energy. This allows to write the relation

$$p_F = (3\pi^2)^{1/3} \hbar \, n^{1/3}, \tag{1.15}$$

where the number density $n = N/V$ was introduced. The Fermi energy is then found by specifying the dispersion relation,

$$E_F = \mu = mc^2\sqrt{1+\left(\frac{p_F}{mc}\right)^2} = \begin{cases} mc^2 + \frac{p_F^2}{2m} & \propto n^{2/3} \quad (\textit{non-relativistic}) \\ c\,p_F & \propto n^{1/3} \quad (\textit{ultra-relativistic}). \end{cases} \tag{1.16}$$

At finite temperature, the distribution is not a step function, but the exponential behaviour makes so that the difference is notable only for energies that are $\approx k_B T$ apart from E_F. To this end, it is useful to define a *Fermi temperature*,

$$T_F = \frac{E_F}{k_b}, \tag{1.17}$$

so that a gas can be treated as completely degenerate if it is cold enough, $T \ll T_F$. NSs are quite hot for terrestrial and even stellar standards, with temperatures $10^6\,\mathrm{K} \lesssim T \lesssim 10^9\,\mathrm{K}$, yet their density is so huge that the Fermi temperature turns out to be $T_F \approx 10^{12}\,\mathrm{K}$; hence, a NS can be safely considered *cold* from a quantum mechanical perspective and treated as a completely degenerate system.

1.5.2 The TOV equation and the Mass-Radius relation

The structure of a NS is ultimately determined by the equation of state of ultradense matter and the hydrostatic equilibrium condition. As already discussed, the latter requires to go beyond standard stellar models, considering the effects of general relativity: the equilibrium configuration is a solution of Einstein equations,

$$R_{\mu\nu} - \frac{1}{2}Rg_{\mu\nu} = \frac{8\pi G}{c^4}T_{\mu\nu}, \tag{1.18}$$

where $R_{\mu\nu}$ is the Ricci tensor, whose contraction is the Ricci scalar $R = R^\mu_\mu$, $g_{\mu\nu}$ is the metric and $T_{\mu\nu}$ is the stress-energy tensor. The enormous gravity of a NS makes so that they are to extremely good approximation spherically symmetric; moreover, even though they spin fast, their specific angular momentum is quite low, $(J/Mc)/(GM/c^2) \simeq 4\times10^{-4}(P/1\,\mathrm{s})^{-1}(M/M_\odot)^{-1}(R/10\,\mathrm{km})^2$, and other possible asphericity sources, such as magnetic deformations, are very small. Hence, the spacetime in which a NS is embedded resembles a Schwarzschild solution, which in spherical coordinates reads

$$\mathrm{d}s^2 = -B(r,t)\,\mathrm{d}t^2 + A(r,t)\,\mathrm{d}r^2 + r^2(\mathrm{d}\theta^2 + \sin^2\theta\,\mathrm{d}\phi^2). \tag{1.19}$$

The matter content is specified by the stress energy tensor, which can be taken as that of an ideal fluid,

$$T_{\mu\nu} = (p+\rho)u_{\mu\nu} + pg_{\mu\nu} \tag{1.20}$$

where u_μ is the 4-velocity, p the pressure and ρ the mass-energy density. Further imposing that matter is at rest in our frame of reference (i.e., u_μ has no space-like components),

only three of the four equations 1.18 are actually independent. Their solution can be written as

$$\begin{aligned} A(r) &= \left(1 - \frac{2Gm(r)}{rc^2}\right)^{-1} \quad \text{where} \quad m(r) = \int_0^r 4\pi r^2 \rho \, \mathrm{d}r \\ \frac{1}{2B}\frac{\mathrm{d}B}{\mathrm{d}r} &= -\frac{1}{p + \rho c^2}\frac{\mathrm{d}p}{\mathrm{d}r}. \end{aligned} \tag{1.21}$$

These three equations do not form a closed system: in order to solve them, a further relation between p and ρ must be introduced. This is the so-called *equation of state* (EoS), which depends on the properties of matter and not of the spacetime itself. Assuming such a relation, the solution can than be rewritten as

$$\frac{\mathrm{d}p}{\mathrm{d}r} = -\rho \frac{Gm(r)}{r^2}\left(1 + \frac{p(\rho)}{\rho c^2}\right)\left(1 + \frac{4\pi r^3 \rho}{m(r)c^2}\right)\left(1 - \frac{2Gm(r)}{rc^2}\right)^{-1} \tag{1.22}$$

which is known as the *Tolman-Oppenheimer-Volkoff (TOV) equation*. The boundary conditions to be specified are $m(r = 0) = 0$ and $p(R_\star) = 0$; the latter defines the radius of the star, from which the total gravitational mass is computed as

$$M = m(R_\star) = \int_0^{R_\star} 4\pi r^2 \rho \, \mathrm{d}r. \tag{1.23}$$

By specifying different values of the central pressure/density, different models can be computed. In particular, a given equation of state is associated to a maximum predicted NS mass. Equations predicting a small maximum mass are called *stiff*, while if this mass is big they are called *soft*. The maximum mass quantity provides a first comparison with observations, as many EoSs predict maximum masses which are smaller than what observed—the heaviest known NS with an accurate mass estimate to date has $M = 2.14^{+0.10}_{-0.09}\, M_\odot$, (Cromartie et al., 2020). Moreover, the condition $p = 0$ gives a prediction for the stellar radius. By means of this quantity, a *mass-radius relation* can be built, which will depend on the EoS itself (see Fig. 1.4). Knowing this relation precisely would put extremely strict constraints on the form of the EoS itself; unfortunately, the radius is notoriously extremely hard to measure with any degree of precision, and notwithstanding the advancements of the last decades no robust limits for the EoS have still been put in this way.

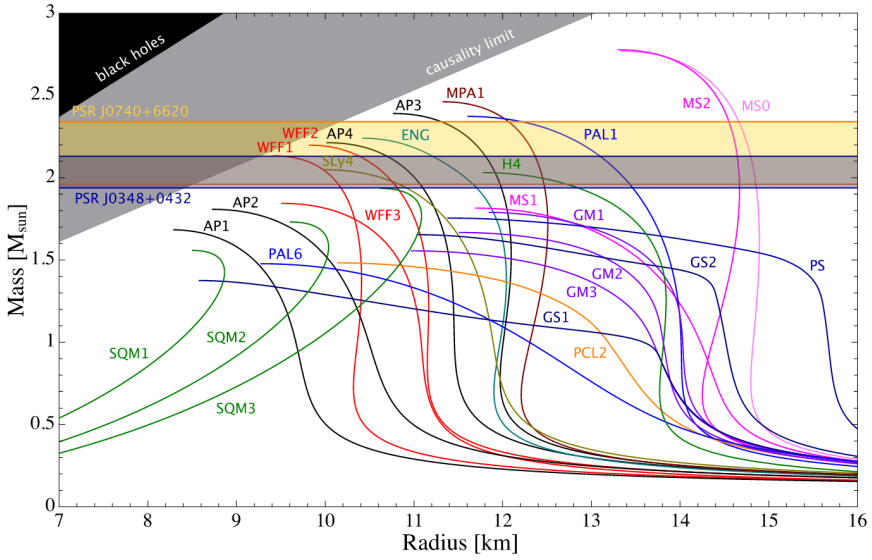

Figure 1.4: Mass-radius relation for a wealth of different EoSs. The horizontal band correspond to the mass measure (at 2σ confidence) of the two heaviest known NSs, PSR J0348+0432 (Antoniadis et al., 2013) and PSR J0740+6620 (Cromartie et al., 2020). Figure reproduced from Hu et al. (2020).

CHAPTER 2

The Physics of Neutron Star Magnetic and Thermal Evolution

In this chapter, the physical ingredients involved in the evolution of the temperature and of the magnetic field in a NS are presented. First, the basic physics of NS cooling will be reviewed, describing the different core cooling regimes. Then, the evolution of the magnetic field will be addressed, with particular attention to the NS crust. Finally, the strong coupling between these two problems will be discussed, laying the basis for the new simulations presented in the next chapters.

2.1 Cooling of low-magnetised NSs

Observing directly the internal regions of a NS or obtaining information on the states of matter therein with experiments is impossible. Hence, NS composition must be studied by identifying those quantities which are sensitive to it, and studying them as they evolve in time or on a large sample of different objects. Collecting data of the mass and radius of as many NSs as possible may appear as the most natural course of action, but it is often very hard to measure them both, and more so independently of each other. Since many NSs emit at least one thermal component, temperature can be directly measured. Cooling mechanisms and heat transport properties strongly depend on the composition, so that thermal evolution of NSs can put constraints on the physics of ultra-dense matter. This is an extremely vast topic and ever increasingly detailed models have been developed since the work of Tsuruta and Cameron (1966) (see e.g. the review by Potekhin et al., 2015). The temperature of a NS can vary due to a variety of processes: accretion, exothermic nuclear reactions and magnetic field dissipation are able to heat the star, while neutrino and photon emission act as cooling agents. This section will briefly review the thermal evolution of isolated, low magnetised NSs, that passively cool down.

Let us first consider the case of a star with uniform temperature $T(t)$. Very soon after the SN explosion, a NS becomes transparent to neutrinos, so that the neutrino "luminosity" comes from the whole volume of the star and is due to the weak reactions

going on in the core. A complete review of neutrino processes in NS can be found in Yakovlev et al. (2001), which provides a complete coverage of what reviewed in the following.

The high fraction of neutrons in a NS core implies that β decay is balanced by some sort of *neutronisation* process. In the case in which the Fermi energy of particles is high enough to fill the neutron-proton mass gap $Q = m_n - m_p \simeq 1.29\,\mathrm{MeV}$, this process can be the inverse β decay itself, bringing to balance the reactions

$$\begin{cases} n \to p + e^- + \bar{\nu}_e \\ e^- + p \to n + \nu_e. \end{cases} \tag{2.1}$$

This reaction produces neutrinos, which can efficiently cool down the core; in NS physics, this is the so-called URCA process, first introduced by Gamow and Schoenberg (1940) (see Sec. 1.1). The corresponding neutrino luminosity can be calculated from the emissivity (emitted energy per unit time and unit volume) N, which can be itself written for each reaction in terms of the quantum mechanical matrix element of the process,

$$N = \int \epsilon_\nu \, \mathrm{d}W_{i\to j} \sum_i \frac{\mathrm{d}\boldsymbol{p}_i}{(2\pi)^3} f_i \sum_j (1 - f_j) \tag{2.2}$$

where ϵ_ν is the emitted neutrino energy, i labels the particles in the initial state, j those in the final one, f is the distribution function of the particles (which will be the Fermi-Dirac one for the degenerate case) and $\mathrm{d}W_{i\to j}$ denotes the differential probability of the reaction (see the diagram in Fig. 2.1). The computation of this quantity can be done in Fermi weak interaction theory and will not be covered here. For our purposes, it is sufficient to note the temperature scaling of this quantity: when performing the phase space integration, the momenta of the degenerate particles that are involved in the reaction will be separated by $\approx k_B T$ from the Fermi energy, giving a $\sim T$ contribution each, while the non-degenerate emitting neutrino will yield a contribution $\sim T^2$ for the conservation of energy and momentum; a further contribution $\sim T$ comes from ϵ_ν in the integral. In the case of the URCA process, there are three degenerate particles, so the final dependence is $\sim T^6$.

The URCA process, however, has a kinematic threshold: it is only possible when the momenta of the degenerate proton, electron and neutron satisfy the triangle relation

$$p_{Fn} < p_{Fe} + p_{Fp}. \tag{2.3}$$

Considering a model of completely degenerate *npe* matter, it can be shown that this corresponds to a proton to total baryon ratio higher than $n_p/n_b = 1/9$ (e.g. Shapiro and Teukolsky, 1983). However, the very same simple model predicts that this ratio is always smaller than 1/9, approaching this value from below as the density increases, so that the URCA process has been deemed impossible in NSs for a long time. Following the work of Lattimer et al. (1991), however, it is now believed that the URCA process may indeed be at work in some NSs. This may be the result of an EoS that allows for the kinematic threshold to be satisfied under some conditions, or of the presence of other

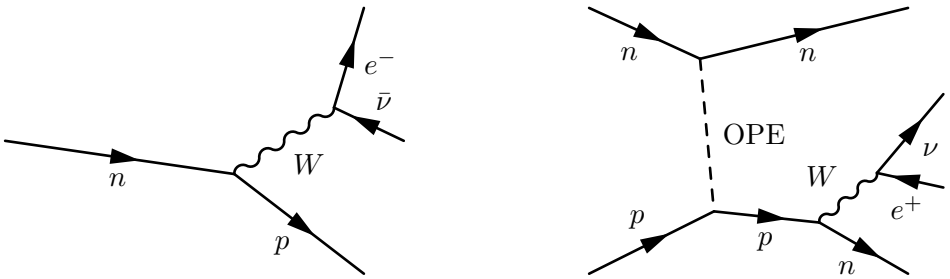

Figure 2.1: Two example Feynman diagrams for (a) β decay and (b) a reaction of the mURCA process, where the strong interaction is written as an effective one particle exchange (OPE). For the sake of clarity, the charged current reaction is shown, even though calculations are often done in the Fermi effective theory where it becomes a 4-tailed vertex.

particle species such has hyperons (the *exotica*), which can take the role of a nucleon in the reaction but do not pose strict kinematic constraints, as they are not degenerate. In any case, these phenomena are expected to be realised only in the innermost regions of some high mass NSs; thus, the main neutrino NS cooling agent is still to be sought in another mechanism.

Momentum conservation can be more easily satisfied if a by-standing nucleon N participates to the reaction by supplying the needed momentum, without decaying itself (see the Feynman diagram in Fig. 2.1),

$$\begin{cases} n + N \to p + e^- + \bar{\nu}_e + N \\ e^- + p + N \to n + \nu_e + N. \end{cases} \tag{2.4}$$

The by-stander can be either a neutron (*neutron branch*) or a proton (*proton branch*), with similar rates (even though the latter has its own kinematic threshold, which is much less strict than the URCA one). The final effect on the emissivity is that two more degenerate particle contribution are added, so that an additional $\sim T^2$ appears, which brings the total to $\sim T^8$. Moreover, the corresponding diagram contains two more interaction vertices, so that the value of the emissivity at the same temperature is lower than in the direct URCA process. This process, referred to as *modified URCA* (mURCA), is thought to be the main cause of NS cooling.

In order to address the effects of these cooling processes on the temperature of a NS, one can write the energy equation for an isothermal object as

$$C\frac{\mathrm{d}T}{\mathrm{d}t} = -L \tag{2.5}$$

where C is the total specific heat, which in the core depends on temperature as $C = \tilde{C}T$ (Potekhin et al., 2015), and L is the total energy loss rate. Focusing on neutrino losses

only and writing the corresponding term as $L_\nu = \tilde{N} T^k$, we get

$$\frac{\mathrm{d}T}{\mathrm{d}t} = -\frac{\tilde{N}}{\tilde{C}} T^{k-1} \quad \Rightarrow \quad \begin{cases} T \sim t^{-1/4} & \text{URCA} \\ T \sim t^{-1/6} & \text{mURCA.} \end{cases} \tag{2.6}$$

From this simple calculation, one can see that cooling via the direct URCA process has a steepest time decay; for this reason, it is called the *fast cooling* process. In contrast, cooling by modified URCA reactions is known as *slow cooling*.

There are countless more possibilities for neutrino processes in NS cores (e.g. reactions involving muons or hyperons), which can alter the cooling evolution. Moreover, all the emissivities can be affected by the onset of a superfluid/superconducting nucleon phase in the core, which alters the phase space distributions, as well as by opening neutrino production channels from Cooper pairs; this will not be covered in detail in this work, but the two mechanism presented here serve as the general terms of comparison for all the other cooling scenarios prompted by them.

On the other hand, NS matter is opaque to photons: hence, photon emission comes from the surface of the star only, with a luminosity that to a first approximation is given by

$$L_\gamma = 4\pi R_\star^2 \sigma_S \, T_s^4 \tag{2.7}$$

where σ_S is the Stefan-Boltzmann constant and T_s is the effective surface temperature. Note that the effective surface temperature T_s in this expression is not the core one, even assuming an isothermal star: in fact, one must take into account that the outermost stellar layers have a large optical depth, so that they host a very large thermal gradient and as a result the surface temperature is altered significantly with respect to the internal one (see Sec. 2.1.1). As a first approximation to perform a simple analytical calculation, the surface temperature can be expressed as $T_s = T^{1/2+\alpha}$, with a constant $\alpha \simeq 1/8$ (Shapiro and Teukolsky, 1983). Solving Eq. 2.5 for the photon contribution then gives

$$\frac{\mathrm{d}T}{\mathrm{d}t} = -\frac{4\pi R_\star^2 \sigma_S}{\tilde{C}} T^{1+4\alpha} \quad \Rightarrow \quad T \sim t^{-\frac{1}{4\alpha}}, \tag{2.8}$$

which gives an even steeper time dependence. However, photon cooling takes place at later times compared to the neutrino one, resulting in a knee in the cooling curve.

The simple model described so far assumes an isothermal core; while its conductivity is high enough not to support huge temperature gradients, this is certainly limiting, especially because the emissivities strongly depends also on density. The more general form of the heat equation is written as a form of Fourier's law[1],

$$C_v \frac{\mathrm{d}T}{\mathrm{d}t} = \boldsymbol{\nabla} \cdot (\boldsymbol{k} \, \boldsymbol{\nabla} T) - N_\nu \tag{2.9}$$

where $\boldsymbol{k}$ is the thermal conductivity tensor. Photon emission is not explicitly present in this equation, but it enters as a boundary condition on $\boldsymbol{\nabla} T(R_\star)$, which depends on the

[1] In general, the heat equation should be written taking into account GR corrections. However, as discussed later, they have little effect in the cases considered in this work, hence they are omitted here.

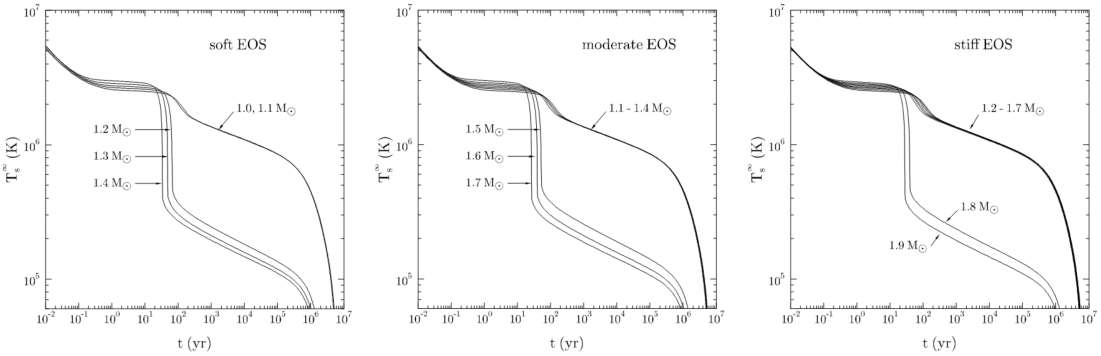

Figure 2.2: Examples of cooling curves for three different EoSs and different stellar masses. Note that in all cases (albeit at different thresholds) direct URCA processes are allowed, resulting in the fast cooling process for the higher mass stars. Note also the knee at $t \approx 10^6$ yr, corresponding to the onset of photon cooling regime. Figures are reproduced from Yakovlev et al. (2001).

relation between the temperature at the top of the crust and the effective surface one. This problem is often treated separately, and will be reviewed in the next section. If magnetic fields are negligible, this equation can be treated in its 1D form (i.e. assuming spherical symmetry), and much effort has been put into solving it with more and more accurate microphysical input. As an example, Fig. 2.2 shows the results by Yakovlev et al. (2001), who studied different EoS allowing the direct URCA process to be triggered at high densities.

2.1.1 NS Envelopes

The outermost layers of a NS, comprising the outer crust, the ocean and the atmosphere (if present) are problematic to treat in the framework discussed in the previous section. In fact, they are geometrically thin (≈ 100 m) but optically thick, and hence host a huge temperature gradient. For this reason, they are treated separately in plane parallel approximation and inserted in the cooling equations as a relation between the temperature at the top of the crust (and bottom of the envelope) T_b and the one at the top of the envelope (the surface one) T_s, which determines the surface temperature gradient to be used as a boundary condition.

Such envelope models date back to Tsuruta and Cameron (1966), and as a general rule of thumb (see e.g. Shapiro and Teukolsky, 1983) the $T_b - T_s$ relation (sometimes called *Tsuruta law*) goes like

$$T_s \approx 10^{-2} \alpha \, T_b \qquad 0.1 \lesssim \alpha \lesssim 1. \tag{2.10}$$

Gudmundsson et al. (1983) showed that the envelope structure only depends on the composition and the ratio between the surface temperature and a power of the surface

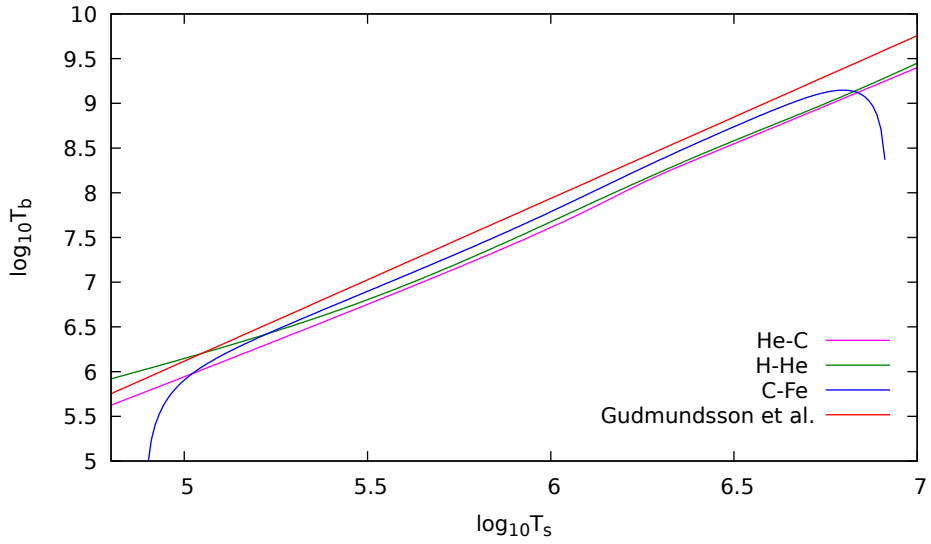

Figure 2.3: Examples of $T_b - T_s$ relations for various compositions of the envelope. The red curve corresponds to Eq. 2.11, whereas the others describe realistic models of light-element envelopes from Beznogov et al. (2016). In all cases, the same characteristic value of the surface gravity $g \sim 2 \times 10^{14}\,\mathrm{cm^2\,s^{-1}}$ was considered.

gravity g, proposing the relation

$$\left(\frac{T_b}{10^8\,\mathrm{K}}\right) = 1.288\left[\frac{1}{g_{14}}\left(\frac{T_s}{10^6\,\mathrm{K}}\right)^4\right]^{0.455} \tag{2.11}$$

where g_{14} is expressed in units of the scale value $10^{14}\,\mathrm{cm\,s^{-2}}$. This expression describes an unaccreted, Fe-Ni envelope and has become a standard reference for NS cooling. Accretion can nonetheless alter the composition of the envelope by adding light elements; Fig. 2.3 shows three examples of $T_b - T_s$ relations for different chemical compositions.

Moreover, the presence of a strong magnetic field affects the transport properties in the envelope. Since heat transport is thwarted across field lines and favoured along them, the formation of a temperature gradient is not equally efficient in all the regions of a magnetised envelope. This effect can be described by adding a magnetic correction factor $\mathcal{X}$ to the $T_b - T_s$ relation as

$$T_s = T_s^{(0)}(g, T_b)\mathcal{X}(B, \Theta, T_b) \tag{2.12}$$

where $T_s^{(0)}$ represent the expression for an unmagnetised envelope, B is the local magnetic field strength and Θ the angle $\boldsymbol{B}$ forms with the normal to the surface. This expression is discussed in Potekhin and Yakovlev (2001), where the authors also provide a practical fitting formula for $\mathcal{X}$ that will be adopted throughout this work. It is worth remarking how this magnetic effect strongly links the surface field topology to the observed temperature

map; this has profound implications for magnetothermal evolution modelling, and will be one of the main points discussed in the next chapters. An up-to-date review of envelope physics and modelling, which also provides practical relations for different envelope compositions, can be found in Beznogov et al. (2021).

2.2 The Evolution of the Magnetic Field

For decades, the idea that the magnetic field of a NS could decay on astrophysically relevant timescales was considered impossible and little attention was given to its study. Nowadays, the evolution of the magnetic field is considered a crucial issue in NS modelling, yet it still presents many uncertainties. In this work, we will focus on the evolution of the crustal field (see discussion in Sec. 3.2), which is supported by the motion of degenerate electrons in a Coulomb lattice. In this section, the equations governing this system will be derived from first principles, highlighting all the relevant assumptions.

2.2.1 The eMHD regime

The magnetic and electric fields in presence of an electric charge distribution with density ρ_e and a current $\boldsymbol{J}$ are given by the *Maxwell equations* (which we write here without general-relativistic corrections, see Sec. 3.2),

$$\begin{aligned} \boldsymbol{\nabla}\cdot\boldsymbol{E} &= 4\pi\rho_e \qquad & \boldsymbol{\nabla}\times\boldsymbol{E} &= -\frac{1}{c}\frac{\partial \boldsymbol{B}}{\partial t} \\ \boldsymbol{\nabla}\cdot\boldsymbol{B} &= 0 \qquad & \boldsymbol{\nabla}\times\boldsymbol{B} &= \frac{4\pi}{c}\boldsymbol{J} + \frac{1}{c}\frac{\partial \boldsymbol{E}}{\partial t}. \end{aligned} \tag{2.13}$$

They describe a system of charged particles, i.e. a plasma, once the charge and currents distribution is specified. In particular, for a system formed by n_i ions of charge Ze and n_e electrons per unit volume, moving with velocities $\boldsymbol{v}_i$ and $\boldsymbol{v}_e$ respectively, the current density is given by

$$\boldsymbol{J} = \mathrm{e}(Zn_i\boldsymbol{v}_i - n_e\boldsymbol{v}_e). \tag{2.14}$$

Since we will deal with processes occurring on macroscopic spatial and temporal scales, charge separation effects can be neglected by imposing local charge neutrality, $n_e = Zn_i$, and working in the *MHD approximation*, i.e. neglecting the displacement current term in the last of Maxwell's equation 2.13,

$$\boldsymbol{J} = \frac{c}{4\pi}\boldsymbol{\nabla}\times\boldsymbol{B}. \tag{2.15}$$

Furthermore, a NS crust can be described in the *electron MHD* regime, in which only electrons are moving. In fact, the huge gravity and lattice structure of a Coulomb crystal makes so that the ion nuclei can be regarded as a fixed background with infinite inertia, $\boldsymbol{v}_i \to 0$. In this case, it is just necessary to supply a generalised Ohm law for the electrons (Ziman, 1972),

$$\boldsymbol{E} = \boldsymbol{\sigma}^{-1}\cdot\boldsymbol{J} - \nabla\mu/\mathrm{e} \tag{2.16}$$

where μ is the chemical potential of electrons (subscripts e will be dropped from now on) and $\boldsymbol{\sigma}$ is the *electrical conductivity tensor*.

The tensorial nature of this quantity reflects its dependence on the magnetic field: in fact, electrons gyrate along field lines making charge transport anisotropic. At first order in the field, this relation can be written out from symmetry assumptions (remembering that $\boldsymbol{B}$ is a pseudo-vector) as

$$(\sigma^{-1})_{i,j} = \sigma^{-1}\delta_{ij} + C\epsilon_{ijk}B_k \tag{2.17}$$

where Einstein index summation is understood and ϵ_{ijk} is Levi-Civita symbol. The two constants are to be determined by imposing a model for the microphysical behaviour of electrons, i.e. the scattering between themselves and with impurities and phonons in the crust. Assuming that the crust is below the electron degeneracy temperature, but above the ion plasma temperature, scattering can be described through a characteristic relaxation time τ, that is assumed to depend on the electron energy only (see e.g. Urpin and Yakovlev, 1980). Further assuming that the electron scattering rate $1/\tau$ is faster than the electron gyration frequency, the electron distribution function can be approximated as a linear perturbation to the Fermi-Dirac distribution, and using a Sommerfeld expansion in the temperature one finds at leading order (see again Ziman, 1972)

$$(\sigma^{-1})_{i,j} = \sigma^{-1}\delta_{ij} + \frac{\epsilon_{ijk}B_k}{\mathrm{e}cn} \quad \text{where} \quad \sigma = \mathrm{e}^2c^2\frac{n\,\tau(\mu)}{\mu}. \tag{2.18}$$

Combining Eqs. 2.13, 2.15 and 2.18 we finally get the Hall induction equation,

$$\frac{\partial B}{\partial t} = -\boldsymbol{\nabla}\times\left[\frac{c^2}{4\pi\sigma}\boldsymbol{\nabla}\times\boldsymbol{B} + \frac{c}{4\pi en}(\boldsymbol{\nabla}\times\boldsymbol{B})\times\boldsymbol{B}\right], \tag{2.19}$$

where the first term on the RHS represents ohmic dissipation, while the second one the nonlinear Hall effect.

2.2.2 The Hall evolution & NSs

The Hall term is one of the fundamental ingredients in shaping the stellar field, especially in the first phases of the evolution. It may be at first glance discarded, since it is an energy conserving term,

$$\begin{aligned}\left.\frac{\partial B^2}{\partial t}\right|_{\text{Hall}} = 2\boldsymbol{B}\cdot\dot{\boldsymbol{B}}|_{\text{Hall}} = 2\boldsymbol{B}\cdot\boldsymbol{\nabla}\times[(\boldsymbol{\nabla}\times\boldsymbol{B})\times\boldsymbol{B}] = 2B_i\epsilon_{ijk}\partial_j\epsilon_{klm}\epsilon_{lpq}\partial_pB_qB_m = \\ = 2\left(\delta_{jl}\delta_{im}-\delta_{jm}\delta_{il}\right)\epsilon_{lpq}\partial_j\partial_pB_iB_qB_m = \underbrace{\epsilon_{jpq}\partial_j\partial_pB_qB^2}_{\text{antisym}\times\text{ sym in }p\text{ and }q} - \underbrace{\epsilon_{ipq}\partial_j\partial_pB_iB_qB_j}_{\text{antisym}\times\text{ sym in }i\text{ and }q} = 0,\end{aligned}$$

but it actually plays an important role in the magnetic field evolution. In fact, Geppert and Wiebicke (1991) showed that it has two fundamental properties:

- it couples different multipoles of the field, allowing energy to be exchanged between structures of different scales;

- it couples the poloidal and toroidal components of the field (see Sec. 3.1.2 for a formal definition).

This means not only that the topology of the field is largely determined by the action of this term, but also that ohmic dissipation is enhanced because it can occur on smaller scales.

To understand the interplay between the two terms in Eq. 2.19, by scaling arguments one defines the Hall and Ohm timescales (Goldreich and Reisenegger, 1992; Pons and Geppert, 2007),

$$\begin{aligned} \tau_H &= \frac{4\pi n e L^2}{cB} &&\approx 6.4 \left(\frac{n}{10^{34}\,\mathrm{cm}^{-3}}\right)\left(\frac{10^{13}\,\mathrm{G}}{B}\right)\left(\frac{L}{1\,\mathrm{km}}\right)^2 10^4\,\mathrm{yr} \\ \tau_O &= \frac{4\pi\sigma}{c^2}L^2 &&\approx 4.4 \left(\frac{\sigma}{10^{24}\,\mathrm{s}^{-1}}\right)\left(\frac{L}{1\,\mathrm{km}}\right)^2 10^6\,\mathrm{yr}, \end{aligned} \tag{2.20}$$

where L is a characteristic length and the numerical values are scaled to fiducial NS parameters. Typically, therefore, the Hall effect is able to shape the field before ohmic dissipation takes over, which in turn happens on similar timescales to the cooling ones.

2.3 The Temperature Equation & Electromagnetic Fields

Electrons are the sole carriers of energy in a Coulomb lattice (as well as in most terrestrial materials), and as such support the electromagnetic fields and temperature gradients at the same time. It then comes as no surprise that the induction and heat transport equations are indeed coupled in several ways. During the buildout of classical electromagnetism in the 19th century, several experiments studied the effect of variously crossed electric/magnetic fields and temperature gradients, resulting in a variety of "effects" (see Ziman, 1972, and references therein for an exhaustive discussion). One of these is the Hall effect, i.e. the result of crossing electric and magnetic field, which was addressed in the previous section. Here, those involving both the electromagnetic and temperature fields will be reviewed.

The most notable effects are the ones of the magnetic field on the thermal conductivity and of electromagnetic dissipation. In the same way as the presence of a magnetic field makes the electrical conductivity anisotropic, Eq. 2.18, thermal conductivity is suppressed across magnetic field lines, around which thermal-energy-carrying electrons gyrate. If the number of occupied Landau levels is high enough that quantizing effects can be neglected (which is well the case in a NS crust) and further neglecting electron-electron scatterings, the relation between the electrical conductivity $\boldsymbol{\sigma}$ and the thermal one $\boldsymbol{k}$, which is now a tensor, is quite simple,

$$\boldsymbol{k} = \frac{\pi^2 k_B^2 T}{3e^2}\boldsymbol{\sigma} \tag{2.21}$$

which is the well-known *Wiedemann-Franz law*.

The first term of Eq. 2.19 has already been described as the one responsible for the ohmic decay. As it dissipates energy in the form of heat, the magnetic field enters the

heat balance equation as the well known *Joule heating* effect. This term drains energy from the magnetic field in presence of a current, transferring the power

$$\boldsymbol{E} \cdot \boldsymbol{J} \tag{2.22}$$

per unit volume.

Furthermore, some effects are linked to the presence of a temperature gradient. The crucial quantity controlling the relation between electric field and temperature gradient is the *thermopower* $\boldsymbol{G}$, defined as

$$\boldsymbol{E} = \boldsymbol{G} \cdot \boldsymbol{\nabla} T. \tag{2.23}$$

This quantity can be computed through the *Mott formula*,

$$\boldsymbol{G} = \mathrm{e}\, \frac{\partial \boldsymbol{\sigma}^{-}1}{\partial \mu}\bigg|_{T} \cdot \boldsymbol{k}. \tag{2.24}$$

This tensor has an isotropic part, called the *Seebeck term*, and an anisotropic part proportional to the conductivity tensor, called the *Ettingshausen–Nernst term*. Physically, the Seebeck term represents advection of electron entropy. The Ettingshausen–Nernst term, on the other hand, has no simple physical interpretation, and moreover is sensitive to the particular form of the relaxation time τ, so for simplicity it will not be included in this work. Under this assumption, the thermopower can be written as

$$\boldsymbol{G}_{ij} = -\frac{S}{\mathrm{e}}\delta_{ij} \simeq -\frac{\pi^2 k_B^2 T}{\mu \mathrm{e}}\delta_{ij} \tag{2.25}$$

where S is the entropy per electron, and the last equality holds for a completely degenerate Fermi gas. The Seebeck effect was first measured as the creation of difference of electric potential between the hotter and colder end of a metal rod, and was historically the first thermoelectric effect to be discovered. If the additional electric field produced by the thermal gradient is not constant in time, it can give rise by induction to a magnetic field; this is the so-called *Biermann battery effect* (Biermann, 1950), which has been often invoked as an efficient mechanism for field amplification in systems like AGN jets (e.g. Prior and Gourgouliatos, 2019) and in the early universe (e.g. Gnedin et al., 2000).

With the inclusion of these effects, the heat equation 2.9 can be finally rewritten as

$$C_V \frac{\partial T}{\partial t} = -\boldsymbol{\nabla} \cdot \boldsymbol{Q} + \boldsymbol{E} \cdot \boldsymbol{J} - N_\nu \tag{2.26}$$

where the heat flux $\boldsymbol{Q}$ is given by the generalised Fourier law,

$$\boldsymbol{Q} + \frac{\mu}{\mathrm{e}}\boldsymbol{J} = -\boldsymbol{k} \cdot \boldsymbol{\nabla} T + T\boldsymbol{G} \cdot \boldsymbol{J}. \tag{2.27}$$

This equation, coupled with the induction equation 2.19, will be the foundation of our model. In the next section, the computational tools needed to tackle them will be described.

CHAPTER 3

Solving the Evolution Equations

The magnetic and thermal evolution equations presented in the last chapter form a system of non-linear second order partial differential equations (PDEs), the former being of the dispersive type, while the latter is diffusive. They are strongly coupled, both by terms containing explicitly the two unknown functions and by the functional dependencies of the transport coefficients. This chapter describes the algorithm chosen in this work to solve them, alongside the main physical assumptions that must be introduced to make the problem practicable.

Solving the coupled magnetic and thermal evolution of a NS is a numerically challenging task, which has been the object of several studies in the last decades. As already mentioned in Sec 1.1, thermal evolution has been the first to be addressed (Tsuruta and Cameron, 1966b) and has subsequently been object of a tremendous effort in refining of the microphysical input (e.g. Yakovlev and Urpin, 1981; Page and Baron, 1990; Levenfish and Yakovlev, 1996; Page et al., 2006; Potekhin et al., 2015). In the vast majority of cases, however, the magnetic field was not included. This was both because the idea that the magnetic field of a NS could decay over astrophysically relevant timescales was not widely accepted, and on a more technical ground because the codes used to solve the heat transport equation inside the star were one-dimensional, i.e. based on perfect spherical symmetry that any magnetic field would break.

Once the importance of magnetic field evolution and decay was understood, several authors developed codes capable of handling the field (see the recent review in Pons and Viganò, 2019), first accounting for 2D ohmic dissipation only (Pons et al., 2009), and then incorporating the Hall effect coupled with the temperature in 2D (Viganò et al., 2013), or the Hall effect in 3D but with no temperature (Wood and Hollerbach, 2015). This work is part of the bridging between these approaches, in that it includes both a 3D domain and the coupled evolution equations. Still, it must be borne in mind that the inclusion of higher dimensions implies much heavier numerical schemes, so that some trade-offs with the microphysical accuracy must be made. At the same time, 1D but very detailed models should not be regarded as outdated, but rather complementary to what is presented here.

3.1 The PARODY code

The tool of choice to treat evolution equations in this work is the code PARODY , written in the FORTRAN language with a parallelisation via both shared (MPI) and distributed computing (OpenMP). In this section, its main characteristics will be reviewed, even though an in depth description is beyond the scope of this work: in fact, the core features of the code date back to the 1990s, and were originally developed by Dormy et al. (1998); Aubert et al. (2008, see also Dormy 1997 for a thorough presentation, from which the present one is adapted) for the study of geomagnetism. Its capabilities to solve PDEs in full 3D on a spherical domain were later on adapted by Wood and Hollerbach (2015) to address the magnetic evolution of NSs, and further used in Gourgouliatos et al. (2016); Gourgouliatos and Hollerbach (2018); Gourgouliatos and Pons (2019); Gourgouliatos et al. (2020). The aim this work has been to add to PARODY the coupled thermal evolution equation, which has been done for the first time with realistic boundary conditions and full accounting for crustal neutrino emission (De Grandis et al., 2020, see also Igoshev et al. 2020 for an application of a simplified version of the same magnetothermal code).

3.1.1 The basic algorithm

PARODY is a *pseudo-spectral* code, in the sense that only part of the problem (namely, the angular derivatives) is treated with a spectral algorithm, whereas the remaining one (i.e. the radial derivatives) is treated with a finite difference scheme. Spectral algorithms are those which take advantage of a Fourier-like decomposition in order to algebraise derivatives; the set of basis functions used by the code is that of spherical harmonics (see App. B), which is the most appropriate to describe domains with spherical symmetry. The code, hence, operates by performing "Fourier" (inverse-) transforms to evaluate angular derivatives in the spectral space via simple algebraic operations. These transforms are performed by integration using the Gauss-Legendre quadrature method (see App. C), so that the meridional (θ) grid is of the Gauss-Legendre type, i.e. built on the zeros of the Legendre polynomials. The number of points is chosen so that the grid contains the length scales up to the ones described by the higher mode considered $\ell_{\max}$. This would correspond to taking $2\ell_{\max}$ points. However, spectral codes suffer of the so-called *aliasing* issue: if the grid is undersampled, the integration in the spectral space may spuriously transfer energy to the larger scales. This is of particular concern when turbulent-like phenomena that transfer energy to smaller and smaller scales are triggered. A simple way to tackle this problem is to increase the number of points (e.g. Canuto, 1988); generally, the code uses 3/2 of the minimum value, which can be further raised if needed.

Radial derivatives, in turn, are treated via a space-centred finite difference scheme, written on an irregular grid of size N_r built following a geometric series with the finest resolution near the boundaries. The main advantage of this choice is that the algorithm can be easily parallelised, as each computing thread will solve the equations on a given spherical shell (for this reason, the number of threads and the radial resolution are bound by the condition that each thread must handle at least 4 grid points in order to take

derivatives).

Time advance is treated differently for linear and non-linear terms, with an implicit and explicit scheme respectively. Let us consider as an illustrative example a schematic version of the temperature equation,

$$\frac{\partial T}{\partial t} = \boldsymbol{\nabla}^2 T + Q. \tag{3.1}$$

If $T^{(n)}$ is the variable at the n-th timestep, the equation gets discretised as

$$\frac{T^{(n+1)} - T^{(n)}}{\mathrm{d}t} = \underbrace{\boldsymbol{\nabla}^2 \left(\frac{T^{(n+1)} + T^{(n)}}{2} \right)}_{\text{C-N}} + \underbrace{\frac{3}{2} Q^{(n)} - \frac{1}{2} Q^{(n-1)}}_{\text{A-B}} \tag{3.2}$$

where the first term on the RHS is treated using the *Crank-Nicolson* scheme, whereas the second uses the *Adams-Bashforth* one. The latter is the explicit part of the scheme, which gets computed in the real (or *configuration*) space, whereas the former is implicit: focusing on it, the terms can be rearranged as

$$\underbrace{\left(\frac{1}{\mathrm{d}t} - \frac{1}{2} \boldsymbol{\nabla}^2 \right)}_{\mathcal{A}} T^{(n+1)} = \left(\frac{1}{\mathrm{d}t} + \frac{1}{2} \boldsymbol{\nabla}^2 \right) T^{(n)}. \tag{3.3}$$

The solution at timestep $n+1$ can be obtained through the inversion of the operator $\mathcal{A}$. This is performed in the spectral space, i.e. after writing the equation for each mode $T_{\ell m}(r)$, with

$$T(r, \theta, \phi; t) = \sum_{\ell, m} T_{\ell m}(r; t)\, Y_\ell^m(r). \tag{3.4}$$

The angular part of the Laplace operator, Δ_S, gets algebraised through the eigenvalue relation of Eq. B.2, which depends on ℓ only, so that we are left with an operator $\mathcal{A}_\ell$ for each mode. Then, the application of the radial difference scheme turns $\mathcal{A}_\ell$ into a $N_r \times N_r$ matrix; since derivatives are taken using the values in three points, it has the structure of a band matrix,

$$\mathcal{A}_\ell = \begin{pmatrix} b_\ell^{(1)} & c_\ell^{(1)} & 0 & \cdots & 0 & 0 \\ a_\ell^{(1)} & \ddots & \ddots & & & 0 \\ 0 & \ddots & \ddots & \ddots & & \vdots \\ \vdots & & \ddots & \ddots & \ddots & 0 \\ 0 & & & \ddots & \ddots & c_\ell^{(N_r-1)} \\ 0 & 0 & \cdots & 0 & a_\ell^{(N_r-1)} & b_\ell^{(N_r)} \end{pmatrix}; \tag{3.5}$$

the part of the equation treated by this scheme is hence specified by only writing out the three vectors a_ℓ, b_ℓ and c_ℓ.

The inversion of this large matrix is one of the most computationally expensive parts of the scheme; hence, a key point for the efficiency of the algorithm is that it should not depend on time, so that the inversion can be performed only once for all, save when the value of $\mathrm{d}t$ gets changed. The code continuously checks the Courant conditions to ensure the timestep is adequate, and in the case it is updated the inversion must be repeated. This operation, however, takes place only when a significant evolution of the quantities occurs, which typically happens rather seldom. Nevertheless, the time independence of $\mathcal{A}$ poses some limits on the class of problems which can be treated using this part of the code, which will impact in particular on the temperature equation (see the discussion in Sec. 3.2).

The boundary conditions must be imposed by altering the first and/or last elements of the matrices $\mathcal{A}_\ell$ to yield the quantity onto which the desired condition must be imposed. For example, a condition on the radial gradient of the temperature at the uppermost point (akin to the one required by the condition described in Sec. 2.1.1) should be implemented by altering the last elements of the matrix so that the equation at the last grid-point yields the discretised radial derivative there, to which the desired value can then imposed at the RHS; in simplified notation,

$$\begin{pmatrix} \ddots & \ddots & \\ \ddots & \ddots & 0 \\ & -\frac{1}{\mathrm{d}r} & \frac{1}{\mathrm{d}r} \end{pmatrix} T^{(n)} = \left.\frac{\partial T}{\partial r}\right|_{BC}. \tag{3.6}$$

3.1.2 Treating vectors

For the sake of simplicity, the description of the algorithm above only considered the scalar temperature equation. Nevertheless, the main features of the algorithm remain unaltered also for the magnetic field equation once the way in which vectors are treated is specified.

The code exploits the fact that the magnetic field is *solenoidal* to represent it more efficiently. In fact, the condition of zero divergence removes one of the initial three degrees of freedom associated with the three components so that only two components are needed to specify the field. In general, given a vector field $\boldsymbol{V}$ which is solenoidal, $\boldsymbol{\nabla}\cdot\boldsymbol{V}=0$, it is possible to introduce the *poloidal-toroidal decomposition* in terms of two scalar functions,

$$\boldsymbol{V} = \boldsymbol{V}_{\mathrm{pol}} + \boldsymbol{V}_{\mathrm{tor}} = \boldsymbol{\nabla}\times[\boldsymbol{\nabla}\times(\boldsymbol{k}V_p)] + \boldsymbol{\nabla}\times(\boldsymbol{k}V_t) \tag{3.7}$$

for any vector $\boldsymbol{k}$. When using polar spherical coordinates, the canonical choice is $\boldsymbol{k}=\boldsymbol{r}$. One can prove that this decomposition is unique. Expanding the curls in spherical coordinates, this decomposition can be written as

$$(V_r, V_\theta, V_\phi) = \left(\frac{1}{r}\Delta_S(V_{\mathrm{pol}}),\ \frac{\partial}{\partial\theta}\left(\frac{1}{r}\frac{\partial}{\partial r}\left(rV_{\mathrm{pol}}\right)\right) + \frac{1}{\sin\theta}\frac{\partial V_{\mathrm{tor}}}{\partial\phi}, \tag{3.8}$$

$$\frac{1}{\sin\theta}\frac{\partial}{\partial\phi}\left(\frac{1}{r}\frac{\partial}{\partial r}\left(rV_{\mathrm{pol}}\right)\right) - \frac{\partial V_{\mathrm{tor}}}{\partial\theta}\right) \tag{3.9}$$

where Δ_S is the angular part of the Laplace operator defined in Eq. B.1.

This decomposition can be generalised to any vector field; in this case, the non-divergenceless part is referred to as the *spheroidal* component, and the decomposition 3.9 can be modified by introducing a third scalar as

$$(V_r, V_\theta, V_\phi) = \left(\frac{1}{r}\Delta_S(V_{\rm pol}),\ \frac{\partial V_{\rm sph}}{\partial\theta} + \frac{1}{\sin\theta}\frac{\partial V_{\rm tor}}{\partial\phi},\ \frac{1}{\sin\theta}\frac{\partial V_{\rm sph}}{\partial\phi} - \frac{\partial V_{\rm tor}}{\partial\theta}\right); \tag{3.10}$$

for the problem at hand, this decomposition is used to treat the current and heat flux vectors. In the case of a solenoidal field, the above decomposition is recovered by setting the spheroidal component to

$$V_{\rm sph} = \frac{1}{r}\frac{\partial}{\partial r}(rV_{\rm pol}). \tag{3.11}$$

If the vector field has axial symmetry with respect to the polar axis of the spherical coordinate system (r, θ, ϕ), then the poloidal component has only r and θ components and $\boldsymbol{V}_{\rm tor} = \boldsymbol{V}_\phi$. Still, it must be borne in mind that this is not true in general, if no symmetries are present.

Finally, it is necessary to provide a spectral representation to the vectorial quantities in our equations. To do this, it is convenient to introduce a new basis of $\mathbb{R}^3$ written as a complex linear combination of the real spherical basis $(\!|\hat{\boldsymbol{r}}, \hat{\boldsymbol{\theta}}, \hat{\boldsymbol{\phi}}|\!)$ as

$$(\!|\hat{\boldsymbol{e}}^+, \hat{\boldsymbol{e}}^0, \hat{\boldsymbol{e}}^-|\!) = \left(\!\!\left| -\frac{1}{\sqrt{2}}\left(\hat{\boldsymbol{\theta}} + \mathrm{i}\hat{\boldsymbol{\phi}}\right),\ \hat{\boldsymbol{r}},\ \frac{1}{\sqrt{2}}\left(\hat{\boldsymbol{\theta}} - \mathrm{i}\hat{\boldsymbol{\phi}}\right)\right|\!\!\right). \tag{3.12}$$

This is known as the basis of *generalised spherical harmonics*, which are defined themselves as [1]

$$\begin{aligned} Y^+_{\ell m} =& \frac{1}{\sqrt{\ell(\ell+1)}}\left(\frac{\partial Y^m_\ell}{\partial\theta} - \mathrm{i}\frac{1}{\sin\theta}\frac{\partial Y^m_\ell}{\partial\phi}\right) \\ Y^0_{\ell m} =& Y^m_\ell \\ Y^-_{\ell m} =& \frac{-1}{\sqrt{\ell(\ell+1)}}\left(\frac{\partial Y^m_\ell}{\partial\theta} + \mathrm{i}\frac{1}{\sin\theta}\frac{\partial Y^m_\ell}{\partial\phi}\right). \end{aligned} \tag{3.13}$$

The components of a vector field $\boldsymbol{V}$ in the $(\!|\hat{\boldsymbol{e}}^+, \hat{\boldsymbol{e}}^0, \hat{\boldsymbol{e}}^-|\!)$ basis can then be expressed as

$$V^{\pm,0}(r,\theta,\phi) = \sum_{\ell=0}^{\infty}\sum_{m=0}^{\ell} V^{\pm,0}_{\ell m}(r)\, Y^{\pm,0}_{\ell m}; \tag{3.14}$$

the angular part of the divergence and curl are then algebraised as (Phinney and Burridge, 1973; Dormy, 1997)

$$\boldsymbol{\nabla}\cdot\boldsymbol{V}(r,\theta,\phi) = \sum_{\ell=0}^{\infty}\sum_{m=0}^{\ell}\left[\frac{1}{r^2}\frac{\partial}{\partial r}\left(r^2 V^0_{\ell m}(r)\right) - \frac{\sqrt{\ell(\ell+1)}}{\sqrt{2}r}\left(V^+_{\ell m}(r) + V^-_{\ell m}(r)\right)\right] Y^m_\ell(\theta,\phi), \tag{3.15}$$

[1] Note that, on top of the different normalisation conventions, several generalisations have been proposed (see Thorne, 1980).

$$
\begin{aligned}
(\boldsymbol{\nabla}\times\boldsymbol{V})^{+}(r,\theta,\phi) &= \sum_{\ell=0}^{\infty}\sum_{m=0}^{\ell} \mathrm{i}\left[-\frac{\sqrt{\ell(\ell+1)}}{\sqrt{2}r}V^{0}_{\ell m}(r) - \frac{1}{r}\frac{\partial}{\partial r}\left(rV^{+}_{\ell m}(r)\right)\right] Y^{+}_{\ell m}(\theta,\phi) \\
(\boldsymbol{\nabla}\times\boldsymbol{V})^{0}(r,\theta,\phi) &= \sum_{\ell=0}^{\infty}\sum_{m=0}^{\ell} \mathrm{i}\,\frac{\sqrt{\ell(\ell+1)}}{\sqrt{2}r}\left(V^{+}_{\ell m}(r) - V^{-}_{\ell m}(r)\right)\; Y^{m}_{\ell}(\theta,\phi) \\
(\boldsymbol{\nabla}\times\boldsymbol{V})^{-}(r,\theta,\phi) &= \sum_{\ell=0}^{\infty}\sum_{m=0}^{\ell} \mathrm{i}\left[\frac{\sqrt{\ell(\ell+1)}}{\sqrt{2}r}V^{0}_{\ell m}(r) + \frac{1}{r}\frac{\partial}{\partial r}\left(rV^{-}_{\ell m}(r)\right)\right] Y^{-}_{\ell m}(\theta,\phi).
\end{aligned}
\tag{3.16}
$$

In order to write the evolution equations in terms of the poloidal and toroidal field, some relations between this representation and the generalised spherical harmonics basis are needed. To this end, let us consider the radial component of the field V_r: this quantity can be itself decomposed in terms of ordinary spherical harmonics (see Eq. B.9), and its relation to the poloidal component is given by the radial Laplace operator from the relation 3.9. Comparing these two relations, one gets

$$
V_r(r,\theta,\phi) = \sum_{\ell=0}^{\infty}\sum_{m=0}^{\ell}(V_r)^m_\ell\, Y^m_\ell(\theta,\phi) = \frac{1}{r}\Delta_S(V_{\mathrm{pol}}) = \frac{1}{r}\sum_{\ell=0}^{\infty}\sum_{m=0}^{\ell}\ell(\ell{+}1)\,(V_{\mathrm{pol}})^m_\ell(r)\,Y^m_\ell(\theta,\phi)
\tag{3.17}
$$

where in the last step the eigenvalue relation B.2 was used. We can then extract the relation

$$
(V_{\mathrm{pol}})^m_\ell(r) = \frac{r}{\ell(\ell+1)}(V_r)^m_\ell(r) = \frac{r}{\ell(\ell+1)}(V^0)_{\ell m}(r)
\tag{3.18}
$$

where the fact that $V_r = V^0$ was finally used. By similar arguments, the toroidal and (when needed) spheroidal components are found to be given by

$$
(V_{\mathrm{tor}})^m_\ell = \frac{\mathrm{i}}{\sqrt{2\ell(\ell+1)}}(V^+_{\ell m} - V^-_{\ell m}) \qquad (V_{\mathrm{sph}})^m_\ell = -\frac{1}{\sqrt{2\ell(\ell+1)}}(V^+_{\ell m} + V^-_{\ell m}).
\tag{3.19}
$$

3.2 The NS model

Neutron Star interior physics is an immense topic by itself, and state of the art calculations of NS structure and transport properties have reached a high degree of refinement. Nevertheless, many mechanisms are still poorly understood, and a number of assumptions must be made for every model to be complete. Moreover, the use of an extremely detailed microphysical framework comes at high computational cost, which is problematic within a framework whose load is already high because of its inherent 3D nature.

For these reasons, the NS model implemented in `PARODY` is a fairly schematic one, modelling the crust as a completely degenerate Fermi gas of electrons. In this section, this model will be described, and the evolution equations as implemented in the code will be discussed.

As a first point, the integration domain of choice is restricted to the NS crust. This assumption stems from the idea that nucleons in the NS core quickly enter a superfluid

and superconducting state in the early cooling phases, and hence expel the magnetic field via Meissner effect. Nucleons are estimated to undergo this transition below a critical temperature of at most $\approx 8 \times 10^9$ K (Levenfish and Yakovlev, 1996). The distinctive traits of Cooper-pair formation on neutrino emission processes, which result in an enhanced cooling, have also been invoked to explain some observations (Page et al., 2011). However, the effects of superconductivity/superfluidity on the core field dynamics are not fully understood (Lander and Gourgouliatos, 2019), with some computations even suggesting that the timescales of magnetic flux expulsion are longer than the lifespan of most observed objects (e.g. Ho et al., 2017). In addition, there is no certainty about whether the superconductor is of Type-I or Type-II, with the commonly accepted model of the phenomenon of pulsar glitches requiring some field threading a Type-II superconducting core (Anderson and Itoh, 1975). In this baffling context, simulations have two paths to choose: either prescribing a simplified model of core field (e.g. Ciolfi and Rezzolla, 2013; Viganò, 2013), or turning to a completely crust-confined field (Wood and Hollerbach, 2015, again Viganò 2013). The `PARODY` model fully embraces the latter approach. At any rate, even though this choice is partially dictated by our ignorance of core physics, the crust remains the most important layer for the magnetic field evolution notwithstanding. In fact, it is the region where most charged particles are found, and can hence support strong currents, and where the Hall effect is able to shape complex field topologies.

This assumption also implies that, since we deal with a thin layer, general-relativistic effects are of limited importance. Although GR effects could be accounted for with no inherent difficulty in our equations (see e.g. Viganò et al., 2013), a proper general-relativistic treatment impacts on the boundary conditions which are imposed on the evolution equations (see Sec. 3.2.1) due to the frame-dragging of the magnetosphere. While this poses no serious problem in 2D, it becomes quite troublesome in 3D, and is expected to affect the results just quantitatively, rather than qualitatively (Pons et al., 2009).

Under these assumptions, the equations that describe the system are the Hall induction equation 2.19 and heat transport equation 2.26. In order to treat them within our code, they are written in terms of adimensional quantities. Namely, the following fiducial values of temperature, magnetic field, chemical potential and relaxation time were used,

$$\begin{aligned} T_0 &= 10^8\,\mathrm{K}, & B_0 &= 10^{14}\,\mathrm{G}, \\ \mu_0 &= 2.9 \times 10^{-5}\,\mathrm{erg}, & \tau_0 &= 9.9 \times 10^{-19}\,\mathrm{s}, \end{aligned} \tag{3.20}$$

which implies that the reference values for the number density and the conductivity $\eta = c^2/(4\pi\sigma)$ are $n_0 \simeq 2.6 \times 10^{34}\mathrm{cm}^{-3}$ and $\eta_0 \simeq 3.9 \times 10^{-4}\mathrm{cm}^2\mathrm{s}^{-1}$. These are supplemented by the star radius $R_\star = 10\,\mathrm{km}$ as the macroscopic length scale, and ohmic time $\tau_O = R_\star^2/\eta_0 \simeq 8 \times 10^7\,\mathrm{yr}$ as the reference time scale.

It is also useful to introduce four plasma length scales, which are relevant to the

electron dynamics,

$$\lambda = \left(\frac{k_{\rm B}T_0}{4\pi n_0 {\rm e}^2}\right)^{1/2} \qquad \text{Debye length} \tag{3.21}$$

$$d = \left(\frac{\mu_0}{4\pi n_0 {\rm e}^2}\right)^{1/2} \qquad \text{skin-depth} \tag{3.22}$$

$$L = \frac{\mu_0}{{\rm e}B_0} \qquad \text{Larmor radius} \tag{3.23}$$

$$l = c\tau_0 \qquad \text{mean free path,} \tag{3.24}$$

The evolution equations can be then written in adimensional form as

$$\frac{\partial \boldsymbol{B}}{\partial t} = {\rm Se}\,\boldsymbol{\nabla}\left(\frac{1}{\mu}\right)\times\boldsymbol{\nabla}T^2 + {\rm Ha}\,\boldsymbol{\nabla}\times\left[\frac{1}{\mu^3}\boldsymbol{B}\times(\boldsymbol{\nabla}\times\boldsymbol{B})\right] - \boldsymbol{\nabla}\times\left[\frac{1}{\tau\mu^2}\boldsymbol{\nabla}\times\boldsymbol{B}\right] \tag{3.25}$$

$$\frac{1}{\rm Ro}\frac{C_V}{T}\frac{\partial T^2}{\partial t} = \boldsymbol{\nabla}\cdot\left(\tau\mu^2\boldsymbol{\chi}\cdot\boldsymbol{\nabla}T^2\right) + \frac{\rm Pe}{\rm Se}\frac{|\boldsymbol{\nabla}\times\boldsymbol{B}|^2}{\tau\mu^2} + {\rm Pe}\,\mu(\boldsymbol{\nabla}\times\boldsymbol{B})\cdot\boldsymbol{\nabla}\left(\frac{T^2}{\mu^2}\right) + \frac{1}{\rm Ro}N_\nu \tag{3.26}$$

having defined

$$\chi_{ij} = \frac{\delta_{ij} + {\rm Ha}^2(\tau/\mu)^2 B_i B_j - {\rm Ha}(\tau/\mu)\epsilon_{ijk}B_k}{1 + {\rm Ha}^2(\tau/\mu)^2|\boldsymbol{B}|^2} \tag{3.27}$$

and introduced the adimensional numbers

$${\rm Ha} = l/L \simeq 50 \qquad \textit{Hall} \tag{3.28}$$

$${\rm Se} = \frac{\pi^2 L l \lambda^4}{2d^6} \simeq 0.05 \qquad \textit{Seebeck} \tag{3.29}$$

$${\rm Pe} = \frac{3d^2}{Ll} \simeq 6\times10^{-5} \qquad \textit{Peclet} \tag{3.30}$$

$$\frac{1}{\rm Ro} = \sqrt{\frac{3}{2\pi^2}\frac{\rm Pe}{\rm Se\,Ha^2}} \simeq 3\times10^{-4} \qquad \textit{Roberts.} \tag{3.31}$$

Performing adimensionalisation with these scales, the neutrino emissivity is expressed in units of $N_\nu^0 = 8\pi{\rm e}^2R^2\tau_0/\mu_0 k_b T_0 = 1.3\times10^{14}\,{\rm erg\,s^{-1}\,cm^{-3}}$.

The large thermal conductivity of the crust, which is reflected in the fact that ${\rm Ro} \gg 1$, means that on the timescale of magnetic evolution the term dependent on the heat capacity of the crust is subdominant. Hence, the exact form of the coefficient of this term, the specific heat C_V, is not important for the secular evolution: as a convenient choice, $C_V = \tau\mu^2 T$ was taken, which implies a constant effective thermal diffusivity throughout the crust. Under this assumption, equation (3.26) depends on temperature only through T^2, which proves to be an advantageous feature for numerical implementation. In fact, the specific heat is in general to be included into the operator $\mathcal{A}$ defined in Eq. 3.3 (for a simplified demonstrative setup). However, if $\mathcal{A}$ depends on the temperature (or magnetic

field) its inversion must be performed at each timestep, spoiling the efficiency of the algorithm. For this reason, the choice of a form of C_V that depends on a single power of temperature is called for in order to treat the long-term evolution. It is nevertheless a limiting assumption, which will be reassessed in Ch. 5 when dealing with short-term phenomena.

Another fundamental ingredient of a NS model is its equation of state; in Sec. 1.5.2 this term was used in its proper sense of a $p(\rho)$ relation for the matter constituents, but what is needed for our set of equations is a relation describing the structure of the object, i.e. the spatial dependence of all our variables. The crust will be assumed to be spherically symmetric, so that n is a function of the radius r alone. In principle, one should take an EoS and solve the TOV equation to get this radial profile; as some EoSs are dependent on the temperature and magnetic field, it may even be necessary to compute these profiles anew at each iteration. In this work, such an approach has not been followed for two reasons: first, since the fine details of the countless possible EoSs open a vast parameter space, the exploration of which is beyond the scope of this work; second, different EoSs lead to great variations in the core structure, but influence less the crust, which is more sensitive to the surface gravity and hence to the total mass and radius, which are in turn fixed by the core itself. On top of this, the crust structure depends on even more variables, such as the chemical composition and impurity content, with a strong degree of degeneracy between all the parameters. The equation of state is then specified as a fiducial profile for the (adimensional) chemical potential, given by

$$\mu(r) = \left(1 + \frac{1-r}{0.0463}\right)^{4/3}; \tag{3.32}$$

$\mu(r)$ increases from unity at the outer boundary ($r = 1$) to $\simeq 4.6$ at the inner boundary ($r = 0.9$). This density profile corresponds to one of the crust models computed by Cumming et al. (2004), chosen as to correspond to the typical value of the impurity parameter $Q \simeq 3$. Furthermore, an Fe-Ni crust will be assumed, without accounting for any chemical composition stratification. Moreover, the electron relaxation time τ will be assumed to be a function of r only and, in particular, taken as $\tau \equiv 1$ (in adimensional units). Taking the relaxation time τ to be independent on temperature is adequate in the lower crust, while it must be regarded as an approximation in the upper crust, where scattering is dominated by phonons (Potekhin et al., 2015). Note, nevertheless, that taking $\tau \equiv 1$, the conductivity in the upper crust corresponds to the phonon conductivity at a realistic temperature, $T \approx 10^8\,\mathrm{K}$.

The emission of neutrinos in the crust is due to a wealth of reactions. In this work, four main contributions were taken into account, namely phonon decay, neutrino pair production, neutrino bremsstrahlung and neutrino synchrotron emission

$$N_\nu(n, T, \boldsymbol{B}) = N_{\mathrm{ph}}(n, T) + N_{\mathrm{pair}}(n, T) + N_{\mathrm{bre}}(n, T) + N_{\mathrm{syn}}(n, T, \boldsymbol{B})\,. \tag{3.33}$$

The basic physics of these processes are outlined in App. A.

3.2.1 Boundary Conditions

As with all PDEs, much of the physics in our system is not actually contained in the equations themselves, but in their boundary conditions. In this case, the boundary conditions reflect a number of physical prescriptions at the boundaries between the core and the crust and at the stellar surface.

Magnetic field The assumption of complete magnetic flux expulsion from the superconducting core requires that the normal component of the magnetic field and the tangential component of the electric field must vanish at the core-crust boundary. However, the Hall term makes the latter condition nonlinear in the magnetic field. Nevertheless, this contribution is actually negligible in the high electron density layers (see Hollerbach and Rüdiger, 2004), and can hence be neglected. This allows to write the boundary conditions in terms of the radial magnetic field and of the tangential component of the current J_t only (see Eq. 2.16),

$$B_r(r_c) = 0 \qquad J_t(r_c) = 0. \tag{3.34}$$

In order to impose the outer magnetic condition, the assumption is that magnetospheric currents are negligible with respect to the ones in the crust, due to its comparatively negligible electrical conductivity, so that the external field can be considered potential. Hence, in order to match the magnetosphere the field at the surface must be potential as well,

$$\boldsymbol{\nabla} \times \boldsymbol{B}|_{r=R_\star} = 0. \tag{3.35}$$

This equation is actually not difficult to solve in our setup: in fact, having already decomposed the field in poloidal and toroidal components and further expanded it in spherical harmonics, it reduces to requiring that no toroidal field is present and that each poloidal mode decays as $(B_{\rm pol})^m_\ell \propto r^{-(\ell+1)}$. Hence, the boundary condition is rewritten as

$$\begin{aligned} &\frac{\partial}{\partial r}(B_{\rm pol})^m_\ell + \frac{\ell+1}{r}(B_{\rm pol})^m_\ell \bigg|_{r=R_\star} = 0; \\ &(B_{\rm tor})^m_\ell|_{r=R_\star} = 0. \end{aligned} \tag{3.36}$$

Temperature Whereas the core can be completely excluded from the domain of integration of the field equation, its effects on the temperature evolution cannot be discarded. Even without solving its full thermal evolution, the role of the core as the main heat reservoir of the star must be taken into account, since it sets the overall temperature scale of the crust. Nonetheless, the core is expected to have an extremely large conductivity, so that it can be treated as isothermal to a very good measure (Potekhin et al., 2015). Its thermal evolution can then be implemented as a prescribed time evolution of the temperature at r_c, which evolves by neutrino emission according to a version of Eq. 2.5,

$$\frac{\partial T_c}{\partial t} = -\frac{N_c(T)}{C_c} \tag{3.37}$$

where C_c is the core specific heat and $N_c(T) = N_0 T^k$ the total neutrino emissivity from the core. In the following, this condition is implemented assuming a standard slow-cooling scenario (Page et al., 2004), namely taking $k = 8$, $C_c = 10^{20}\,\mathrm{erg\,s^{-1}\,K^{-1}}$, $N_0 = 10^{21}\,\mathrm{erg\,K^{-8}}$.

The surface temperature is controlled by the heat blanketing envelope described in Sec. 2.1.1. Assuming that no energy sources or sinks are present in the envelope, the temperature gradient at the top of the crust is given by (Tsuruta and Cameron, 1966a)

$$-\left(\boldsymbol{k}\cdot\boldsymbol{\nabla}T\right)\cdot\hat{\mathbf{r}} = \sigma_{\mathrm{SB}}\,T_s^4(T_b,\mathbf{B})\,, \tag{3.38}$$

where $\hat{\mathbf{r}}$ is the radial unit vector. The relation between the surface temperature T_s and the one at the bottom of the envelope T_b used in this work is the one given by Eq. 2.12.

3.2.2 Timestep Control

Since part of the time advance algorithm is explicit, the timestep is to be chosen in order to fulfil the Courant condition, ensuring that the algorithm cannot "evolve" faster than the differential equation itself, i.e. that the time it takes for a wave to traverse a cell should not be smaller than the timestep. In particular, three limits were considered,

$$\Delta t < \frac{1}{2}\min\left[\left(\frac{4\,\Delta x^2}{\eta}\right)^{\frac{1}{3}}\left(\frac{n_e\,\Delta x}{\mathrm{Ha}\,B}\right)^{\frac{4}{3}},\quad \frac{1}{\eta}\Delta x^2,\quad \frac{C_V}{2k}\Delta x^2\right] \tag{3.39}$$

where $\eta = c^2/4\pi\sigma$ is the resistivity, k the scalar part of the thermal conductivity and Δx measures the maximum width of a cell. The first limit comes from the Hall term, the second from the Ohm one and the third from heat diffusion (in which case the timestep represents the heat diffusion time). This condition is computed in the real space for each point, and the timestep gets adjusted accordingly. The last contribution must actually be considered only when heat diffusion is treated explicitly, which will only be done in the version of the code described in Sec. 5.2 in order to treat short-term phenomena; when heat diffusion if treated implicitly the timestep is determined by the two terms derived from the induction equation (typically the one related to the Hall term). In the latter cases, the timestep ranges between $\approx$ days and $\approx$ years depending on the resolution. In Ch. 5, where the short term evolution will be assessed, the Courant condition related to heat diffusion will have to be properly considered; the model will also be extended to lower densities, so that the timestep values will go down to fractions of an hour.

3.2.3 Computational Details

Once the algorithm is set and implemented, the code must be run as efficiently as possible. To this end, the code has been compiled using the more up-to-date version of the Intel© `FORTRAN` compiler, running the code on modern HPC facilities. Such machines allow one to fully exploit the parallel nature of the code; the typical radial resolutions used were of ≈ 100 points, meaning that ≈ 30 processes were to be started at once to run the code with the requirement that at least 4 points are treated by the same process, necessary for

it to compute derivatives. Note that this puts a limit on the number of processes that can be used before the radial resolution becomes unreasonably high; this is in contrast to codes following different approaches, which run on hundreds if not thousands of parallel processes.

The angular resolution is set by the maximum number of modes, which is typically in the range $[100, 200]$. This corresponds to a resolution of several tens of meters on the surface. With these values, a run adapted to the long term evolution lasted for several wall-clock days, producing several GiB of data in the form of unformatted files. Neutrino emission, in particular, is of huge computational cost, since the fits used to describe it are quite involved; their inclusion has the effect of approximately doubling the runtime.

3.3 From the surface to the observer: GR ray-tracing

One of the final outputs of a magnetothermal simulation is the surface temperature map. This cannot, however, be directly compared to observations, since the current instrumentation (as well as the one planned in any foreseeable future) has not high enough resolution to produce a spatially resolved picture of the NS. Instead, the total observed thermal flux, which mostly lies in the X-ray band, is studied as a function of the rotational phase (pulse profile) and frequency (spectrum), allowing the surface properties to be deduced *a posteriori*.

Hence, to link simulations and data the flux as received by an observer at infinity must be computed. Even though GR effects were neglected when computing the evolution in the thin crust, this is not possible any more when considering the propagation of light across the magnetosphere and beyond, so that an approach taking into account both gravitational ray-bending and gravitational frequency redshift is required. Note that one of the effects of ray bending is to move the *terminator*, i.e. the line dividing the in-sight and out-of-sight portions of the star, so that more than 50% of the surface is visible; this has the effect of reducing the observable variations with the phase for a given non-uniform map.

This task has been achieved using the `IDL` ray-tracing code originally developed by Zane and Turolla (2006, see also Taverna et al. 2015; Popov et al. 2017). The code divides the star surface into a grid, associating to each patch the co-latitude Θ and azimuth Φ of its centre in the observer's frame XYZ, with the Z-axis along the line-of-sight (LOS) and the X-axis in the plane of the LOS and the star spin axis $\mathbf{\Omega}$. Then, only the photons propagating along the LOS are selected, and the contributions of all the patches which are in view at a given rotational phase γ are collected.

Assuming the metric outside the NS to be Schwarzschild's, Eq. 1.19, in vacuum, the phase- and energy-dependent radiation flux at the observer is then obtained by integrating the specific intensity over the surface,

$$F_\nu(\gamma) = (1-x)\frac{R_{\rm NS}^2}{D^2}\int_0^{2\pi} \mathrm{d}\Phi \int_0^1 I_\nu \,\mathrm{d}u^2 \,, \tag{3.40}$$

where the redshift factor is defined as $x \equiv 2GM_{\rm NS}/c^2R_{\rm NS}$, $M_{\rm NS}$ and $R_{\rm NS}$ are the star

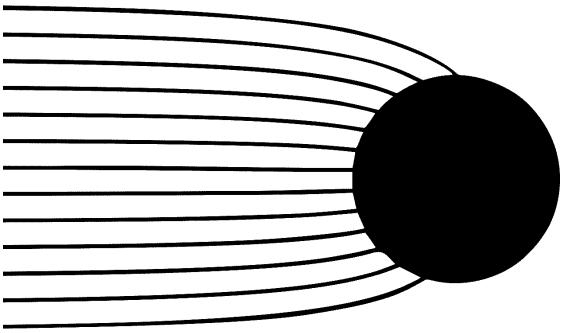

Figure 3.1: Cartoon outlining the propagation of light around a NS due to GR ray-bending.

mass and radius, c is the speed of light and D is the source distance. The geometrical integration is done over the azimuth Φ and $u \equiv \sin\bar{\Theta}$; this is not the colatitude Θ as measured by a stationary observer on the surface, but its value at infinity,

$$\bar{\Theta} = \int_0^{1/2} \frac{\mathrm{d}v \, \sin\Theta}{[(1-x)/4 - (1-2vx)v^2 \sin^2\Theta]^{1/2}} \, ; \tag{3.41}$$

this integral incorporates the ray-bending effect. In Eq. 3.40, the frequency ν is the one measured by a static observer at the stellar surface, whereas the frequency at infinity is $\nu_\infty = \nu\sqrt{1-x}$. The specific intensity I_ν follows once an emission mechanism is specified. It depends in general on the photon propagation direction, as well as on the local temperature and magnetic field strength and direction.

Moreover, the geometry of the source must be specified. This is given by two angles, one representing the direction of the rotation axis and one the direction of the magnetic field. If the field is axially symmetric, the choice of a magnetic axis is trivial, as it coincides with that of the dipole component, $\boldsymbol{b}_{\rm dip}$; in more complex topologies, a choice must be made. In the non symmetric cases presented in Sec. 4.3, the choice was to take the field axis to be that of the quadrupole component, $\boldsymbol{b}_{\rm quad}$. In this framework, the angular coordinates θ and ϕ in the magnetic axis system can be expressed in terms of those in the observer's frame, Θ and Φ, via the angle χ between the rotation axis $\hat{\boldsymbol{\Omega}}$ and the LOS and and ξ (ψ), the angle between $\hat{\boldsymbol{\Omega}}$ and $\boldsymbol{b}_{\rm dip}$ ($\boldsymbol{b}_{\rm quad}$) (see Taverna et al., 2015, for more details). The choice of $\boldsymbol{b}_{\rm quad}$ rather than $\boldsymbol{b}_{\rm dip}$ causes no loss of generality, since it can be easily shown that $\psi = \xi \pm \Theta_{\rm q}$, where $\Theta_{\rm q}$ is the angle between $\boldsymbol{b}_{\rm dip}$ and $\boldsymbol{b}_{\rm quad}$ (see again Sec. 4.3).

The angular resolution of the ray-tracer was set to the one employed by `PARODY` to obtain the thermal map; the angles χ and ξ (ψ) were than taken on a 21×21 evenly spaced grid, and the observed spectrum was computed for 30 evenly spaced phase values. The chosen energy band lies in the X-rays, $0.1 - 3\,\mathrm{keV}$ with a 50-point evenly spaced grid.

CHAPTER 4

Secular 3D Magnetothermal Evolution

When addressing the long-term properties of a NS, such as the evolution of its thermal emission and of its period, the magnetic field strength and topology is absolute key. This is particularly true for the strongly magnetised NSs, which have estimated lifetimes of several kyr, a timescale on which the Hall effect is playing the most important part in the evolution. In this section, the evolution of the magnetic field on this secular scale will be discussed. The evolution of an initially purely dipolar field will be presented as a first reference case (Sec. 4.1); then, cases with no particular symmetry will be addressed. This lack of symmetry can arise from an instability of an initially symmetric field (Sec. 4.2), or be imposed from the beginning (Sec. 4.3). The information on the emission gathered in the frame of the object will then be linked to observable quantities computing light propagation around the NS taking into account GR bending. The results presented in Sec. 4.1 and Sec. 4.3 have been published in De Grandis et al. (2020), whereas those in Sec. 4.2 in De Grandis et al. (2021).

4.1 An axisymmetric example: the Hall attractor

As with most problems in physics, the result of the simulations in this Thesis will crucially depend on the initial conditions. In particular, the choice of the initial magnetic field is critical to address its evolution. Unfortunately, models of core-collapse supernovæ are not able to provide as yet a robust mechanism for the field amplification up to NS values, let alone give an indication of what the magnetic geometry may be.

By a simple argument of field flux conservation (e.g. Woltjer, 1964), one may indeed expect stellar fields (for example, $B_\odot \approx 100\,\mathrm{G}$) to be amplified by a factor $(R_\mathrm{star}/R_\mathrm{NS})^2 \approx 10^{10}$, reaching NS-like fields. It is also worth noting how the magnetic flux of magnetised main sequence stars, white dwarfs and NSs is observed to be of a remarkably similar order of magnitude, $\Phi \approx 10^{5.5}(R/R_\odot)^2\,\mathrm{Mx}$ (Reisenegger, 2003) despite the great differences between those objects. On the other hand, magnetic flux conservation in a cataclysmic event such as a SN explosion is for sure an oversimplification, and in any case the

most extreme observed magnetar fields ($B \gtrsim 10^{14} - 10^{15}\,\mathrm{G}$) are so strong that even under this assumption their formation poses some problems. Thus, models relying on field amplification through dynamo effects were introduced (Duncan and Thompson, 1992), in which the field gets greatly amplified in the first milliseconds of the proto-NS phase. Several such mechanisms have been proposed, involving other possibilities, like high mass, strongly magnetised progenitors (the *fossil field* scenario, Ferrario and Wickramasinghe 2008), dynamical processes in a pre-supernova binary system (Clark et al., 2014), precession-driven dynamos (Lander, 2021) or magneto-rotational instabilities (Reboul-Salze et al., 2021).

In any case, there remains a knowledge gap between the early phases models (before the solidification of the crust) and the long term ones, with a stratified and hydrostatically stable object and a superfluid core (whether or not threaded by a field). The widespread approach is then to assume that the field amplification is fast enough that by the time of the crust solidification the star has reached some kind of MHD equilibrium. In this work, the initial field was set to a large scale mode (Rüdiger et al., 2013); in particular, such fields were built with the form $B_{\ell m} \propto \zeta_\ell(r)/r$ where $\zeta_\ell(r)$ is a combination of Bessel functions adapted to the boundary conditions, which is a method used to obtain force free-fields (see App. D for details); an analogous approach has been used by Aguilera et al. (2008); Viganò (2013).

The very first case that will be considered is the simplest one, namely an initially pure poloidal dipole ($\ell = 1$, $m = 0$) with $B_{\mathrm{dip}}(0) \approx 3 \times 10^{13}\,\mathrm{G}$. A batch of test runs was carried out to check that with such an initial condition the axial symmetry (as well as the north-south symmetry) is maintained to machine precision, i.e. there is no energy transfer to the $m \neq 0$ orders. Hence, the equations were not solved in the whole crust, but the domain could be safely restricted to a spherical wedge with periodic boundary conditions at the sides. In the spectral domain, using a wedge which is $1/n$th of the crust corresponds to taking to be equal all the modes for which the order has the same $m \mod n$. In this case, a wedge encompassing 1/6th of all the longitudes has been considered.

In this run, core cooling was switched off and the core temperature kept at a constant value and keeping it fixed at the crust-core interface. This is not expected to have a direct effect on the consistency of the final surface thermal maps: in fact, the core thermal evolution sets the overall temperature scale of the star, but does not directly affect its topology, which is dictated by the magnetic field. This is again true in the long term, and due to the large thermal conductivity of the crust (i.e. the large value of the Ro number). In particular, the initial temperature value has been set in this case to $T = 4.5 \times 10^7\,\mathrm{K}$. This choice was made in light of the application to real sources described in Sec. 4.1.1,

The evolution of the dipolar component of the field is shown in Fig. 4.1 (left). Throughout the Hall phase, $t \lesssim 10^5\,\mathrm{yr}$, its value hardly changes, while it decreases by an order of magnitude in $t \approx 10^6\,\mathrm{yr}$, as the ohmic dissipation takes over. This value can be used to compute the spin-down evolution, Eq. 1.3, and follow the trajectory of the object on the $P\dot{P}$ diagram. This is shown in Fig. 4.2 for an initial period of 10 ms and standard NS parameters; at first, the trajectory runs parallel to a constant B_{dip} line, to then bend

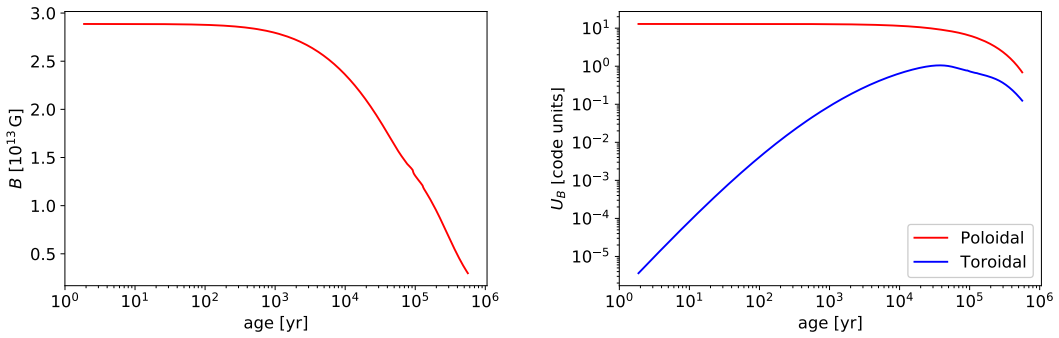

Figure 4.1: (*Left*) Evolution of the value of the dipolar component at the NS surface. (*Right*) Evolution of the total magnetic energy in the two field components.

towards lower $\dot{P}$ values as the field decreases.

An analogous behaviour can be found in the evolution of the magnetic energy, Fig. 4.1 (right). As already mentioned, the Hall term is able to transfer energy between poloidal and toroidal components, which can be seen in this case considering the growth of the contribution of the toroidal field to the total energy. Moreover, the importance of a toroidal field has been suggested as an important factor for the MHD stability of a system (e.g. Lander, 2013). Two snapshots of the field geometry at early and late times are shown in Fig. 4.3. As a general feature, the Hall evolution tends to form equatorial structures in which the poloidal field is enhanced and creates closed field line loops. These features are on smaller scales than the large dipole, reflecting the energy transfer to lower modes. A toroidal field is swiftly formed and keeps growing, especially in the lower crustal layers; however, it keeps outside of the equatorial region, without developing marked small scale structures.

As the energy transfer to the smaller scales is the distinctive feature of the Hall effect, it is worth examining it in detail. In fact, Gourgouliatos and Cumming (2014) studied the characteristic of this energy cascade finding a configuration known as the *Hall attractor*, in which odd-ℓ multipoles dominate over even ones. Fig. 4.4 shows the evolution of the energy content on the first seven modes to test this scenario. As expected, despite initially growing at similar rates after some Hall times the even modes (most notably the $\ell = 4, 6$ ones) get suppressed with respect to the odd neighbouring ones; hence, the configuration reached at this point in time brings the resemblance of the Hall attractor, which are then washed away on much longer timescales by the takeover of ohmic dissipation. In fact, the Ohm term acts more effectively on high-ℓ modes, so that the eventual configuration one expects after several τ_O is again purely dipolar. In this work, such long timescales were not reached for a number of reasons: on a practical side, they would require extremely long computational times; besides this, they would describe a cold, decayed objects which has no more detectable activity and as such limited astrophysical interest; finally the very fact that small scale structure get suppressed limit

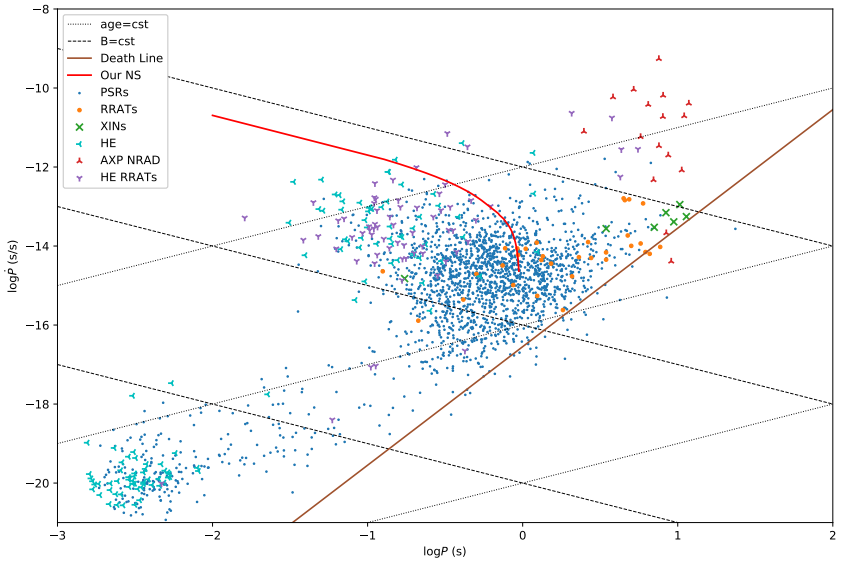

Figure 4.2: Evolution of the NS in the $P\dot{P}$ diagram obtained from the Larmor formula Eq. 1.3 and the dipole evolution profile from Fig. 4.1 with standard NS parameters, $I = 10^{45}\,\mathrm{g\,cm^2}$, $R_\star = 12\,\mathrm{km}$, $\sin\xi = 1/2$. The brown line represents the radio pulsar *death line*, below which radio emission mechanisms are expected to turn off, as parametrised in Gourgouliatos and Hollerbach (2018).

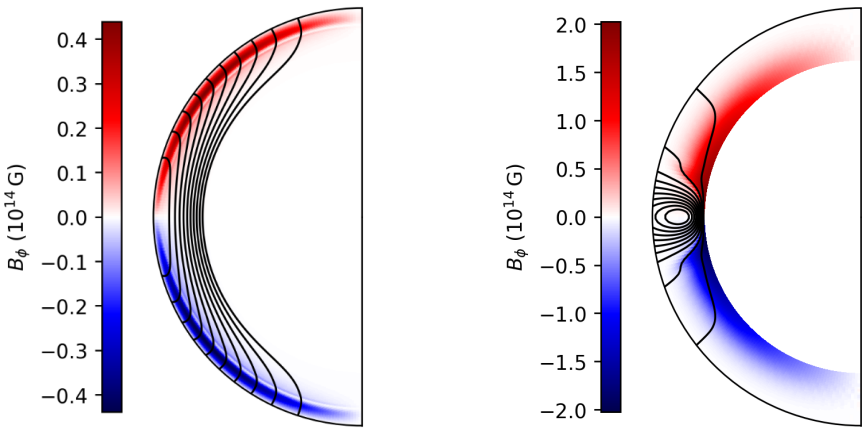

Figure 4.3: Two snapshots of the evolution of the magnetic field at an early time ($t \simeq 2\,\mathrm{kyr}$, left) and in a later phase ($t \simeq 400\,\mathrm{kyr}$, right). The poloidal field is marked by its field lines, whereas the toroidal one corresponds to the ϕ component shown in colour (note that this identification is only valid in axial symmetry, see Sec. 3.1.2). In the first case, the value of the surface dipolar field is still $\simeq 3 \times 10^{13}\,\mathrm{G}$, whereas in the latter it has decayed down to $\simeq 4 \times 10^{12}\,\mathrm{G}$. Here and in all similar plots hereafter, the crust width is enhanced by a factor 4× to improve visualisation.

the interest of this case for a multi-dimensional approach. Note that the capability to follow the evolution of each mode allows a consistency check by looking at the evolution of the $\ell = 0$ mode (the monopole), which should always be found to be zero as required by the condition $\boldsymbol{\nabla} \cdot \boldsymbol{B} = 0$.

The internal temperature structure and external thermal map for the same times previously considered are shown in Fig. 4.5. There are two ways in which the magnetic field is shaping temperature: via its evolution inside the crust and its effect on the conduction through the envelope. In the crust, the field is dissipating energy where currents are present and at the same time thermal conduction is preferentially driven along field lines, and suppressed across them. Field lines hence act as a thermal insulator, which is particularly effective in case of closed loops. In fact, a closed field line must be supported by a current which gives rise to Joule heating; the heat thus generated is then effectively trapped inside the line. In the case at hand, this mechanism originates an equatorial hot belt, which gets more and more pronounced as time elapses and the equatorial field structure develops. The fact that field lines thwart heat transfer across themselves is of paramount importance when considering the envelope: in fact, it is the strong heat gradient in this region that determines the final thermal structure of the surface. Therefore, even though the equatorial belt in the crust is hotter, this does not automatically translate into an hot equatorial belt on the surface. The field lines of the outer potential field run parallel to the surface at the equator, so that heat transport is extremely poor and what is observed is a *colder* equatorial belt. This effect has

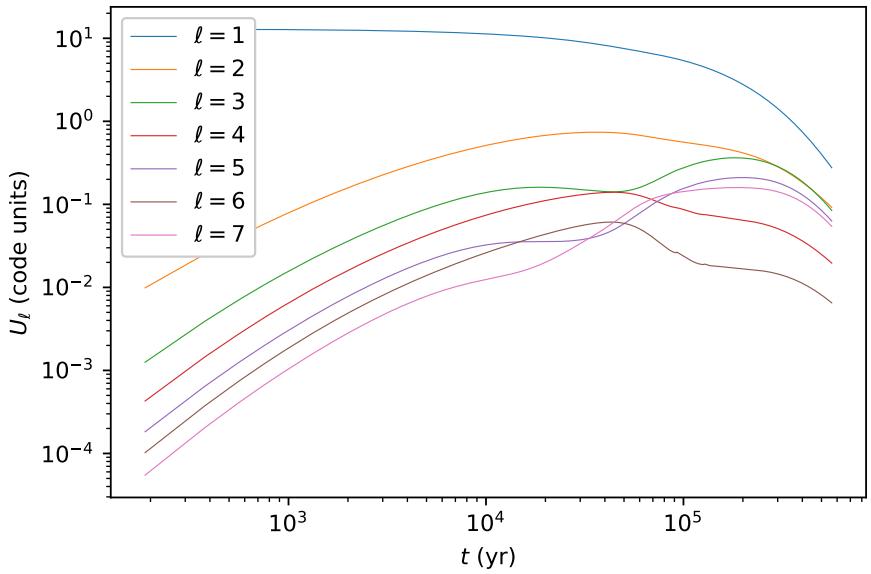

Figure 4.4: Time evolution of the energy in the first 7 ℓ-modes for an initially dipolar field.

been computed in this work adopting the practical fits for a magnetised envelope given by Potekhin and Yakovlev (2001), but very recently Kondratyev et al. (2020) found a qualitatively similar "inversion" effect using state-of-the-art 3D models of NS envelopes.

In the early phases, the temperature anisotropy inside the crust is not very pronounced, so that the magnetic screening effect dominates and the resulting thermal map has two hotter regions at the poles, with the temperature monotonically decreasing towards the equator. This kind of surface map is the one resulting from a pure dipole, and is well known in the literature (e.g. Greenstein and Hartke, 1983, see also Page 1995; Popov et al. 2017). In contrast, in more evolved configurations the equatorial "heat trap" mechanism of closed field lines becomes very effective and the thermal gradients in the crust become much stronger. As a consequence, the magnetic screening of the hot region is not total, and a more structured surface thermal map is produced, with two warm polar regions, a thin equatorial cold ring and two hot belts at the intermediate latitudes. As for the magnetic field, this configuration is expected to eventually turn back to a dipole on ohmic timescales, which are not reached in the present work.

With all the information in the thermal map, the thermal emission and its observational quantifiers can be addressed. This has been done by using the ray-tracing GR code described in Sec. 3.3: with the thermal map as an input, the spectrum received by an observer at infinity (i.e. with gravitational redshift, for which standard NS values $M = 1.4 M_\odot$, $R = 12\,\mathrm{km}$ were used) was computed as a function of the rotational phase and the viewing angles χ and ξ. Using the same notation introduced in Sec. 3.3, χ represents the angle between the spin axis and the LOS and ξ the angle between the spin

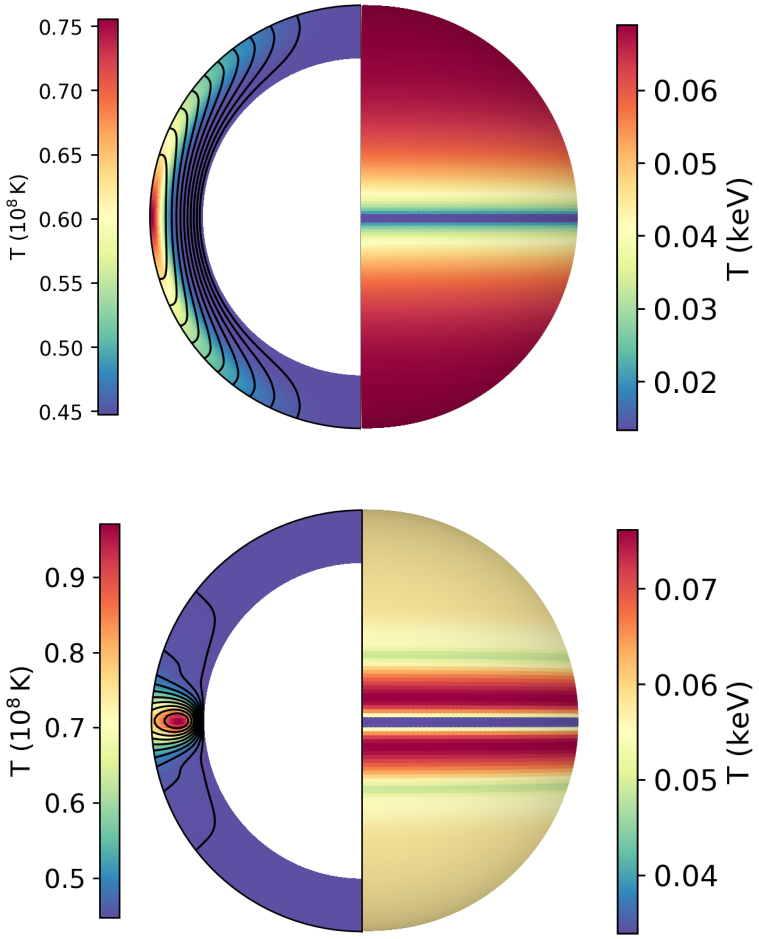

Figure 4.5: Two snapshots of the evolution of the temperature in the same conditions shown in Fig. 4.3. The left hand side of each plot shows the temperature structure inside the crust, with the poloidal field lines superimposed; the right hand side the corresponding surface thermal map, i.e. after applying Eq. 2.12).

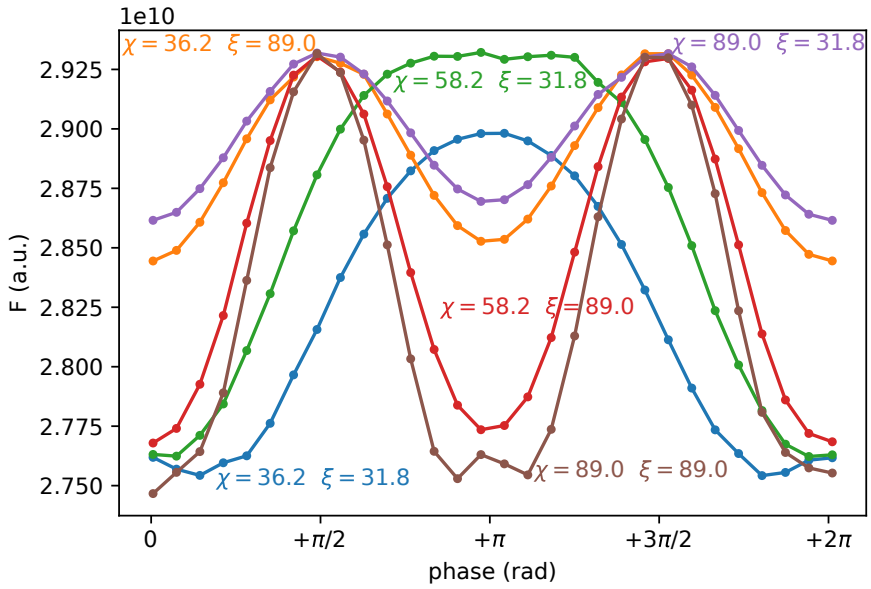

Figure 4.6: Pulse profiles in the $0.1-3\,\mathrm{keV}$ energy band at $t \simeq 400\,\mathrm{kyr}$ for selected values of the two geometrical angles; each curve is labelled by the corresponding values of χ and ξ (in degrees).

and the magnetic axes.

Some of the pulse profiles thus obtained, which correspond to the phase-resolved spectrum computed by the ray-tracer integrated over all frequencies, are shown at the later stage in Fig. 4.6 for some representative values of the viewing angles. The profiles reflect the high degree of symmetry of the map, as they are symmetric with respect to the middle phase with a quasi-sinusoidal shape. For the cases in which the hot belt crosses the LOS more than once in a period, a double-peak curve is obtained, whereas it stays single-peaked otherwise.

A convenient quantity used to characterise each light curve is its pulsed fraction PF, defined as

$$PF = \frac{F_{\max} - F_{\min}}{F_{\max} + F_{\min}}, \tag{4.1}$$

where $F_{\max}$ ($F_{\min}$) is the maximum (minimum) of the flux, integrated over a given energy band, attained in a whole rotational period (note that in some conventions a factor $1/2$ is included). Finally, an emission model must be specified, which in this case is taken to be a blackbody

$$F(E) = E^3 \left[\frac{A}{\exp(E/T) - 1}\right], \tag{4.2}$$

where the factor A is directly proportional to the area of the emitting patch at temperature T and inversely proportional to the squared distance of the source. Since the latter cancels out in the ratio, the PF depends only on the thermal map, the viewing angles

and the selected energy band; the energy band considered here is that of the soft X-rays, $0.1 - 3\,\mathrm{keV}$, where emission from middle aged, cooling NSs peaks (e.g. Page, 1995). This choice has been made in order to study the relation between the pulsed profile and the thermal map in as simplest and direct a way as possible, without introducing additional anisotropy in the emission pattern itself; moreover, these calculations will be compared in the following to sources that show an essentially thermal spectrum (see Sec. 4.1.1). No absorption due to the interstellar medium has been considered.

Fig. 4.7 shows how the maximum PF (i.e. the one for the most favourable viewing geometry; the minimum one is always $\simeq 0$) evolves in time, alongside its dependence on the viewing angles χ and ξ. The PF peaks early on in the evolution ($t \simeq 25\,\mathrm{kyr}$), when the highest temperature anisotropy in the crust is reached, to then slowly decrease as the crust becomes more isothermal and the field is pushed back to a pure dipole by ohmic dissipation. As one may expect for such a symmetric configuration, the overall value is anyway quite low, $PF \lesssim 5\%$. Indeed, models of GR propagation put an upper limit to the maximum PF in an axisymmetric model, which can reach up to $\sim 10\%$ for comparable star mass and radius if the emission model is isotropic (Page, 1995); the result obtained here is well within this limit. The temperature north-south symmetry is, instead, manifested in the invariance of the PF upon exchange of the χ and ξ angles, i.e., the symmetry along the diagonal in the χ, ξ contour plots shown in Fig. 4.7.

4.1.1 Is RX J1856.5-3754 in a Hall Attractor Phase?

So far, the analysis of the emission has been restricted to phase-resolved, energy-integrated lightcurves. However, the computation provides the full phase-resolved spectra, see an example in Fig. 4.8, that will now be discussed. In doing so, the results will be analysed in view of the comparison with a specific source, RX J1856.5-3754, that shows peculiar spectral properties that resonate with the characteristics of the case at hand.

RX J1856.5-3754 is the first-discovered and brightest source in the class of X-ray Isolated NSs (XINSs). This class is comprised of a small number of objects; to date, only seven of them are known (hence the nickname "magnificent seven", M7) even though other candidates are being studied (see e.g. the recent study by Rigoselli et al., 2021). The characteristics that these objects in their own separate class are (Turolla, 2009):

- thermal X-ray emission ($T \sim 50 - 100\,\mathrm{keV}$), with no hard power law component;
- faint optical counterparts, implying an exceedingly unbalanced X-ray to optic flux ratio, $F_X/F_o > 10^4$; no detectable radio emission (although a short-wavelength pulsed radio emission has been claimed for two objects Malofeev et al. 2007);
- no association with a companion or a supernova remnant;
- pulsation periods laying in a narrow range, $3 - 12\,\mathrm{s}$;
- somewhat low pulsed fractions , $1\% \lesssim PF \lesssim 30\%$.

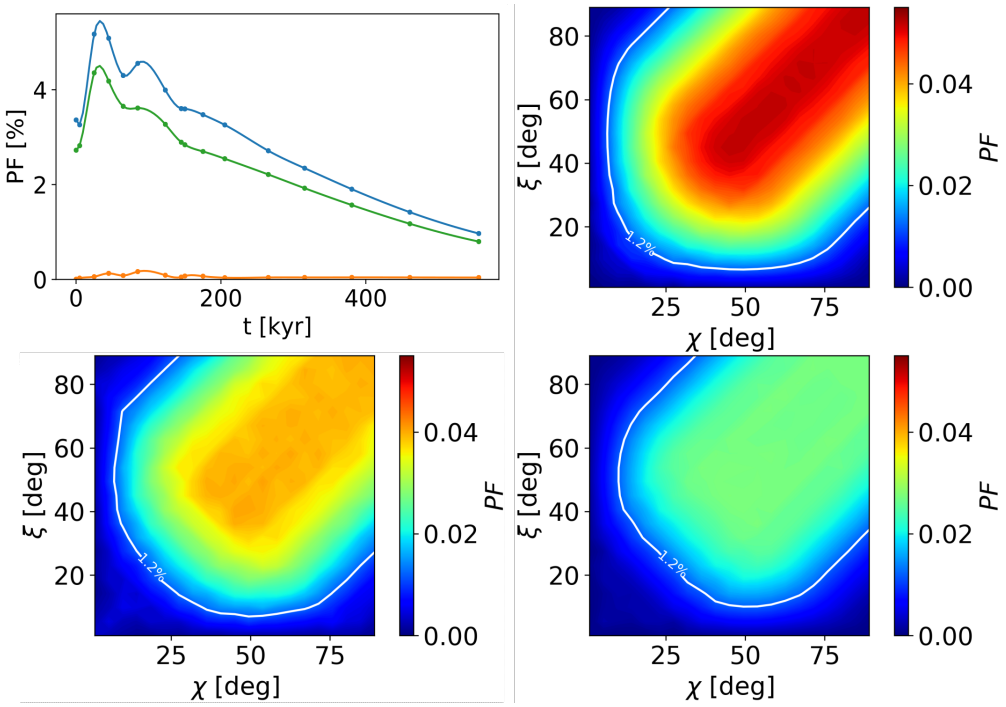

Figure 4.7: Pulsed fraction as a function of time for an axisymmetric field. The three evolution curves correspond to the viewing angles $\chi = 90°$, $\xi = 90°$ (blue, the maximum value), $\chi = 36.2°$, $\xi = 31.8°$ (green, see Sec. 4.1.1) and $\chi = 90°$, $\xi = 0°$ (orange). Contour plots show the dependence on the viewing geometry at the selected ages, 25 kyr (top-right), 123 kyr (bottom-left) and 265 kyr (bottom-right). The contour line at $PF = 1.2\%$ corresponds to the value observed for RX J1856.5-3754 (see again Sec. 4.1.1).

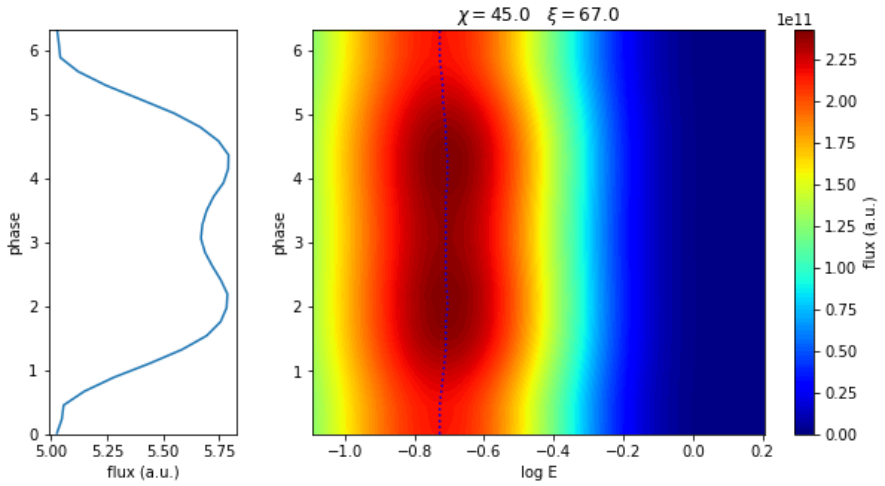

Figure 4.8: Example of fully phase- and energy-resolved spectrum at $t \simeq 400\,\mathrm{kyr}$ (right panel). The blue dotted line shows the value at which the spectrum peaks at each phase. The left panel shows the energy integrated, phase-resolved pulse profile, obtained by summing over the energy range.

The X-ray flux does not show any long term variability, with the exception of RX J0720.4-3125, that shows a cyclic variation with a period of several years (de Vries et al., 2004; Haberl et al., 2012). This very simple, thermal emission makes the M7 an ideal target for the comparison with magnetothermal simulation.

In particular, RX J1856.5-3754 is one of the most well-studied sources in the group: in fact, since its discovery in the Rosat All Sky Survey by Walter et al. (1996), it has been targeted by the *XMM-Newton* and *Chandra* satellites (see Sartore et al., 2012, for a comprehensive analysis of existing data). Its emission is pulsed with a period of $P \sim 7\,\mathrm{s}$ with a very low pulsed fraction, $PF \sim 1.2\%$ (Tiengo and Mereghetti, 2007). Unfortunately, the lack of accurate measurements of the period derivative $\dot{P}$ prevented up to now a robust estimate of the B-field: van Kerkwijk and Kaplan (2008) gives a spin-down value of $B \simeq 1.5 \times 10^{13}\,\mathrm{G}$, whereas a quite lower value, $B \simeq 3 - 4 \times 10^{12}\,\mathrm{G}$, has been inferred by Ho et al. (2007) using spectral fitting with atmospheric models. For the same reason, the age of RX J1856.5-3754 is not unambiguously estimated: the spin-down age is $\tau_\mathrm{c} \approx 4\,\mathrm{Myr}$, which is in contrast with dynamical estimates, based on the identification of the NS birthplace, which set it shorter by an order of magnitude, $\tau_\mathrm{dyn} \sim 4 \times 10^5\,\mathrm{yr}$ (Tetzlaff et al., 2011; Mignani et al., 2013).

RX J1856.5-3754 exhibits a purely thermal spectrum, not presenting the absorption features observed in the other sources of the group (Haberl et al., 2003; van Kerkwijk et al., 2004; Haberl et al., 2004; Zane et al., 2005). Through the analysis of a large set of *XMM-Newton* data, Sartore et al. (2012) proposed a best fitting spectral model

comprised by two blackbody components,

$$F(E) = E^3 \left(\frac{A_1}{\exp\left(E/T_1\right) - 1} + \frac{A_2}{\exp\left(E/T_2\right) - 1} \right) \tag{4.3}$$

with (redshifted) temperatures and radiation radii

$$\begin{array}{lll} T_1 = 62.4\,\mathrm{eV} & T_2 = 38.9\,\mathrm{eV} & (T_2/T_1 \simeq 0.59) \\ R_1 = 4.7 \left(\dfrac{d}{120\,\mathrm{pc}} \right) \mathrm{km} & R_2 = 11.8 \left(\dfrac{d}{120\,\mathrm{pc}} \right) \mathrm{km} & (A_2/A_1 \simeq 6.3) \end{array}$$

where the distance d has been scaled to a value compatible to the estimated distance of 123^{+11}_{-15} pc (Walter et al., 2010), which makes RX J1856.5-3754 the closest of the M7.

This simple form of the spectrum, combined with the very low $PF \sim 1.2\%$, suggests that RX J1856.5-3754 harbours a simple, symmetric field. Nevertheless, the results of the fit present a peculiarity: the area of the hotter component is smaller than the area of the cold one. This may not sound surprising for an object with a small, hot emitting polar cap as is observed in many pulsars, but seems at odds with the tiny pulsed fraction. Although the viewing angles may certainly be in a particularly unfavourable arrangement, the model described in the following will present an explanation of this characteristic that does not require such a fine tuning.

To test this possibility, the synthetic spectra obtained with the ray-tracer were fitted with a double BB using an expression analogous to Eq. 4.3, taking as variables the two temperatures (with T_1 always being the higher one) and the ratio of the areas (so that the distance dependence can be factorised out as a overall normalisation constant). The spectra at all ages were found to be indeed well fitted with this expression; Fig. 4.9 shows the parameters obtained for this fit during the evolution. The ratio of the two temperatures changes over time, yet stays in a comparatively small range. On the other hand, the ratio of the areas starts below 1 (i.e., the hotter component is larger, as it would be expected for a simple dipole-like configuration), to then grow above this value after some kyrs.

At this point, it should be noted how the values selected at the beginning for this example run were chosen in order to match RX J1856.5-3754 at the age of 400 kyr, close to the dynamical age: the dipolar surface field is $\simeq 4 \times 10^{12}$ G, close to the spectral estimate by Ho et al. (2007), and the hotter temperature $T_1 = 62.1$ eV is in agreement with the measurements.

In particular, the spectral fit at 400 kyr returns a value of the hotter component area which is *smaller* than that of the colder one. With the additional requirement that the computed PF matches the observed value of $PF \simeq 1.2\%$, the values turns out to be $T_2/T_1 \approx 0.76$ and A_2/A_1 ranging between 6.0 and 6.7, depending on the selected source geometry (see Fig. 4.10). Fig. 4.11 shows the fit for $\chi = 36.2°$ and $\xi = 31.8°$, which was chosen as the "best" geometry since it yields $PF \simeq 1.2\%$ with a ratio $A_2/A_1 = 6.3$, which is the closest to observations among the sample. These results are indeed in broad agreement with the observations, even though the systematic errors associated to the simplifying assumptions of the theoretical model restrain a statistically significant comparison between this synthetic spectrum and observations.

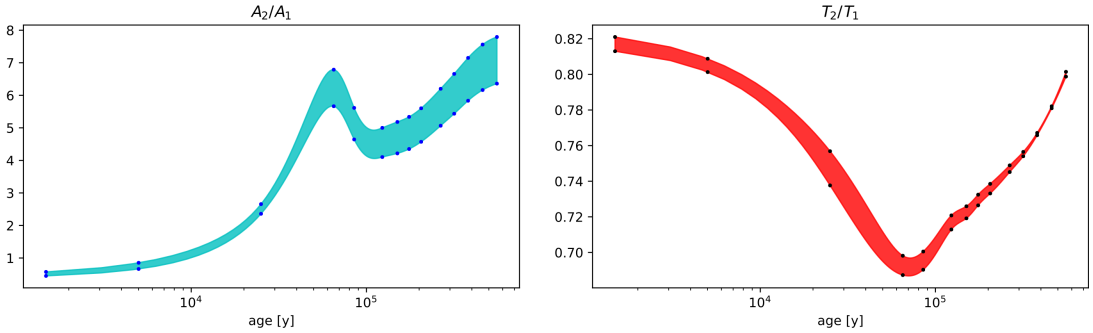

Figure 4.9: Evolution of the T_2/T_1 and A_2/A_1 ratios extracted by fitting the synthetic spectra with the double BB at selected times (results are connected through spline curves). The ranges correspond to all the possible viewing geometries considered in the grid.

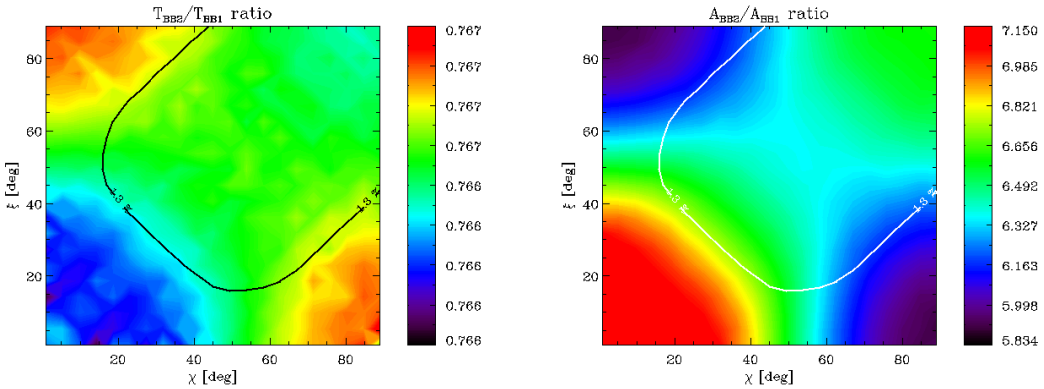

Figure 4.10: Ratios T_2/T_1 and A_2/A_1 as a function of the viewing angles for the synthetic spectrum at $t \simeq 400\,\mathrm{kyr}$.

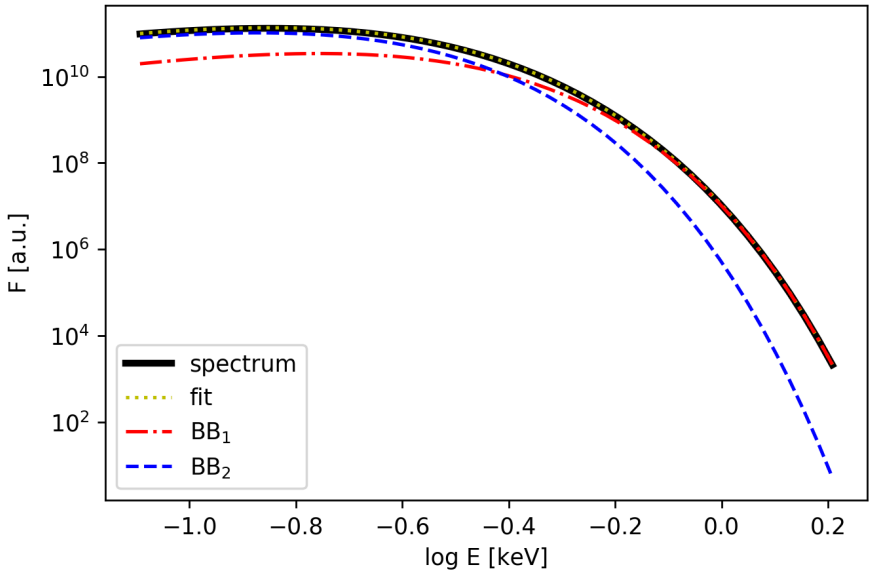

Figure 4.11: Phase-averaged synthetic spectrum of RX J1856.5-3754 (black-solid curve) computed at $t \simeq 400\,\mathrm{kyr}$ with the best fitting BB+BB model (yellow-dotted curve, nearly indistinguishable from the calculated spectrum) and the single hotter (red dash-dotted) and colder (blue dashed) BBs. The geometrical angles $\chi = 36.2°$ and $\xi = 31.8°$ are chosen so that the observed $PF \simeq 1.2\%$ is reproduced and the ratio $A_2/A_1 = 6.3$ is the closest to the observed one.

This result goes beyond earlier attempts to link RX J1856.5-3754 to the Hall attractor, which could reproduce the temperature ratio, but obtaining that the *hot* region had the largest area (Popov et al., 2017). In fact, this early work considered only the imprint of the magnetic field on the surface temperature via the envelope conduction, on top of an isothermal crust. When considering the effects of the the magnetic field in the whole crust, the efficient heat trapping mechanism active in the presence of a high degree of symmetry allows small hot structures to get formed and persist over long timescales even without external heating agents.

It is finally worth remarking how this result was obtained under some assumption, dictated by the uncertainties in the estimates of some source parameters and by the limitations of the present theoretical model. In particular, the dynamical age estimate was chosen rather than the spin-down one, which not only is a worst estimator of the age, since it assumes a constant dipolar field throughout the evolution, but in this case is affected by the poor measure of $\dot{P}$. Moreover, the chosen value of the dipolar field which is compatible with that derived by Ho et al. (2007) but a factor 2–3 smaller than the spin-down measure. Given these uncertainties and the hindrance of comparing an inherently multipolar model with estimates derived assuming a dipolar field, the idea behind this choice was to use values inferred from spectral fitting to investigate the spectral properties. At any rate, several other runs with different initial field values were checked to produce qualitatively similar results and, in particular, the fact that the spectrum is always well described by a double BB with the ratio A_2/A_1 eventually getting above unity continued to hold.

Furthermore, the surface emission mechanism is probably more complicated than an isotropic blackbody and emission models from an atmosphere or a condensed surface should be employed. Furthermore, no account has been made for possible effects due to the radiation across the NS magnetosphere and the interstellar medium, as well as for the response function of a real X-ray detector, although these are likely not to alter dramatically the expected spectral shape and pulse profiles (Page and Sarmiento, 1996). Even more important, a complete model would require some information about the source geometry. The viewing angles χ and ξ are typically hard to determine in radio-quiet sources like the M7, due to the inherent degeneracy which affects spectroscopy alone. A natural way to solve this problem is to exploit additional observables, like the ones provided by polarisation measurements, which are already accessible in the optical band and will be available in the near future at X-ray energies with new generation satellites like *XPP* (Jahoda et al., 2019). Using this technique, Mignani et al. (2017) gave a constraint for the viewing geometry of RX J1856.5-3754 from observations in the optical band by comparing theoretical models and observations of the *PF* and polarisation parameters as functions of the viewing angles. These estimates, however, are based on a purely dipolar field and cannot be directly compared to the model presented in this work. A model of polarised emission taking into account a consistently evolved multipolar field may in the future provide new insights on this matter.

Another issue that arises when comparing the present model to RX J1856.5-3754 is the computation of the spin period evolution. Taking an initial period of 10–50 ms

and solving Eq. 1.3 as shown in Fig. 4.2, the final period is $\approx 1\,\mathrm{s}$. This value is quite shorter than the ones measured in the M7 of the same estimated age, $P \sim 3 - 10\,\mathrm{s}$ (RX J1856.5-3754 has $P \simeq 7\,\mathrm{s}$). Such values may be reproduced only if the initial period is of the same order of the present one (a possibility that has actually been proposed, e.g., by Haberl et al. (2012) for SXP 1062). Nevertheless, other factors may be at play: first and foremost, an underestimate of the initial field (reflecting in a too low $B_{\mathrm{dip}}(0)$), but also that spin-down losses themselves should be computed self-consistently. In fact, even though the dipole is the only radiative component in a vacuum, the presence of a magnetosphere can alter the spin-down evolution. As higher multipoles have not decayed as yet in the lower magnetosphere, a complete model, akin to the one developed by Spitkovsky (2006) for a dipolar field, should be used to assess the effects of the strong multipolar structure on the spin-down.

4.2 The rise and fall of Instabilities

After describing a case in which the initial axial symmetry is preserved throughout the evolution, this section will turn to one that, albeit starting from a symmetric initial condition, spontaneously breaks it forming an inherently 3D pattern. Such a behaviour is possible when the field is able to trigger an eMHD instability, that also causes the rapid formation of low scale structures.

An initial condition for which an unstable behaviour is expected is one where a strong toroidal field is present. Recently, Gourgouliatos and Pons (2020) studied such a case for the magnetic field evolution only, confirming that the Hall evolution can indeed trigger physical instabilities of the resistive tearing type—i.e. happening at finite electrical conductivity (Wood et al., 2014). Moreover, Igoshev et al. (2020) studied some configurations with strong toroidal fields within a coupled magnetothermal evolution framework, finding an inherently 3D behaviour (even though in those cases substantial local field enhancements were not found). It is worth noting that the idea of strong toroidal fields buried in the depths of magnetar-like objects is not new: for example, it has been invoked to explain the activity of the so-called *low-B magnetars*. These peculiar sources, among which the more well-known are SGR 0418+5729 and Swift J1822.3−1606[1], exhibit a transient activity that is virtually indistinguishable from that of other magnetars, whereas spin down measurements yield dipolar field estimates in line with those of standard radio pulsars (see e.g. Turolla et al., 2011, and references therein). Therefore, since the transient activity is the same observed as the manifestation of an ultra-strong field, this must be present in these objects as non-radiative components, like the toroidal one.

To explore one of these cases, a simulation was run with an initial dipolar poloidal field with $B_{\mathrm{dip}}(0) \approx 10^{14}\,\mathrm{G}$ and a strong $\ell = 2$ toroidal field with $B_{\mathrm{tor}}(0) \approx 4 \times 10^{15}\,\mathrm{G}$. As the signature of instabilities is to produce small scale structures, the angular resolution for this run had to be increased up to $\ell_{\max} = 250$, yielding a resolution of few tens of

[1] See the McGill magnetar catalogue, `http://www.physics.mcgill.ca/~pulsar/magnetar/main.html`, (Olausen and Kaspi, 2014).

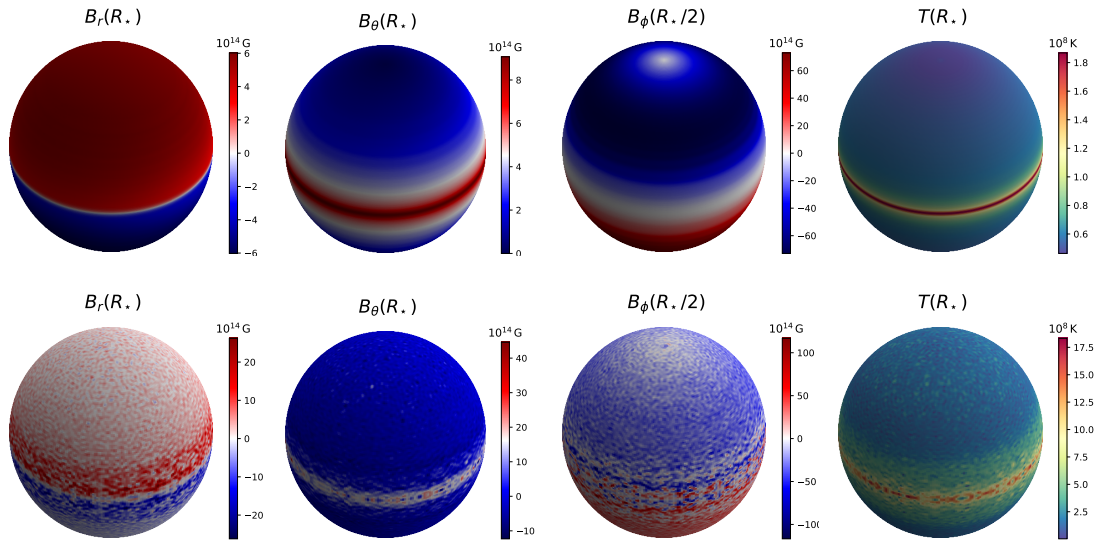

Figure 4.12: Two snapshots of the evolution of the magnetic field and temperature for an early configuration (top row, $t \simeq 300\,\mathrm{yr}$) and a later one, after the instability has been triggered (bottom row, $t \simeq 6\,\mathrm{kyr}$). The ϕ component of the field is shown at half depth, since the boundary condition suppresses it at the surface.

meters on the surface. Indeed, after a few τ_H the instability is triggered. Figs. 4.12 and 4.13 show an early configuration, $t \simeq 300\,\mathrm{yr}$, compared to a later one, $t \simeq 6\,\mathrm{kyr}$; as in the previous cases, structures form along the magnetic equator, and a general symmetry can still be discerned, but on top of those a more intricate pattern can be clearly seen. The structure of the field is very speckled, as the field is efficiently amplified in local small structures in which values $\gtrsim 2 \times 10^{16}\,\mathrm{G}$ are reached. As a consequence, the temperature itself gets asymmetric and is increased by local enhanced ohmic heating.

As already mentioned, the presence of this kind of instabilities in the Hall evolution has been assessed in the literature. Nevertheless, the physical rather than merely numerical nature of case at hand has to be checked; this can be done by inspecting the magnetic power spectrum, shown in Fig. 4.14. The fact that the resolution is good enough not to trigger artificial numerical instabilities is borne out by the flatness of the spectrum at high ℓ, sign that the energy cascade from the large scale modes has not reached the limit imposed by the simulation setup. The small rising tail at the very end of the spectrum is a common feature in spectral simulations, and caused by the aliasing procedure; since it does not reach high values and is well separated by the rest of the cascade by the plateau, it is not worrisome. As noted when discussing the Hall attractor, the evolution has a parity preference, manifesting itself in the zigzagging shape of the power spectrum. On top of this, another wavy profile of secondary peaks with a width of some tens of ℓ's can be observed, with a general decreasing trend towards the higher modes, in a cascade-like fashion following at a roughly constant slope up to $\ell \simeq 100$. From dimensional arguments,

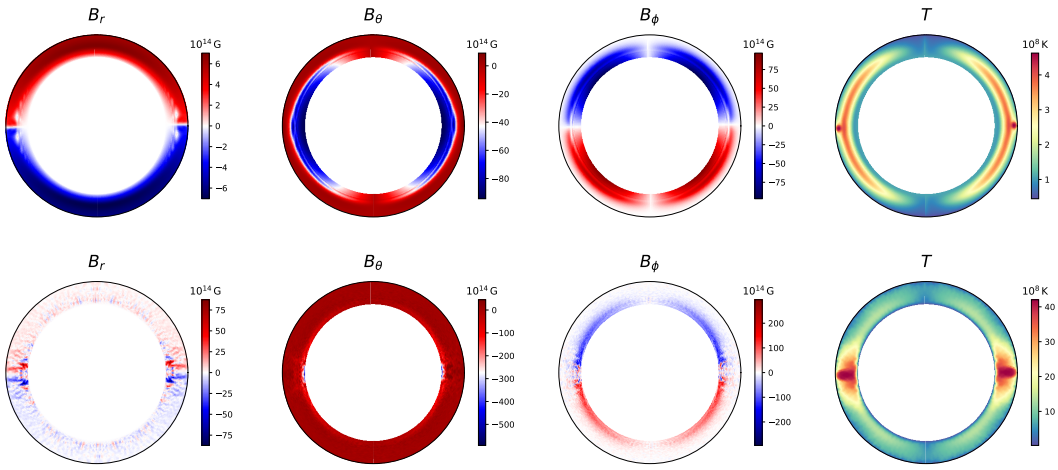

Figure 4.13: Same as Fig. 4.12 but showing the quantities on a cut along the prime meridian.

Goldreich and Reisenegger (1992) proposed for the Hall cascade a scaling as ℓ^{-2} whereas, using a more refined argument drawing from the analogy of the Hall eMHD with kinetic Alfvén waves, Schekochihin et al. (2009) give a scaling with exponent $-7/3 \simeq -2.3$. Due to the complex structure of the present spectrum, an attempt to quantitatively estimate the slope of the present case was not attempted, let alone one to distinguish between these two close values; nevertheless, the spectrum seems consistent with a ≈ -2 exponent (dashed line in Fig. 4.14). Since the system retains an high degree of axial symmetry, the power spectrum as a function of the order m is sharply peaked at 0 and shows very scant features; hence, it is not shown or discussed here. To sum up, a merely numerical nature for the observed behaviour is to be discarded, and the onset of a resistive tearing eMHD instability confirmed.

The main consequence of the onset of an instability is the formation of small regions in which the magnetic field and temperature get enhanced. These seem to be the ideal conditions to build up a strong magnetic stress that is able to "break" the crust, which as T increases becomes weaker, i.e. able to support smaller mechanical stresses without breaking or deforming. To test this, the magnetic stress tensor $M_{ij} = B_i B_j / 4\pi$ can be compared to the maximum mechanical yield of the crust through the von Mises criterion (see e.g. Perna and Pons, 2011; Pons and Rea, 2012; Lander and Gourgouliatos, 2019),

$$\sqrt{\bar{M}_{ij}\bar{M}^{ij}} \gtrsim \tau_{\max}(n, T) \tag{4.4}$$

where $\bar{M}_{ij}$ denotes the traceless part of the stress tensor. Estimates for $\tau_{\max}$ where derived by Chugunov and Horowitz (2010) from molecular dynamic simulations and elucidated the strong dependence of the breaking stress on temperature. In particular,

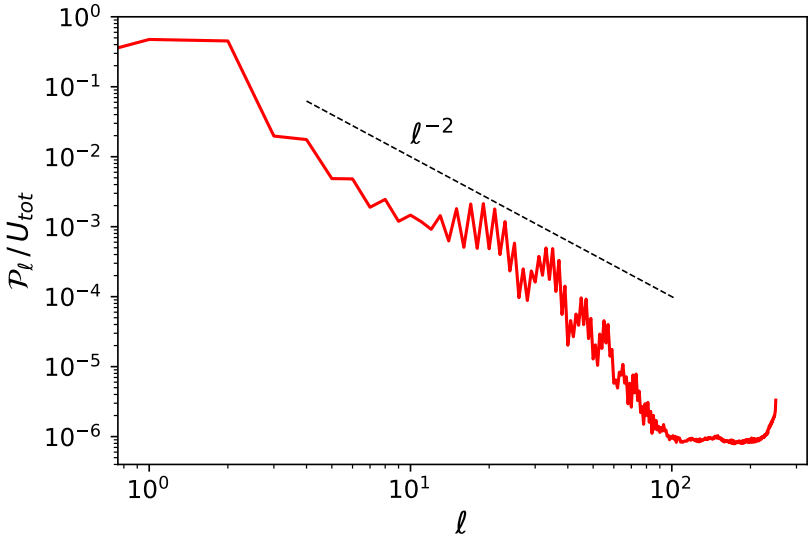

Figure 4.14: Magnetic power spectrum at $t \simeq 6\,\mathrm{kyr}$, after the instability has been triggered. The dashed line with slope ℓ^{-2} represents the slope obtained from scaling relations for Hall turbulence by Goldreich and Reisenegger (1992).

they provide a fit for the maximum crustal yield in the form

$$\tau_{\max} = \left(0.0195 - \frac{1.27}{\Gamma - 71}\right) n_i \frac{Z^2 \mathrm{e}^2}{a} \tag{4.5}$$

where $\Gamma = Z^2\mathrm{e}^2/ak_BT$ is the classical Coulomb coupling parameter, n_i is the ion density, $a = (4\pi n_i/3)^{-1/3}$ is the ion sphere radius and the mean ion charge in the Fe-Ni crust was taken to be $Z = 29.4$ as used in Horowitz et al. (2007) in a similar context. Since $\tau_{\max}$ decreases at higher T, a consistent coupled evolution of temperature and magnetic field is essential for evaluating the possibility of the criterion to be satisfied.

For the present case at $t \simeq 6\,\mathrm{kyr} \lesssim \tau_H$, Fig. 4.15 shows the ratio between the magnetic and the breaking stress in the region of the crust where the ratio itself is maximum, which happens to be at about half the crust depth. This ratio indeed reaches values up to $\sim 50\%$: the von Mises criterion for crustal yielding is then likely to be fulfilled. This happens in the equatorial region, where the strongest field is developed in a heated, weaker region.

It ought to be note, nevertheless, that the use of the von Mises criterion as expressed by equation (4.4), albeit widespread in the literature, should be taken with some care. In fact, it does not take into account the effects of the enormous gravity, that tends to inhibit any radial displacement (see e.g. Haskell, 2008). However, since the resistive tearing instability arises as a consequence of the presence of a strong toroidal field, the present result is not much affected even when setting to zero all radial shear terms (the maximum

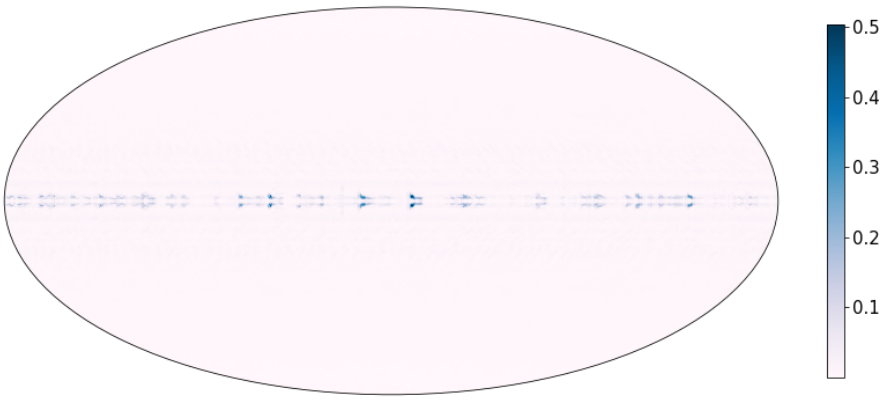

Figure 4.15: Ratio between magnetic stresses and maximum yield during the instability, shown in Mollweide projection at the radius where the maximum value is attained, close to half of the crust depth.

stress-to-yield ratio only decreases from $\sim 50\%$ to 45%). Still, only a consistent, non-local calculation which takes into account the global hydrostatic structure of the crust could unambiguously solve the issue.

Moreover, the physical process happening once the von Mises criterion is fulfilled is not known in detail: in the literature, the expression *starquake* is often used (e.g. Pons and Rea, 2012), yet it is somewhat prone to give rise to misunderstandings. In fact, under the extreme pressure of a NS crust, the creation of fractures and the ensuing gaps are not possible (Jones, 2003); rather, the crust starts flowing plastically (see again Lander and Gourgouliatos, 2019). This directly concerns magnetar activity, since the flowing matter has field lines locked in, resulting in a rearrangement of the field which is thought to be responsible for magnetar bursts and outbursts (Pons and Rea, 2012). However, the full solution of the problem would require again the inclusion of the hydrostatic and hydrodynamic evolution of the crust, which is beyond the scope of this work. The instability was observed to last for some 1000 yr before being damped by dissipation, but for the aforementioned reasons following it any further would not be representative of magnetar evolution.

At any rate, the onset of an eMHD instability as observed here is a mechanism that is able to provide a viable explanation for the activity (bursts and outbursts) detected in young magnetars (age $\lesssim 10^4$ yr), which are the vast majority of the magnetar population. Whether the same instability can be triggered for different parameters that better represent the conditions typical of older objects, like the low-B sources SGR 0418+5729 and Swift J1822.3-1606 (age $\approx 10^5$–10^6 yr; Turolla et al., 2011; Rea et al., 2012) or the onset of outbursts is produced by a different, possibly related, mechanism remains an open question.

Θ_q	β	$PF_{\max}$
45°	0.75	16%
45°	1.25	20%
45°	10	23%
90°	1	4%

Table 4.1: Parameters of the configurations discussed in Sec. 4.3, with the maximum value of the *PF* reached in the evolution.

4.3 Non-axisymmetric initial conditions

As a further step, this section will deal with cases which do not have any degree of symmetry from the very initial condition[2]. As discussed in Sec. 4.1, symmetric field configurations produce a thermal emission with low pulsed fraction and symmetric lightcurves. While considering locally anisotropic emission mechanisms, going beyond the BB used in this work, may alter these properties, the wide variety of observed *PF*s and lightcurve shapes calls for the consideration of more complicated field topologies. Geppert et al. (2006); Zane and Turolla (2006); Page et al. (2007) tested different possibilities, although only focusing on the structure of the B-field in the crust (presence of a toroidal component or higher order multipoles) without addressing its evolution, nor its effects on the temperature of the crust. More recently, Perna et al. (2013) presented surface emission models which were derived self-consistently following the star magnetothermal evolution in 2D (axial symmetry).

No attempt to explore the infinite parameter space of all the possible initial field topologies will be done here; rather, a small number of representative cases will be presented, in the spirit of understanding the analogies and differences brought by an essentially 3D treatment. Namely, on top of a dipolar poloidal field with $B_{\rm dip}(0) = 10^{13}\,\mathrm{G}$ akin to the one presented in Sec. 4.1 a quadrupolar poloidal component with an axis rotated by an angle Θ_q has been added. Several values of Θ_q and of the relative strength $\beta = B_{\rm quad}(0)/B_{\rm dip}(0)$ were studied as reported in Tab. 4.1; in all cases the initial temperature was set to a uniform value $T(0) \equiv 10^8\,\mathrm{K}$. Similar configurations have recently been studied by Kondratyev et al. (2020) as a background for a detailed stationary-state model of heat transport in the envelope which, although not directly comparable to the results of an evolutionary code considering the crust, will serve as a qualitative benchmark.

In general, the evolution shows that there is still a transfer of energy to higher magnetic multipoles, with the initial components remaining dominant, and odd modes are still being favoured. The tilt angle Θ_q undergoes virtually no change ($\lesssim 1°$) over the whole time span for all the examined cases. On the other hand, the temperature evolution within the crust shows a different behaviour with respect to the axisymmetric

[2]Part of the results presented in this section were obtained in collaboration with Andrea Gnarini for the completion of his MSc Thesis, `http://tesi.cab.unipd.it/65186/`.

cases. In fact, whereas currents still tend to heat up the region near the equator (of the dipolar component), the presence of a non negligible off-axis quadrupolar component makes so that field lines are more tangled. These field lines are able to bring heat outside the closed field lines in the hot region, so that the heat trapping mechanism is not as efficient. For this reason, the hot region quickly disappears, and the crust goes back to being almost isothermal over some τ_H.

Consider the first two cases in Tab. 4.1 ($\Theta_q = 45°$, $\beta \approx 1$); their temperature evolution is shown in panel (a) of Figs. 4.17 and 4.18. Along the equator of the dipole (note that the coordinates of the projection are referred to the axis of the quadrupole) a hotter belt is formed, but it is not symmetric. Rather, it gets thinner at one end and much larger at the other, so that effectively a spot-like structure appears in one hemisphere only. Going from the crust to the surface, including the blanketing envelope, the resulting thermal map is still dominated by magnetic effects, and the colder equatorial ring appears; however, the presence of the quadrupole stretches it, more noticeably for the higher β case, to a more sharp-cornered shape. Moreover, a somewhat higher temperature region is present above of the hot patch. Note, again, that the most efficient heat dissipation and retention happens in the regions where the field lines are more closed (i.e. at the equator of the dipole), but this same condition also translates in a more efficient magnetic blanketing in the envelope, as the field runs almost parallel to the surface, so that the hottest point in the crust actually corresponds to the coldest zone on the surface. As the evolution proceeds, however, the crust becomes almost isothermal, and by some tens of kyr the cold belt is the only feature left on the surface. Notice that its shape changed from the initial state as a consequence of the magnetic field evolution.

The thermal maps obtained for these cases can again be studied in terms of observables using the GR ray-tracing code. Figs. 4.17 and 4.18, (b) panels, show the time evolution of the *PF* for selected geometries, as well as the dependence of the *PF* from the angles χ between the LOS and rotation axis and ψ between the spin axis of the one of the *quadrupolar* component (which was used instead of ξ just for coding convenience) at selected times. Compared to the symmetric case, the *PF* can reach much higher values, peaking at early times ($t \lesssim 10\,\mathrm{kyr}$) to then start decaying very slowly. The peak corresponds to the time in which the thermal anisotropy in the crust is maximal; then, the *PF* decreases much more slowly as its evolution becomes dictated by the field evolution on an isothermal crust. This can be understood as the effect of ohmic dissipation, which tends to bring the field to a dipolar state on very long timescales ($t \gtrsim 10^7\,\mathrm{yr}$) which are not followed here.

An asymmetric configuration also produces more varied shapes of the pulse profiles: as an example, Fig. 4.16 shows them for the model with $\Theta_q = 45°$, $\beta = 1.25$ at an age of $\sim 10\,\mathrm{kyr}$. For certain viewing geometries, the shape deviates significantly from a quasi-sinusoidal one.

In the two cases discussed so far, the *PF* evolution is quite similar, but the one with the larger β yields a higher *PF*. It may then be expected that as the quadrupole increases so does the *PF*, and very high values can be reached in this way. To test this, a somewhat extreme case with $\beta = 10$ was run. However its evolution, displayed in Fig. 4.19, does not

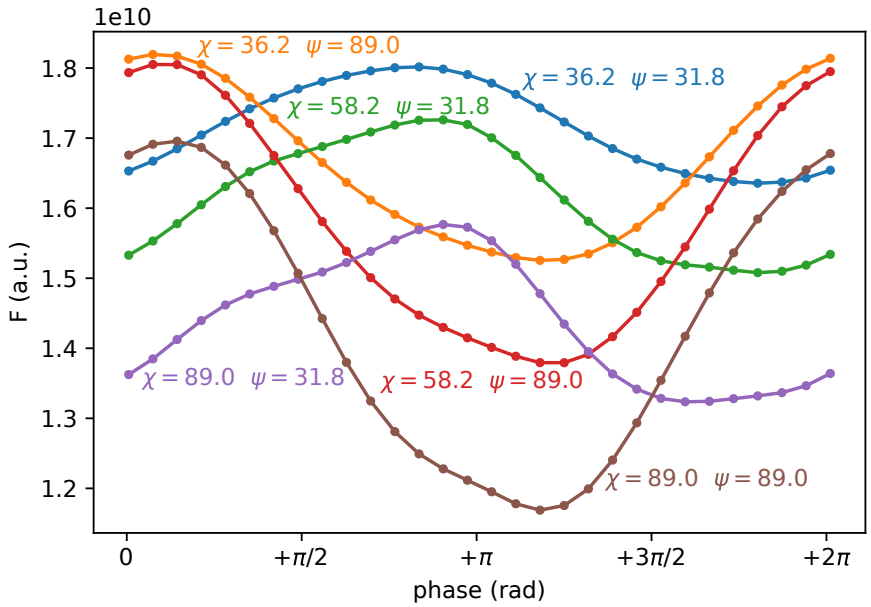

Figure 4.16: Same as Fig. 4.6 for the asymmetric case $\Theta_q = 45°$, $\beta = 1.25$ at time $t = 9570\,\mathrm{yr}$.

follow this pattern, and it is closer to the one of a symmetric quadrupole. The role played by the equator of the dipole in the case from Sec. 4.1 is now taken over by the two nodes of the quadrupole, and a two band structure appears on the surface (hot inside the crust, but cold on the envelope surface). Moreover, an efficient heat trapping mechanism is recovered. This results in longer evolution timescales; in particular, the crust reaches an isothermal state after a time that is longer by almost an order of magnitude with respect to the previous cases. As to the *PF*, the maximum value only marginally increases with respect to the one obtained for $\beta = 1.25$, whereas the evolution for a fixed geometry spans a much wider range, eventually going below 10% for all angles.

Finally, cases with different Θ_q was tested. Values of 30° and 60° have been run, without significant qualitative differences to those at 45°. It is however worth briefly discussing the value $\Theta_q = 90°$, that was taken with $\beta = 1$ (see Fig. 4.20). This case is still somewhat symmetric, resulting in quite low *PF* values ($\lesssim 4\%$), comparable to the purely symmetric cases. Even if the field has now mostly ϕ component, a quadrupolar poloidal field has not the same geometry of a toroidal field (which in axial symmetry has ϕ component *only*), and its effect is again to isothermalize the crust, which in this case happens on a timescale $\approx 100\,\mathrm{kyr}$, corresponding to the plateau of the *PF* profile.

In conclusion, even keeping an isotropic emission mechanism non-symmetric models provide a way to account for significant *PF* values, up to about 25%, while exhibiting a rich behaviour in the pulse profile shape, that can become asymmetric and skewed as is indeed observed in some sources (e.g. the XINS RX J0420.0-5022 Haberl et al. 2004).

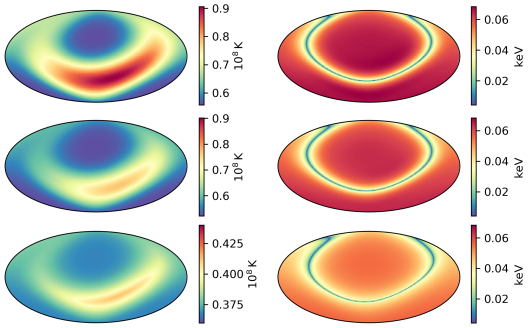

(a) Mollweide projection of the thermal maps at the top of the crust (left) and at the surface (right).

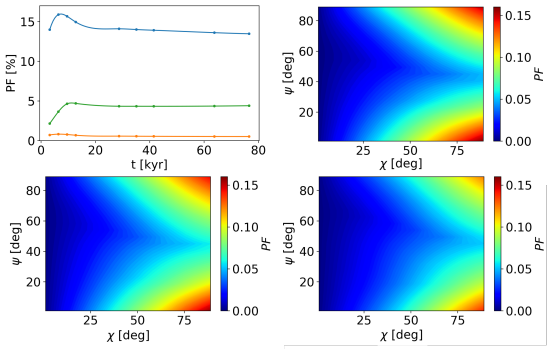

(b) Evolution of the PF for selected viewing angles, alongside its full dependence on ξ and ψ at selected times.

Figure 4.17: Thermal maps and pulsed fractions for the case $\beta = 0.75$, $\Theta_q = 45°$, shown at three times $t_1 = 6378\,\mathrm{yr}$, $t_2 = 9570\,\mathrm{yr}$ and $t_3 = 41\,476\,\mathrm{yr}$ (top to bottom, left to right). The PF evolution curves correspond to the viewing geometries with angles $\chi = 90°$, $\psi = 0°$ (blue, corresponding to the maximum overall value), $\chi = 65°$, $\psi = 45°$ (green) and $\chi = 45°$, $\psi = 45°$ (orange).

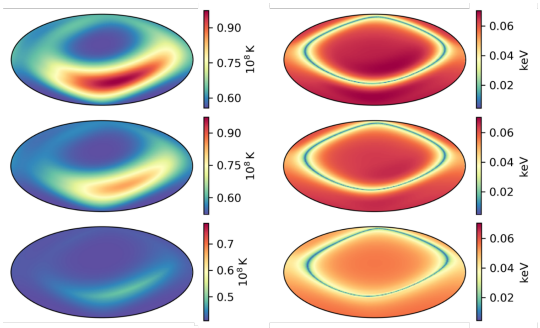

(a)

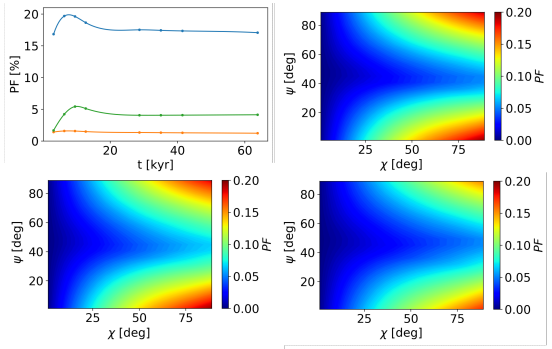

(b)

Figure 4.18: Same as in Fig. 4.17 for the case $\beta = 1.25$, $\Theta_q = 45°$, shown at three times $t_1 = 6378\,\mathrm{yr}$, $t_2 = 9570\,\mathrm{yr}$ and $t_3 = 41\,476\,\mathrm{yr}$.

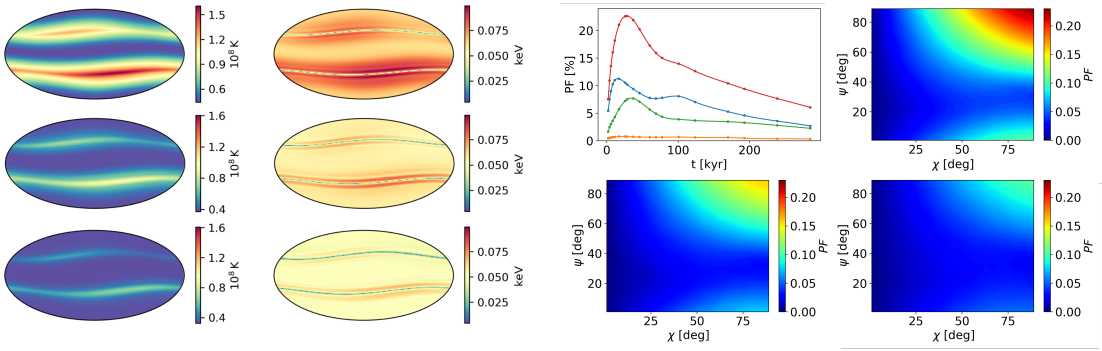

(a) (b)

Figure 4.19: Same as in Fig. 4.17 for the case $\beta = 10$, $\Theta_q = 45°$, shown at three times $t_1 = 25\,637$ yr, $t_2 = 68\,900$ yr and $t_3 = 169\,700$ yr (note that the timescale is quite different from the one of Figs. 4.17 and 4.18). In this case, the maximum PF corresponds to the viewing angles $\chi = 90°$, $\psi = 90°$ (red evolution curve).

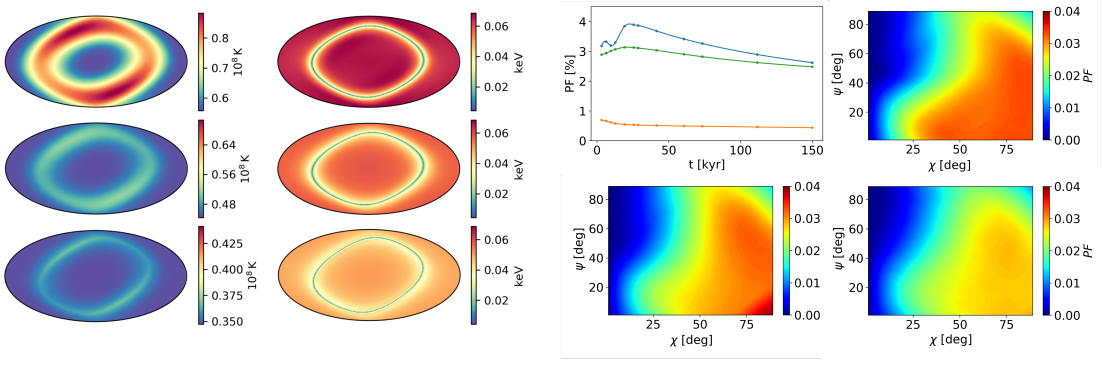

(a) (b)

Figure 4.20: Same as in Fig. 4.17 for the case $\beta = 1$, $\Theta_q = 90°$, shown at three times $t_1 = 6378$ yr, $t_2 = 68\,900$ yr and $t_3 = 115\,500$ yr (note that the timescale is quite different from the one of Figs. 4.17 and 4.18).)

A remarkable effect of the field complexity is to make so that in these cases the crust tends to become isothermal rather quickly, so that the late-time observed properties are controlled by the structure of the magnetic field only. The absence of efficient heat retention also prevents mechanisms such that invoked in Sec. 4.1.1 to explain the peculiar spectrum of RX J1856.5-3754: even in an unfavourable geometry giving a small *PF* the area of the hotter emitting area would be larger than the cold one. Finally, it is worth noting how, albeit being based on a simplified envelope model, the thermal maps obtained for the asymmetric fields are in good general agreement with those produced by the detailed model of Kondratyev et al. (2020) for similar geometries.

4.4 A Highly Multipolar Example

In the previous sections, cases with quite simple initial conditions were presented. As already stressed, the foremost reason for this choice remains the poor understanding of the early PNS phases and the consequent absence of a robust alternative. Even though solving this issue is far beyond the scope of this work, this section will present a representative example mimicking a more intricate initial condition as a proof of concept for the capabilities of the code.

In order to run such a test case, the work by Reboul-Salze et al. (2021) was taken as a reference. Using the code `MagIC`[3], they developed a model of field amplification based on the mechanism of magneto-rotational instability (MRI) in a PNS. Their code shares the basic approach (as well as some history) with `PARODY`, so that their results can be quite naturally put into the present framework. In particular, they show the power spectra for the magnetic field after the MRI has fully developed, for both the poloidal and toroidal parts. This state corresponds to roughly the first seconds the PNS state, which is quite different from the one in which the Hall evolution begins. Nevertheless, in the aforementioned spirit a condition taken from their result has been adapted here, under the assumption that the initial field maintains the same multipolarity (i.e. power spectrum shape).

To this end, the generic mode of the initial field was built as

$$B_{\ell m}(r) = \frac{1}{\sqrt{\mathcal{P}_{\ell m}}}\, W(r)\, \cos\left(\frac{2\pi}{\lambda_r}(r - r_c) + \phi_{\ell m}\right) e^{\mathrm{i}\,\psi_{\ell m}}; \qquad \lambda_r = \sqrt{\frac{r^2}{\ell(\ell+1)}} \tag{4.6}$$

where λ_r is the typical radial wavelength associated to each mode, $W(r)$ is a weight function that ensures that each component matches the BCs of the model smoothly, and ϕ, ψ are pseudo-random phases. The desired power spectrum is recovered by modulating each mode with the value $\mathcal{P}_{\ell m}$, which was in turn obtained from a simple fit of the two components of the magnetic power spectrum given in Fig. 7 of Reboul-Salze et al. (2021). The overall field was then scaled in order to obtain a maximum field of $\approx 4 \times 10^{14}$ G; note, however, that this implies a dipolar field smaller by several orders of magnitude, $\approx 10^{11}$ G. The initial temperature has been set to a constant value.

[3] `https://magic-sph.github.io/index.html`.

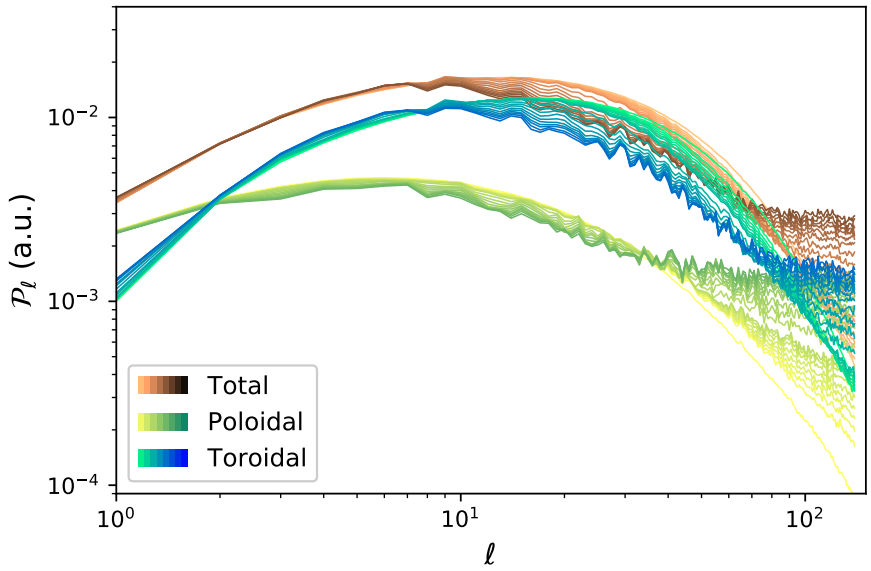

Figure 4.21: Time evolution of the magnetic power spectrum for the first 7 kyr of the initial conditions of Fig. 4.22. The different spectra are shown at constant time intervals, and darker colours correspond to more evolved configurations.

This initial configuration, shown in Fig. 4.22, was then evolved for ≈ 7 kyr. In Fig. 4.21, the evolution of the magnetic power spectrum throughout this period is shown. As in the case of an initial dipolar field, the Hall evolution favours some modes over the nearby ones, producing its hallmark wavy pattern; the peak of the spectrum is displaced from $\ell \simeq 20$ to $\ell \simeq 10$, while a lot of energy is transferred to the small scales, with the spectrum getting close to a plateau at large ℓ. Remarkably, the energy content in the dipole (which determines the magneto-rotational properties) hardly changes, with the value of the dipole at the surface evolving quite erratically without exhibiting variations of more than $\approx 20\%$. Hence, even though the energy transfer between different scales is indeed happening, the Hall evolution does not seem to be able to account for the formation of large scale magnetar-like fields. At the same time, rescaling the whole field in order to have the desired initial power spectrum shape with a large dipole would produce gargantuan total fields, which do not match the observational evidence. Therefore, some other mechanism modifying the early field structure has to be invoked to explain the large observed dipolar fields; at the same time, the lack or inefficiency or inefficiency of said mechanism may account for the formation of low-dipolar field objects like CCOs and, more specifically for this framework, low-B magnetars.

In the phyisical space, the evolution leads to the configuration shown in Fig. 4.23. The magnetic field tends to get concentrated in medium-scale structures, where it gets enhanced; these, in turn, translate into the formation of hotter regions in the uppermost layers, appearing as hot spots on the surface (see the cuts in Fig. 4.24). Moreover, these

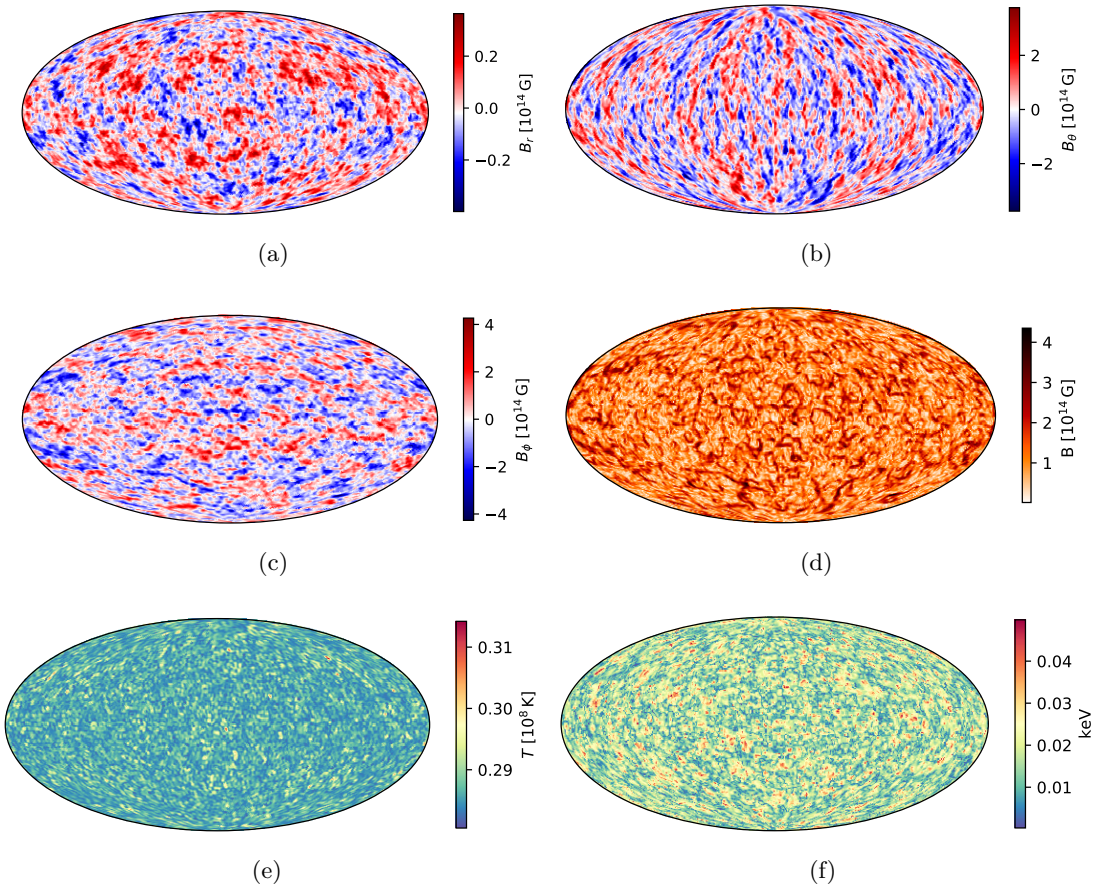

Figure 4.22: Magnetic field components (panels a–c), total value (panel d), temperature distributions (panel e) at the crust top, and surface temperature map (panel f) for the highly multipolar field of Sec. 4.4 after few iterations from the initail condition.

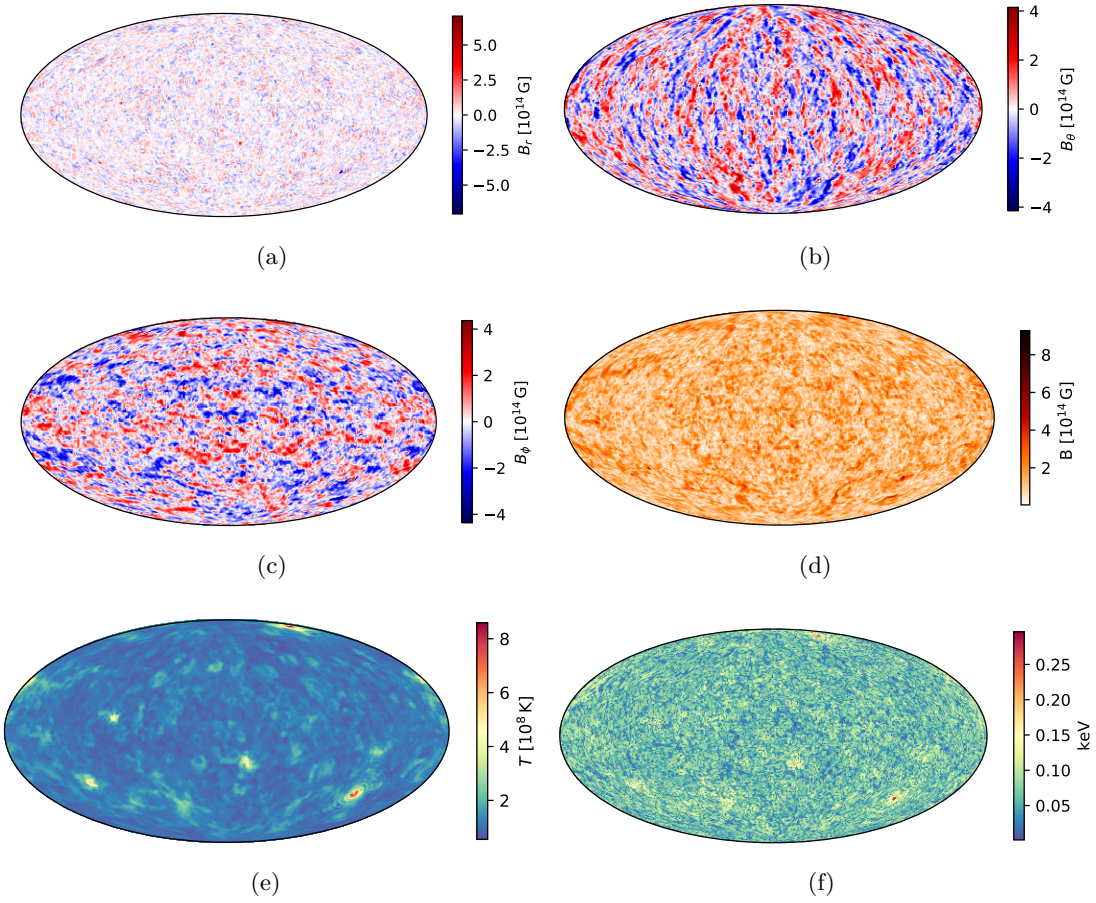

Figure 4.23: Same as Fig. 4.22 after $t \approx 7\,\mathrm{kyr}$.

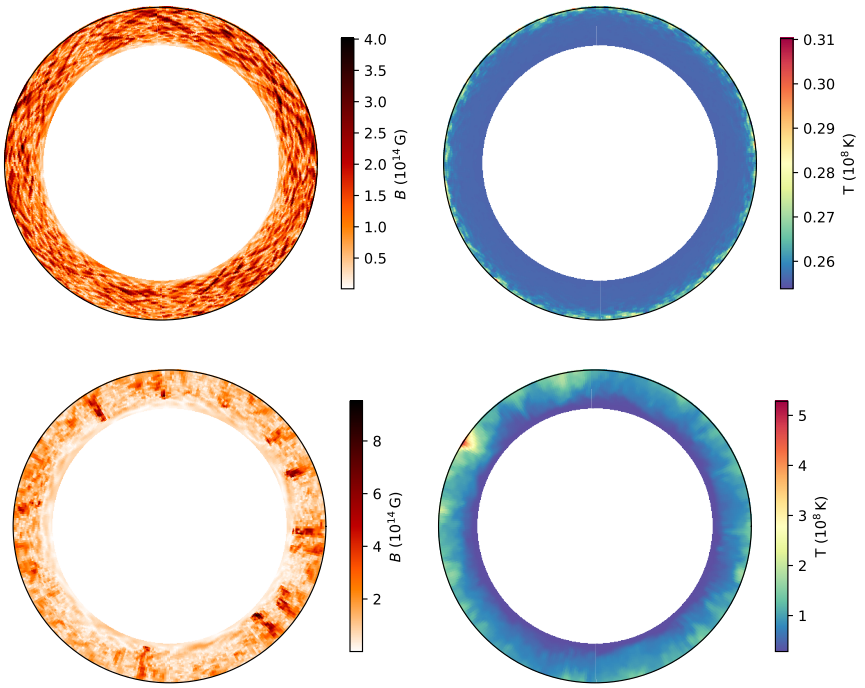

Figure 4.24: Cuts along the prime meridian for the magnetic field strength and temperature from Fig. 4.22 (top row) and Fig. 4.23 (bottom row).

structures evolve on sub-Hall scales (or, better, on the Hall timescales adapted to the small scale structure), with the thermal map of the star changing on timescales of the century (see Fig. 4.25). This variability prevents robust predictions on the expected pulsed fraction and lightcurve shape, for which a systematic study beyond the scope of this work would be required.

Finally, it is worth mentioning that Gourgouliatos et al. (2020); Igoshev et al. (2021) studied a field that went on to form a continuous spectrum akin to the one used here, finding the same formation of spotlike structures. However, their initial condition had energy injected in some high modes only, with the subsequent evolution pointing towards a single structure. Conversely, starting the simulation with an already fully spread energy spectrum produces a higher degree of structure variability in time within a comparable timescale.

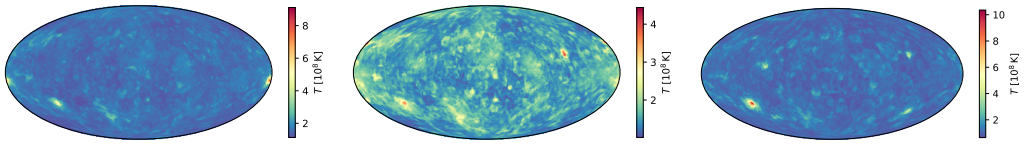

(a) $t \simeq 1200\,\mathrm{yr}$ (b) $t \simeq 2000\,\mathrm{yr}$ (c) $t \simeq 5300\,\mathrm{yr}$

Figure 4.25: Thermal maps at intermediate times (see also with Fig. 4.22 and Fig. 4.23, panels (e)). The structure of the hot patches changes with a timescale of several centuries.

CHAPTER 5

Localised Heating in the Crust

Studying the long-term global evolution of a NS is one of the main applications of magnetothermal evolution models, but it is perhaps not the context in which a 3D approach shows all its capabilities. In fact, numerical hindrances force some strong simplifying assumptions, which becomes a price one can pay in those cases in which the possibility of removing any symmetry assumption is absolute key. This is the case when tackling certain NS behaviour, in particular that associated with short-term, transient phenomena like magnetar outbursts. This chapter will be devoted to the modelling of such phenomena as events of localised heat injection in the crust. In the first section, some results obtained with the original `PARODY` code as previously described will be presented, addressing heating in the deep crust and in the more shallow layers. They will indicate some general behaviours, but will also pose some problems concerning timescales, which will be tackled in the following section, where an updated version of the code will be presented, which will allow to study more accurate models of magnetar outbursts. The results presented in Sec. 5.1 have been published in De Grandis et al. (2020), whereas those in Sec. 5.2 are being published in De Grandis et al. (2022).

5.1 Preliminary Cases

Let us first consider the numerical setup as it has been used so far, with the only addition of a heating term that can be activated in a certain region of the crust for a given amount of time. This is tantamount to the add to Eq. 2.26 a term of the form

$$s(r, \theta, \phi)\, \dot{H}' \tag{5.1}$$

representing an additional heat source per unit time and volume. From a numerical point of view, this term is to be treated much in the same way as neutrino losses, but with an opposite sign. In order to avoid sharp spatial gradients, a smoothing function $s(r, \theta, \phi)$ has been introduced. This has to be considered when calculating the energy injection rate $\dot{H} = \int_\omega s(r, \theta, \phi) \dot{H}' \, \mathrm{d}V$ where ω represents the region in which the term is active. In the following, different choices for the precise shape of s will be made, but it will always

be taken with a maximum at the centre of the patch. The total heat injection is then computed as $H = \dot{H}\,\Delta t$ for an injection time Δt; while it would certainly be possible to introduce a function that smooths the heat injection profile in time, this has been observed to make no difference in the considered cases. Two situations will be addressed in this section: localised fast heat deposition in the deep crustal layers, and prolonged heating in the external layers.

5.1.1 Heating in the deep crust

As already mentioned, the activity of transient magnetars is believed to be due to some kind of crustal failures (see Sec. 4.2), which causes a fast dissipation of magnetic energy in a comparatively small region. The dynamics of such events is little understood, owing to the many processes that may be involved (e.g. the crust may flow plastically, Lander, 2016). Studying the details of these events is currently beyond the capability of the code, which does not incorporate a description of the crustal matter motion. However, observations point to a rather fast mechanism, whichever its origin. Therefore, a minimal model to study the effects of crustal failures, and in particular the way in which heat is transported to the surface, is to inject heat for a short time interval in a localised region of the crust, much in the same way as in Pons and Rea (2012) but in a fully 3D approach.

For the first test, a background state with an initial field $B_{\rm pol} \approx 10^{12}\,\mathrm{G}$ and $B_{\rm tor} \approx 10^{13}\,\mathrm{G}$ that has been consistently evolved for a Hall time has been considered. The rather strong toroidal field was selected in the light of the results from Sec. 4.2, where it triggered the instability ultimately causing the crustal failures.

Heat has then been injected in the innermost half of the crust, in a patch in the northern hemisphere; the function $s(r, \theta, \phi)$ considered in this case is a gaussian profile along each spatial dimension, with $\sigma_r \simeq 100\,\mathrm{m}$, $\sigma_\theta \simeq \sigma_\phi \simeq \pi/5\,\mathrm{rad}$. The magnitude of the heating is $\dot{H} \simeq 5 \times 10^{37}\,\mathrm{erg\,s^{-1}}$ (although this value is biased by the oversimplified model of the specific heat, see the discussion in Sec. 5.2). The heating term is switched on for a very short time, $\Delta t_{\rm inj} \simeq 3\,\mathrm{s}$.

The subsequent evolution of the NS luminosity as the heat reaches the surface has then been calculated assuming a patch-wise blackbody emission at the local surface temperature as derived via Eq. 2.12. Fig. 5.1 shows the resulting lightcurve; the time evolution resembles a typical FRED (fast-raise-exponential-decay) pattern. Moreover, the two curves displayed there illustrate the role played by neutrino emission in the crust. In fact, this heat deposition results in temperature high enough to trigger a sizeable neutrino emission (contrary to what occurred for the background state), which reduces the maximum photon luminosity by a factor ~ 2 with respect to the case in which neutrino losses were turned off. In the present case the peak luminosity is $\sim 10^{33}\,\mathrm{erg\,s^{-1}}$, with an increase of a factor ≈ 10 above the quiescent level.

The enhanced luminosity is not coming from the whole surface, but from a spot-like region that exhibits a somehow peculiar evolution. In fact, its shape is determined by heat diffusion, which in turns depends on the magnetic field direction as heat tends to flow along field lines. Fig. 5.2 shows some meridional cuts of the crust during the luminosity rise time, which display how heat is not just flowing radially towards the surface, but

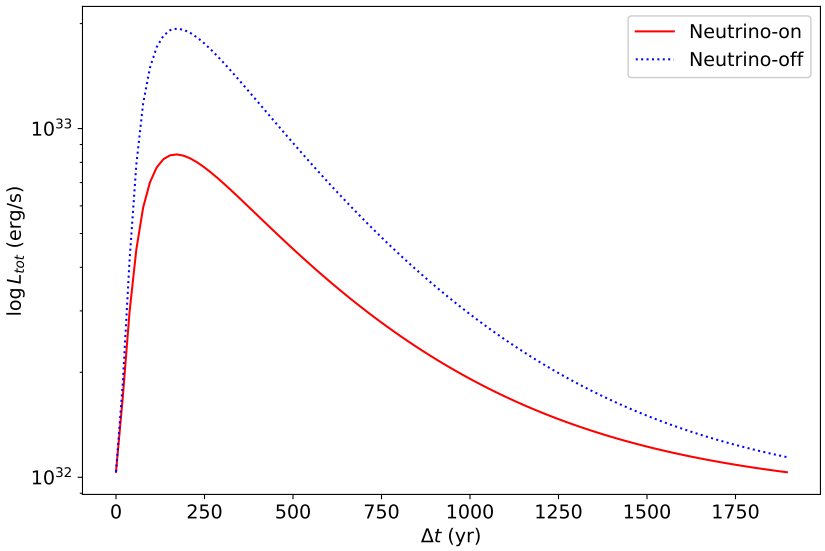

Figure 5.1: Luminosity evolution after an impulsive heat injection in the innermost half of the crust. Neutrino emission reduces the peak luminosity by a factor ~ 2.3 compared to photon cooling only.

does so following the magnetic field. Therefore, even though the maximum heat injection occurs at the centre of the patch, the patch has an asymmetric temperature, slightly hotter towards the pole. Moreover, the so formed hotter region tends to drift as it cools down, both in latitude towards the equator, and in longitude. This effect is shown in Fig. 5.3 through four snapshots of the heated surface spot at different times.

The total duration of the event, before the quiescent luminosity is reached again, is of some thousands years, with a rise time of about one century. Therefore, even though on a general level its behaviour is reminiscent of the flux variation observed during magnetar outbursts, the timescales are much longer (Coti Zelati et al., 2018). This issue will be addressed in the following section.

5.1.2 Heating from above

Another application of the framework discussed in the previous section is the study of pulsar hot spots. In fact, as long as it can be assumed that no other effects apart from heating come into play, and irrespective of the origin of the heat itself, the physical ingredients are the same. The major difference with respect to what presented in the previous section is that now energy is deposited in the outermost crustal layers, as it is the case e.g. for the heating from backflowing currents on the surface of radio-pulsars.

The background state chosen for this case is a NS with initial field $B_{\rm pol} \approx B_{\rm tor} \simeq 10^{12}\,$G and uniform temperature $T \simeq 5 \times 10^7\,$K, which was beforehand evolved for some Hall times, $t \simeq 10^5\,$yr. A heating term has then been activated in a small region of radius $\sim 0.5\,$km in the close proximity of the magnetic pole. The choice of this spot position has

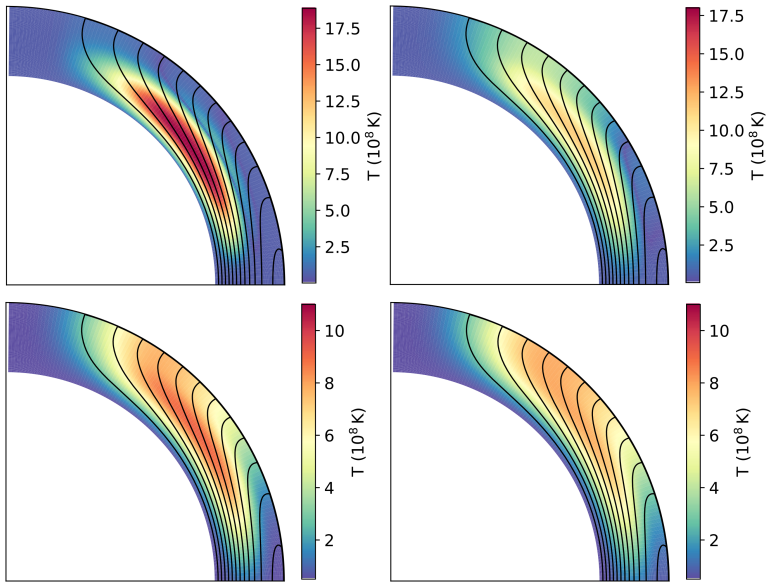

Figure 5.2: Meridional cuts (at the same ϕ) of the evolution of the hot spot during the rise phase. Time increases from left to right and from top to bottom. Transport of heat to the surface happens preferentially along magnetic field lines, whose planar projection is superimposed in black. Note that colour bar range shrinks between the two rows to improve visualisation.

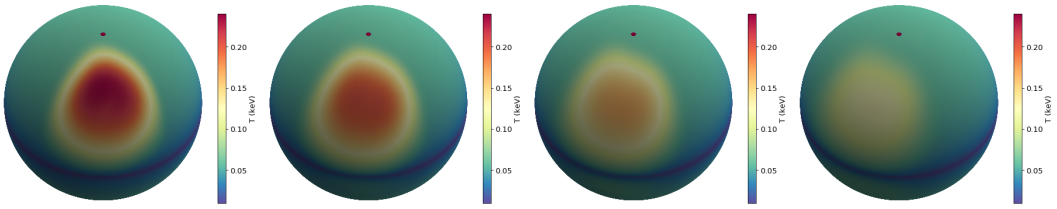

Figure 5.3: Surface thermal evolution of the hot spot producing the luminosity shown in Fig. 5.1. Time increases from left to right; snapshots are separated by $\sim 200\,\mathrm{yr}$ and the first one corresponds to the peak of the luminosity curve. The magnetic north pole is highlighted for reference.

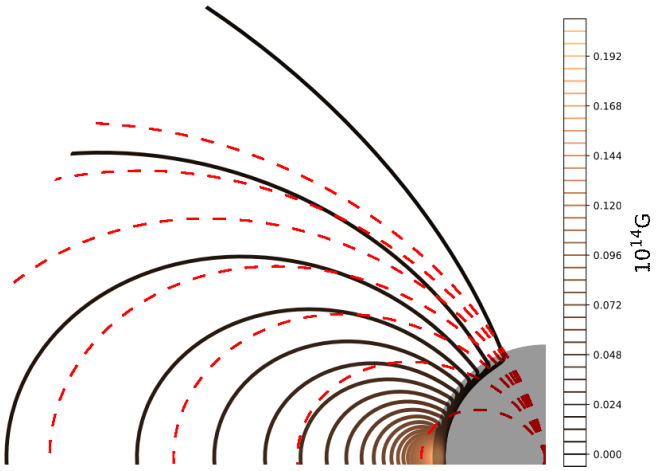

Figure 5.4: Extrapolation of the structure of the magnetic field lines outside the NS. The colour bar encodes the field strength from black (zero) to copper (maximum value). Dashed red lines indicate a purely dipolar field for comparison. Given the high degree of symmetry of this case, only a quarter of the star is shown without loss of information.

been dictated by the fact that, even though the external magnetic field in our simulations is not a pure dipole, it keeps its symmetry and has a qualitatively similar shape (see Fig. 5.4), so that heating of the polar regions is to be expected. Even if the simulations do not include the dynamics of the magnetosphere, its configuration was obtained by continuation of the boundary condition 3.36 for the magnetic field at the top of the crust, requiring that for each harmonic $B_\ell^m(r > R_\star) = B_\ell^m(R_\star)/r^{\ell+1}$.

Pulsar backflowing currents can reach a depth ranging from about a tenth to the entire width of the crust (Karageorgopoulos et al., 2019). In the simulations presented here, the heat source was activated from the surface down to a quarter of the crust width. At any rate, different depth values were verified to provide quite similar results, possibly because this length is anyway much smaller than the other relevant lengths in the problem. In these cases, the heating rate is quite modest, so that sharp gradients are not introduced; therefore, it was not necessary to introduce the modulation function s.

Provided that the heat injection is steady, the results show that the hot spot reaches a quasi-stationary state in a few years. With a heated patch of size $\sim 1\,\mathrm{km}$ and no spatial modulations, heat diffuses out so that the spot tends to assume a quasi-circular shape, staying into the injection region. Fig. 5.5 (top row), shows the initial injection shape compared to the equilibrium configuration of the hot spot obtained for a steady heat injection $\dot{H} = 5 \times 10^{25}\,\mathrm{erg\,s^{-1}}$. Then, the evolution of the same spot was followed after the heating term is turned off. In a time $\approx 1000\,\mathrm{yr}$, the spot cools down in such a way that only a ring corresponding to the region rim is left. In the final cooling phases (Fig. 5.5, bottom row), a crescent-like structure drifting towards the equator becomes visible as a subdominant feature alongside the main hot spot, which is still in correspondence to

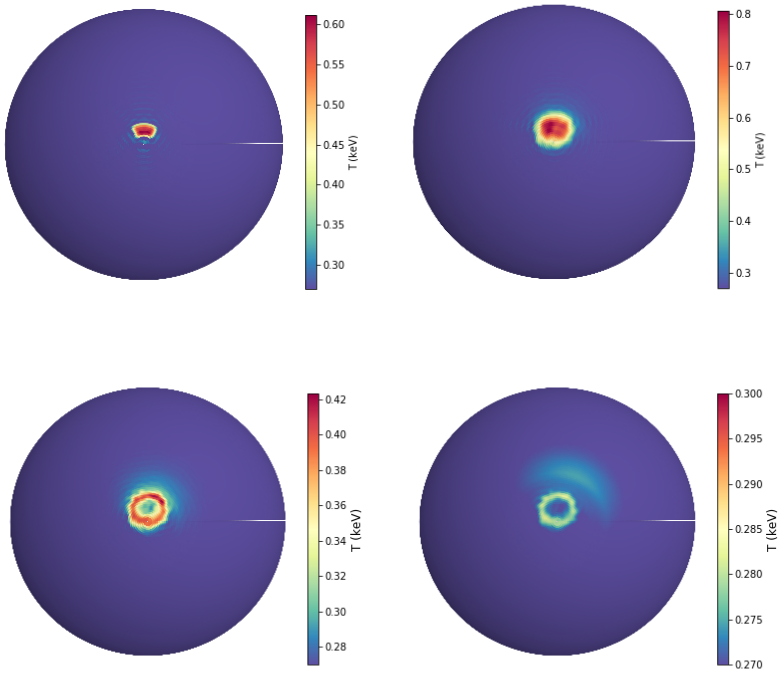

Figure 5.5: *Top row:* initial (left) and equilibrium (right) stages of the evolution of a hot region (magnetic pole at the centre, towards the observer) during a steady heat injection in the outermost layers. *Bottom row:* cooling of the spot after heating is turned off. The last three snapshots (from top to bottom and from left to right) are separated by a time interval $\sim 200\,\mathrm{yr}$. Note that the colour bar range shrinks between panels to highlight the effect.

the initially heated region. Eventually, however, the crescent becomes hotter than the central spot in the very late stages (when the temperature difference from the background is nevertheless very small).

In the case of a higher heat injection, $\dot{H} = 5 \times 10^{26}\,\mathrm{erg\,s^{-1}}$, a similar phenomenology can be observed, but a turbulent-like pattern of the temperature emerges, see Fig. 5.6. This results in a more complex evolution as the spot cools down after the heating is discontinued. Its relic, in fact, gets fragmented into many smaller structures that do not exhibit the ordered, ring-like shape of the previous case. Again, a drifting crescent-shaped subdominant structure is formed in the final phases.

Moreover, the backreaction of the temperature gradients on the magnetic field become important: in fact, in this situation a temperature gradient that is perpendicular to the (radial) density one is present, hence the Biermann battery effect, that has a negligible feedback effect in the long term evolution of isolated stars, becomes important and can give rise to a substantial local enhancement of the magnetic field. Such behaviour is

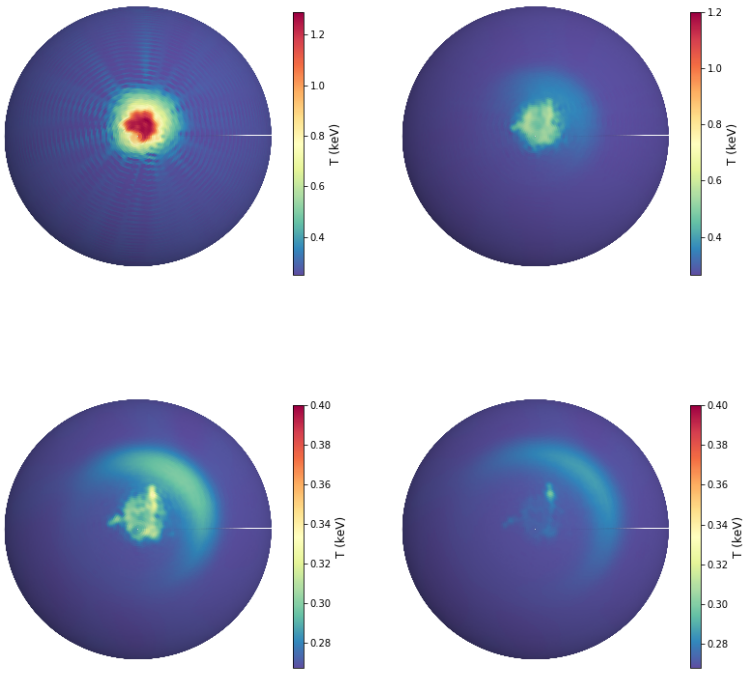

Figure 5.6: Cooling of a spot with the same geometry of the one in Fig. 5.5 but with a 10 times higher heat flux. Here, snapshots are separated by $\sim 300\,\mathrm{yr}$, with the first one referring to the time at which heating stops. Note that colour bar range decreases between the two rows to highlight the effect.

displayed in figure 5.7. When the stationary state is reached, some small magnetic structures appears on top of the $\approx 10^{12}\,\mathrm{G}$ large-scale (quasi) dipolar field, where the field strength can reach values up to $6 \times 10^{14}\,\mathrm{G}$. Note that the Biermann-battery generated field is perpendicular to the density gradient (see the first term of Eq. 3.25), so that the observed strong radial field is generated by the combined action of the battery itself and of the Hall term.

The cooling phase lasts some thousands years. It is therefore possible that the aftermath of powerful heating events can produce long-lasting thermal structures on a NS crust, evolving in complex patterns along field lines. Moreover, during these phases thermo-coupling effects, driven by the external heat injection, are able to create local magnetic structures, even if the magnetic field in the magnetosphere is very close to a dipole. As an example, Fig. 5.8 shows the external field lines as extrapolated for the last case at the instant at which the heating is turned off. After subtracting the contribution of the $m = 0$ modes, which are dominated by the dipolar field, a small magnetic field loop is clearly visible above the heated region, extending outwards up to a distance $\lesssim R_\star$

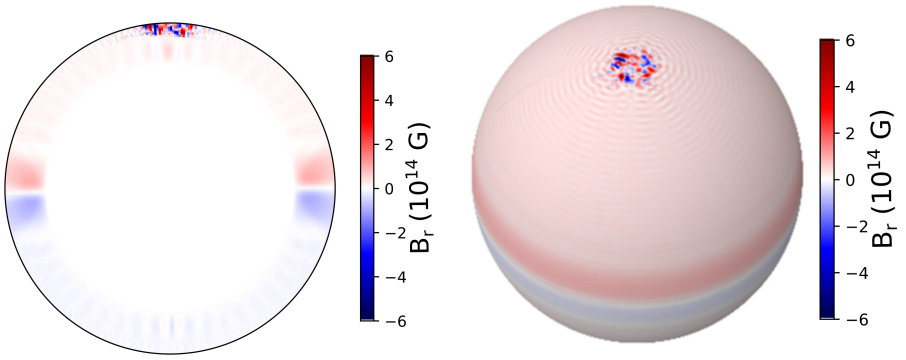

Figure 5.7: The radial component of the magnetic field in the localised heating steady state shown on the first panel of Fig. 5.6.

with a typical strength $\approx 10^9$ G. This shows that battery-generated structures are not necessarily confined into the crust, but can extend in the inner magnetosphere. This may bear to the localised magnetic structures hinted by the observations of proton cyclotron lines in the observations of some magnetars, like SGR 0418+5729 (Tiengo et al., 2013). Thermo-coupling effects, on the other hand, turned out to be less important in the case of deep heating, where the local enhancement of the magnetic field is modest.

Although only a limited number of cases were considered, a distinctive feature common to both deep and surface heating is the drifting of hot spots from the initially heated region as they cool, with a possible marked change in shape. This is a direct consequence of anisotropic heat conduction in the crust, which occurs essentially along the magnetic field lines. In this respect, a small degree of asymmetry of the position and shape of the initially heated region with respect to the magnetic pole is necessary for the formation of crescent-like structures during the evolution. As expected, heat injection in a circular patch exactly at the magnetic pole results in a nearly circular, cooling spot. However, simulations show that such deviations need to be indeed small, which in real sources may be produced by a variety of mechanisms, like e.g. the exact location of the crustal failure, the presence of sub-dominant non-dipolar components, or the effect of the coupling of crustal heating currents with the rotation of the star (Karageorgopoulos et al., 2019).

Non-polar, crescent-like hot spots have been recently detected in NICER X-ray observations of the millisecond pulsar PSR J0030+0451 and interpreted as due to heating from backflowing currents in a strongly non-dipolar magnetic field (Miller et al., 2019, see Fig. 5.9). The results discussed in this section show that such features may also form as thermal relics of past events of heat deposition even in presence of a dipole-dominated field, provided that proper account for the crustal transport properties is made. Even though the evolutionary history of PSR J0030+0451 is likely quite different from that of a passively cooling NS, and its (dipolar) field is lower than the one used in our model, a qualitatively similar behaviour of the crust may have caused the observed pattern even without invoking strong multipolar fields.

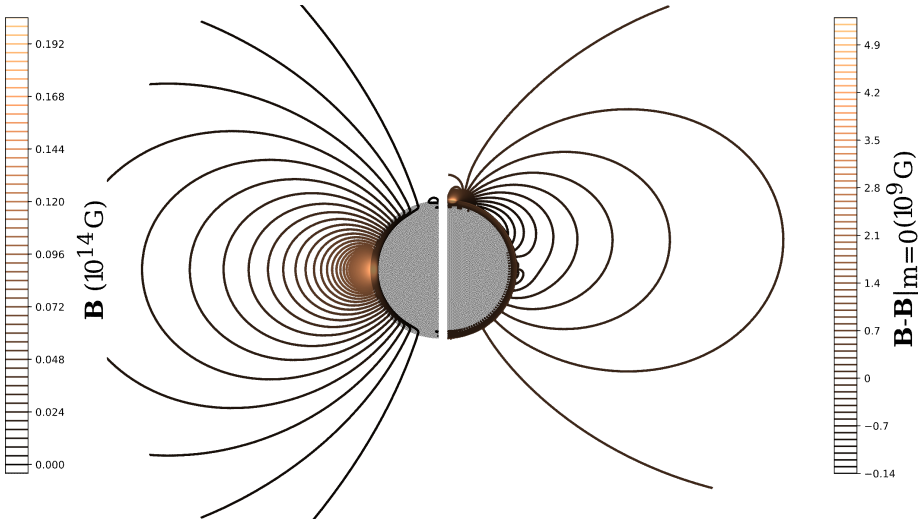

Figure 5.8: The extrapolated external magnetic field for the case in Fig. 5.7. The left half shows the total field and the right one the difference between the total field and its $m = 0$ modes, which are dominated by the dipole.

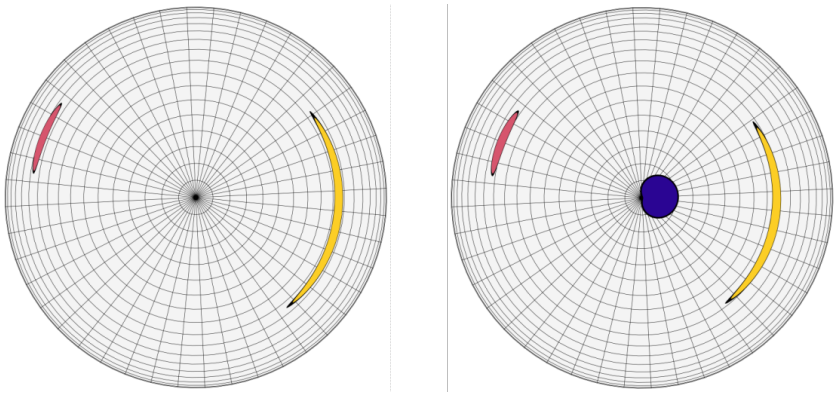

Figure 5.9: The two best fit models, with two or three spots, for the surface of PSR J0030+0451 as observed by *NICER*. Figure adapted from Miller et al. (2019).

Notwithstanding the intriguing similarities with observations, the simulations presented in this section suffer from the fact that timescales are not compatible with the observations of magnetar transient phenomena, which last at most $\approx 1\,\mathrm{yr}$, as well as with previous works in the field (e.g. Pons and Rea, 2012). This can essentially be attributed to the oversimplified microphysical content in the code. In order to have a more quantitative gauge, consider the heat diffusion timescale across a length L, which can be estimated as (Chaikin et al., 2018)

$$\tau_{\mathrm{diff}} \sim \frac{1}{4}\left[\int_L \mathrm{d}l \left(\frac{C_V}{k}\right)^{1/2}\right]^2, \tag{5.2}$$

and is hence regulated by the specific heat-to-thermal conductivity ratio. According to the estimates of Chaikin et al. (2018), for the typical conditions in a NS crust, the timescale of heat transport from an internal heater to the surface is $\lesssim 1\,\mathrm{yr}$, whereas in our model the value of the characteristic diffusion time across the crust turns out to be much longer, $\tau_{\mathrm{diff}} \approx 50\,\mathrm{yr}$. This calls for a major improvement of the treatment of the crustal model. A strategy to solve these issues and obtain more realistic models will be described in the next section.

5.2 Modelling Short-Term Evolution

As already mentioned, the results presented so far were obtained with a version of the `PARODY` code adapted to some assumptions for the microphysical input, which are adequate for the description of the secular evolution. Whereas some of them are deeply embedded in the core structure of the code, such as the analytical prescriptions for a T- and B-independent EoS and for the other transport quantities, some assumptions can be relaxed if one is only interested in short term evolution. In particular, two assumptions that stemmed essentially from computational time issues were related to:

Specific heat form the assumption that C_V is linearly dependent on the temperature is a good description for the electron contribution only, and does not take into account the contribution of the ion lattice which is actually the dominant one. This makes Eq. (2.26) dependent on T^2 only, allowing the code to invert the operator $\mathcal{A}$ in Eq. 3.3 as seldom as possible, ensuring the efficiency of the numerical scheme. This is a good enough approximation in the long term, as the term $\propto \partial T/\partial t$ is strongly suppressed, but becomes questionable when this term starts to dominate, as in the case of impulsive heating;

Crust-Envelope interface as magnetic and thermal evolution get faster at lower densities, the crust external limit has been so far set to a rather high value ($\approx 10^{10}\,\mathrm{g\,cm^{-3}}$) not to be limited by excessively small timesteps. This implies a thick thermal

blanketing envelope. However, short term events are expected to happen at much lower densities, where heat diffusion timescales are shorter and more compatible with the observed behaviour.

Both these points were addressed, upgrading the code so that it is able to deal with heat injection phenomena on realistic timescales.

5.2.1 Upgrading the Code

As to the first of the aforementioned points, a minimal model for the crustal specific heat can be written as (e.g. Potekhin et al., 2015)

$$C_V = C_V^{\text{lattice}} + C_V^{\text{el}} = 3k_B n_i + \frac{\pi^2 k_B^2}{m_e c^2} \frac{\sqrt{x_r^2+1}}{x_r^2} T \tag{5.3}$$

where, because of charge balance, $n_i = Z n_e$ and $x_r = p_F/m_e c$ is the adimensional Fermi momentum of electrons (Eq. 1.15). The first, temperature independent contribution describes a classical bcc lattice and the second one completely degenerate electrons. The first term is the dominant one up to very high temperatures (where the classical expression also becomes inaccurate). The issue with this expression is that the two terms have different temperature dependencies, so that no manipulation such as writing the equation in terms of T^2, as done before, can eliminate the T dependence in the LHS of the temperature equation. Using again an implicit integration scheme with this expression requires to invert the time advance operator $\mathcal{A}$ at every timestep, which would be computationally too costly. Instead, the whole temperature equation has been moved to the explicit part of the time advance algorithm, and treated with the Adams-Bashforth scheme. This is still more costly than using the implicit algorithm, but it does not alter the time for an iteration significantly. The magnetic evolution scheme has not been changed.

Secondly, the crust has been extended to incorporate the outer layers. This was done by using the simple model proposed by Yakovlev et al. (2021), who determine the adimensional Fermi momentum, from which the density follows, as a function of the depth z as

$$x_r^3 = \left[\frac{z}{z_0}\left(2 + \frac{z}{z_0}\right)\right]^{3/2} \quad ; \quad z_0 = \frac{Z m_e c^2}{m_u g_s A} \approx 10\,\text{m} \tag{5.4}$$

where the scale length z_0 is given in terms of the atomic mass unit m_u, and g_s is the gravitational acceleration in the local f.o.r. In the following, standard NS parameters ($M = 1.4\,M_\odot$, $R = 12\,\text{km}$, $g_s = 1.59 \times 10^{14}\,\text{cm}^2\,\text{s}^{-1}$) will be used, as well as a constant Fe composition ($Z = 26$, $A = 56$). For consistency, the density profile used so far, Eq. 3.32, has been kept, with the outer crust built on top of it from a density of $\approx 10^{11}\,\text{g}\,\text{cm}^{-3}$ downwards. The transition point was chosen with the additional requirement that the two profiles join smoothly (see Fig. 5.10); this implies that the width of the crust is increased by about 40%, and the region that is treated as a heating blanketing is actually quite thin. Nevertheless, the inner crust plays no role in the outburst physics, since it

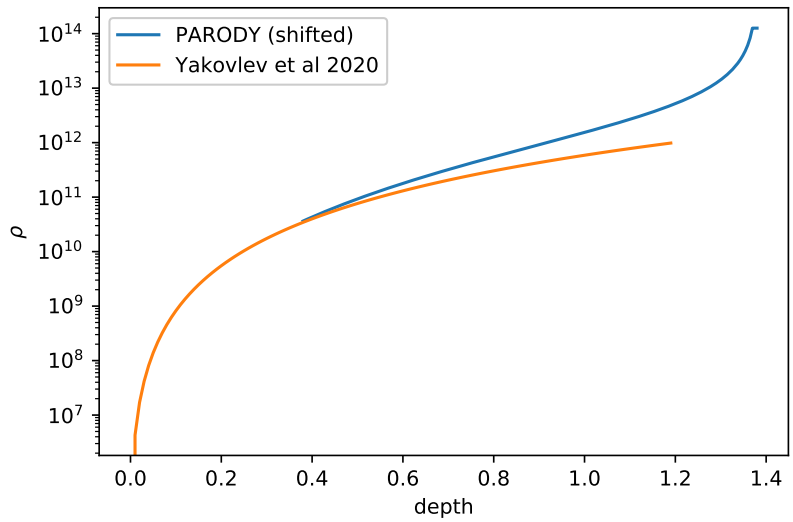

Figure 5.10: Updated density profile with the addition of the outer crust according to Eq. 5.4

virtually does not evolve on the relevant timescales and the details of its EoS (as well as the crossing point between the two profiles, which is quite deep) is hence irrelevant, as already noted by Yakovlev et al. (2021) themselves.

A numerical challenge caused by this more accurate treatment of the short-term evolution is related to neutrino emission. In fact, neutrino loss terms have a strongly non-linear dependence on temperature ($N\nu \propto T^7$–T^8) and treating them on short timescales with an explicit algorithm such as the one implemented in `PARODY` is problematic. Treating them consistently up to very high T, in fact, may require extremely small timesteps, to the point that machine precision is reached in some terms that hence cannot get properly updated. For this reason, the timestepping algorithm has been left unaltered and a numerical check imposed on the neutrino loss term. In particular, if the timestep is too large the neutrino emission can be overestimated and *overshoot*, resulting in a negative temperature in correspondence of what was a very hot point. This has been prevented by requiring that at each time iteration the temperature of any given point could not decrease by more than 50% of its original value. This mimics the fast cooling, relaxing it over a more manageable time, which has nevertheless checked to be limited to few time iterations.

With these modifications to the code, it is now possible to turn to the study of short term phenomena. In particular, in the remainder of this section a model for transient magnetar outbursts (see Sec. 1.4.1) will be presented. Note that in these cases the battery term in the induction equation has been removed, since it gives rise to numerical issues; the study of its effects is postponed to future work (see Sec. 5.2.3).

5.2.2 Modelling Outbursts

In this section[1], a set of simulations intended to model magnetar outbursts will be presented. While it is not a new idea to study transient magnetar outbursts using codes initially developed for describing NS cooling (without a magnetic field, i.e. in 1D, e.g. Yakovlev et al., 2021, and other works by the same group) and magnetothermal evolution (in 2D, Pons and Rea, 2012, in the following PR+12), this work will for the first time exploit the advantage of using a fully 3D treatment, which is essential to reproduce the hot spot-like structure suggested by observations.

There is currently no clear picture as to which the exact mechanism causing the heating of the observed hot-spot may be. Since most transient NSs have a large spin down field or other signatures of strong fields (such as the proton cyclotron scattering line in SGR 0418+5729, Tiengo et al. 2013) the general consensus is that some kind of fast magnetic energy dissipation is taking place in the outermost layers of the crust. This may be triggered from inside the crust (e.g. by a mechanical failure due to magnetic stresses, see Sec. 4.2) or from outside by very strong backflowing currents or some other dynamics of the field in the lower magnetosphere; regardless, the addition of an external heating term provides an agnostic way of studying how the event unfolds with different conditions.

In order to match the observed risetimes ($\lesssim 1\,\mathrm{d}$), the heating phase should be quite short, lasting much less than the overall duration of the event. As already noted by PR+12, the actual value of the injection time Δt is irrelevant for the subsequent evolution as long as the total (time integrated) injected heat H is the same and Δt is not much longer than the characteristic heat diffusion time across the crust; in this case, a quasi-stationary state may develop (see Sec. 5.1.2). For the cases considered here, it has been verified that values $\lesssim 1\,\mathrm{h}$ yield indistinguishable results. The introduction of a smoothing function in time has been verified to produce no effect, as well.

The heating term has been added into a spatially localised region in the external crust ($\rho \approx 10^7\,\mathrm{g\,cm^{-3}}$) with a thickness of $\approx 100\,\mathrm{m}$ and a diameter of some kilometres to reproduce the observed hot spot areas. The modulation function $s(r, \theta, \phi)$ used in this case is a $\sin^4$ profile centred at the centre of the heated region in all the three directions r, θ and ϕ. Note, however, that since crustal neutrino emission is very non-linear and much stronger in the hotter zone at the centre of the patch, the temperature profile tends to be flattened out, so that the exact form of the smoothing profile is not crucial.

Neutrino saturation Another effect of crustal neutrino emission, which was already observed by PR+12 in 2D, is the saturation of the maximum (photon) luminosity with the growth of the total heating input. In fact, neutrino emission processes in the crust get abruptly triggered above $T \approx 3 \times 10^9\,\mathrm{K}$ (see App. A). This implies that, keeping all the other parameters unaltered, as the total heat input H increases a greater and greater fraction gets quickly dissipated in the form of neutrinos, without contributing to the

[1]Part of the results presented in this section were obtained in collaboration with Elisa Lucchetta for the completion of her MSc Thesis.

thermal radiation emission.

This effect has been tested taking a background NS with an initial crustal temperature of 10^8 K and a dipolar field of 10^{13} G. The field has again been built as the poloidal part of a force free field. It has also been checked that the inclusion of a toroidal component, even much stronger than the poloidal one, has virtually no direct effect on the outburst, since it is confined in the deeper layers by the requirement of negligible magnetospheric currents (the boundary condition Eq. 3.36). In these cases, the heating term has been activated few time iterations after the beginning of the simulation, so that the magnetic configuration is virtually the same as the initial one. The heated patch is located at $\rho \simeq 3 \times 10^7\,\mathrm{g\,cm^{-3}}$ and covers a rather large area ($\sim 20\%$ of the surface). Albeit not completely realistic, this has been purposely done for two reasons. The first, of more practical nature, is that very large energy inputs are required in order to observe the saturation, implying steep thermal gradients that are problematic to treat within a spectral scheme; enlarging the heated region produces smoother, more numerically manageable gradients. The second point is a generality one: as it will be shown in detail later, the location of the heated region with respect to to the magnetic field geometry is important for the lightcurve shape, so that the use of a large patch has been preferred in order to average out these effects.

Fig. 5.11 shows the different luminosity curves obtained varying the heat input. As in the previous section, in this case and in the following ones the luminosity has been computed assuming a patch-wise blackbody emission. The general behaviour is coherent with what observed in real sources (and qualitatively similar to the curves in PR+12): a rise time of hours to $\lesssim 1$ day, faster as H increases (and hence the peak gets higher) and an overall duration $\gtrsim 100$ d, longer for the brighter cases. This time span is too short for the field to undergo a significant evolution. The general shape of the curves does not change much between the various cases. Upon visual inspection, the curves appear to be piling up as H increases. In order to get a more quantitative evidence of this effect, the peak luminosity (in the local f.o.r.) and rise-time have been plotted against the total injected heat H as shown in Fig. 5.12. The saturation effect, then, becomes evident: after the heating becomes larger than $\approx 10^{44}$ erg, the luminosity increase become very small, and the rise-time almost unchanged as larger and larger H are injected.

Dependence on the injection density The cases considered so far considered the same depth of the heat injection. Nevertheless, injecting the same H at different depths—and hence at different densities—has two effects: first, since the specific heat is different, the resulting temperature variation will not be the same. Second, the deeper the injection the longer the distance that heat need to travel to reach the surface and alter the luminosity will be. Fig. 5.13 shows different the lightcurves corresponding to the same injection of $H = 2.9 \times 10^{40}$ erg in the same patch or radius $\simeq 2$ km, in a shallow layer at different depths in the outer crust. The equation of state there shows quite significant variations with depth (see Fig. 5.10), and the shape of the lightcurves themselves turns out to be quite sensitive to the injection depth. In fact, as the depth increases the risetime becomes longer and the peak lower, as shown in Fig. 5.14. This effect is in part

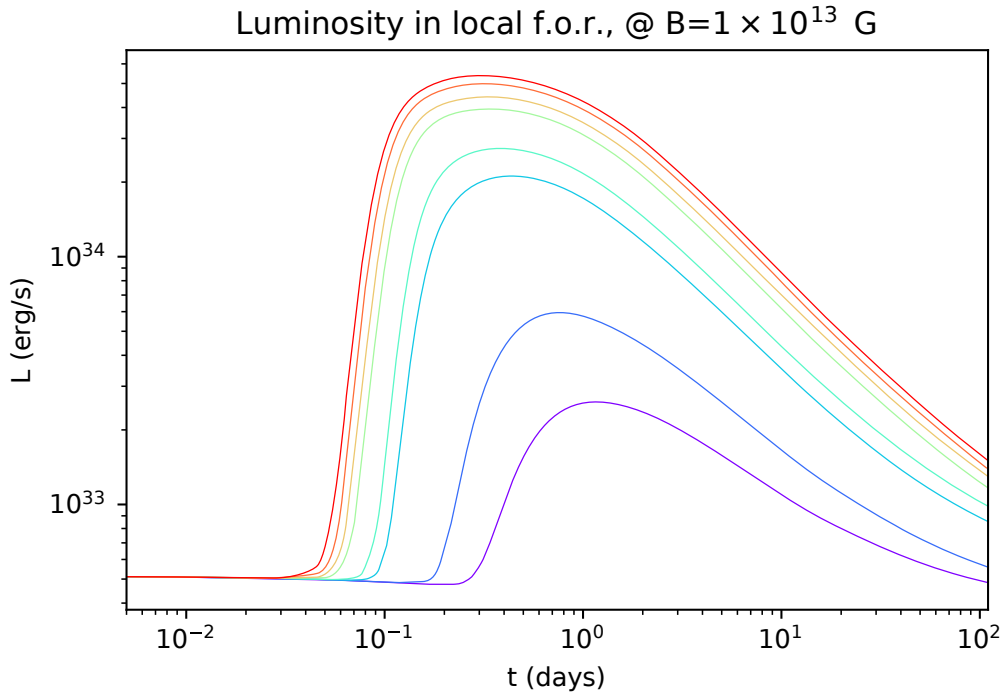

Figure 5.11: Luminosity curves after the injection of increasing amounts of heat; higher curves correspond to higher H (see Fig. 5.12 for the values) for a NS with $T(0) = 10^8\,\mathrm{K}$, $B \sim 10^{13}\,\mathrm{G}$.

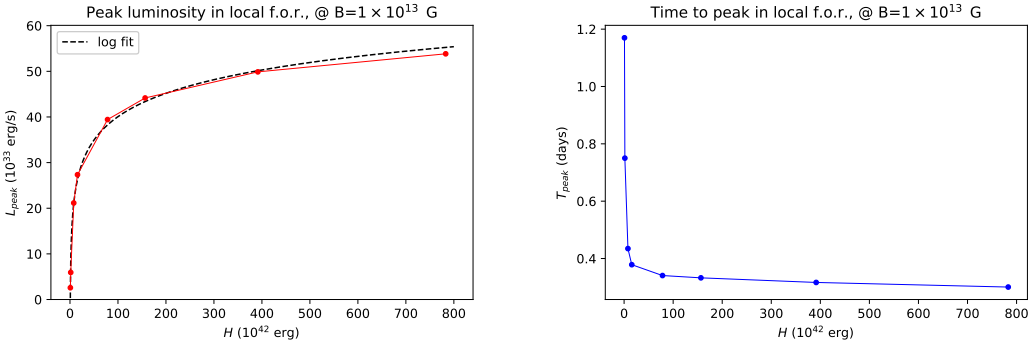

Figure 5.12: Peak luminosity and rise-time as a function of the heat injection for the curves in Fig. 5.11. In the first panel, a logarithmic fit to the points has been added as a reference.

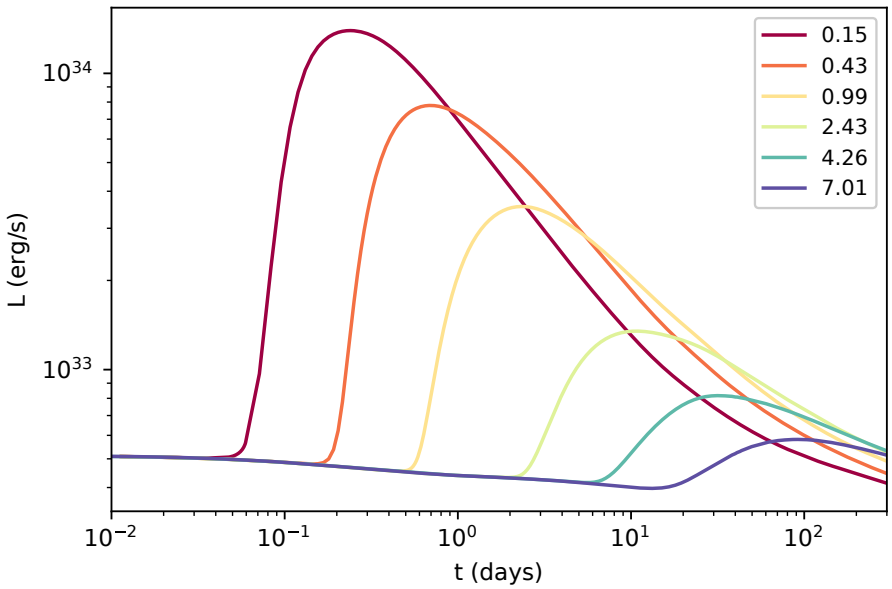

Figure 5.13: Lightcurves corresponding to the injection of the same $H \simeq 2.9 \times 10^{40}$ erg at different depths. The curves are labelled with the value of average density in the injection region in units of $10^7\,\mathrm{g\,cm^{-3}}$.

degenerate with the variation of the total energy input H, but when considering the combined effect of neutrino saturation it points to an origin of outbursts from heating in the outermost layers of the crust. On the other hand, heating in the deep layers may indeed reach the surface, but in too small amounts to cause a proper outburst, and may be confused with a variation of the background luminosity.

Dependence on the magnetic field strength The runs presented so far started from the same purely dipolar field with $B \simeq 10^{13}\,\mathrm{G}$. In order to asses how the outburst lightcurves depend on the magnetic field, two aspects must be considered: strength and direction of the lines. To tackle the former, let us consider a heat injection of $H \simeq 3 \times 10^{40}\,\mathrm{erg}$ in a $\approx 5\,\mathrm{km}$ radius patch, centred on the magnetic pole; the injection density is again $\rho \approx 3 \times 10^7\,\mathrm{g\,cm^{-3}}$. The resulting luminosity curves are shown in Fig. 5.15 for field strengths varying between 10^{12} and $10^{14}\,\mathrm{G}$; in order to focus on the evolution of the heated patch, the evolution of the background (namely, the heating of the equatorial belt) has been subtracted out. In these cases, the time-step Δt has been kept fixed to a small value ($\approx 1\,\mathrm{min}$) in order to avoid any potential inconsistencies caused by the anti-overshooting algorithm used to treat neutrino losses, which may arise due to the dependence of the ideal timestep value on the field strength. The timing properties of the curves, in particular the instants of the rise onset and of the peak, show no significant

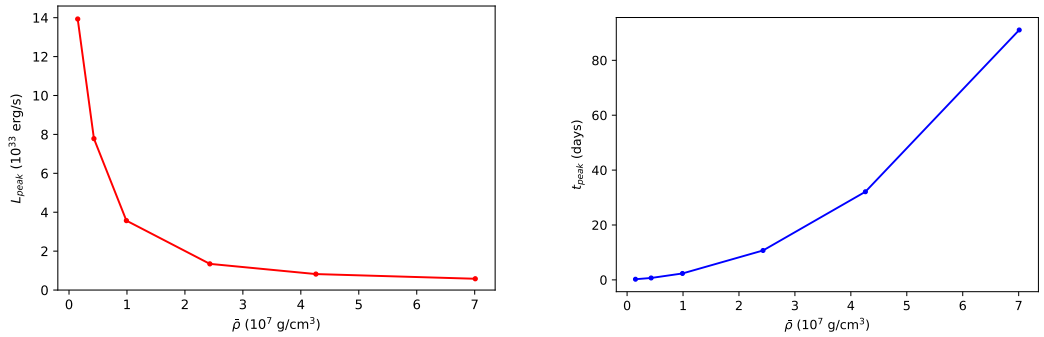

Figure 5.14: Peak luminosity and rise-time a function of the average density for the curves in Fig. 5.13 at different injection depths.

variation, and the overall shape is almost identical. Alongside the true luminosity at the surface, the figure also shows the evolution of the surface integral $\int T_b^4 \mathrm{d}S$, representing the "luminosity" as computed using the top-of-the-crust temperature (again, subtracting the background). These curves also show no significant variations amongst each other, but it is nevertheless remarkable how the order of these curves is reversed with respect to the true luminosity. In fact, since the magnetic field acts as an insulator, one may expect to find lower peaks for stronger fields, by reason of the presence of a field component that is orthogonal to the heat propagation towards the surface (which in the polar regions is nevertheless quite small). This is indeed the case, as shown by the integrated T_b, but the effect of the envelope is not as trivial. In fact, in the heat-blanketing envelope the longitudinal heat conductivity, which drives the heat transport near the pole, gets amplified by electron quantisation effects; this makes the envelope polar regions more transparent to heat as the field grows (the effect is the opposite near the equator, see Beznogov et al., 2021, in particular their Figure 22). In the case at hand, in which the hot region is indeed polar, this ends up reversing the hierarchy between the two families of curves in Figure 5.15. At any rate, the qualitative differences between these lightcurves are small enough not to require a complete exploration of the other effects at different field strengths, so that the representative value $B \simeq 10^{13}\,\mathrm{G}$ will be considered in the following.

Dependence on the magnetic field geometry Let us now turn to the effects of the field geometry in the injection region. To this end, the same patch of the previous run was considered, this time with $H = 4 \times 10^{40}\,\mathrm{erg}$, but it was put at two different locations. In one case, it lies around the magnetic pole, while in the other it crosses the equator (in practice, this has been realised by rotating the field rather than the patch itself, so that its position with respect to the grid is unaltered). These two positions are representative of a geometry where lines are mostly "open" (perpendicular to the surface) or "closed" (normal to it), respectively. The evolution of the lightcurves is shown in Fig.

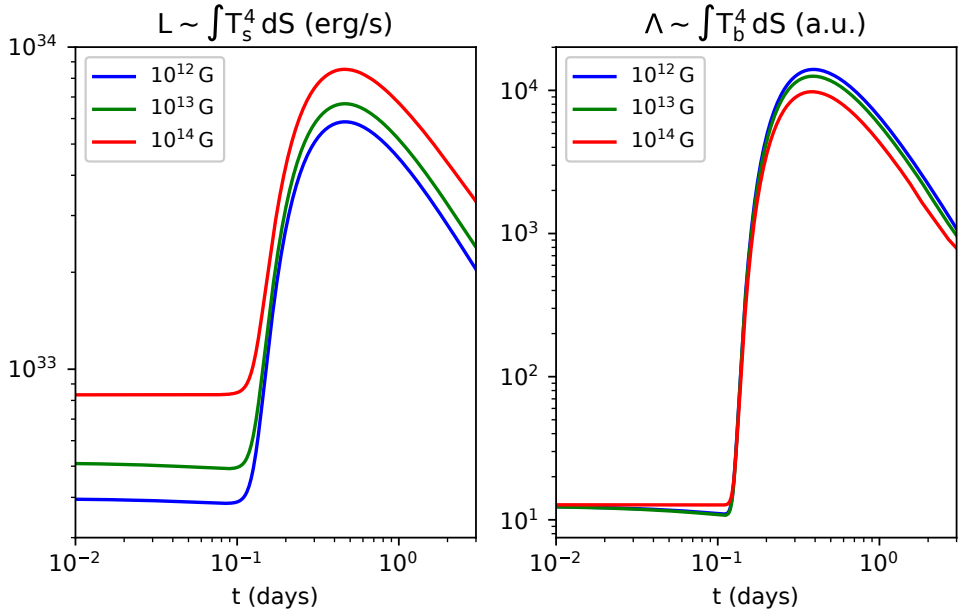

Figure 5.15: Evolution of the luminosity and of the "crust-top luminosity" in the first phases of an outburst for three different strengths of the (dipolar) magnetic field. The heating H and the heated region, placed symmetrically around the pole, is the same in all three cases.

5.16. This time, two different envelope compositions have been studied, including a light element envelope (the "fully accreted" model from Beznogov et al. 2021) alongside the Fe-Ni composition considered so far. The accreted envelope is more transparent, so that the luminosity is higher for the same internal temperature. This also means that the radial temperature gradients are larger, so that a somewhat long transient phase ($\lesssim 1\,\mathrm{yr}$) must be considered before starting the heat injection to allow for their formation in the initially isothermal crust; this phase is of almost negligible duration (hours) with the more blanketing envelope, that yields a smaller gradient. The most important effect in shaping the lightcurves is indeed the different position: in the cases in which the injection is in the equatorial zone, the risetime is longer, the peak luminosity lower and the event lasts for a longer time overall. Contrariwise, even though they have different magnitudes, the curves with different envelopes and same heating location have very similar timing and only small differences in the slopes at the various phases.

This behaviour is understandable in terms of the thermal insulation properties of the magnetic field. Much in the same way as magnetic insulation in the envelope creates a cold belt where field lines are parallel to the surface, see Ch. 4, the diffusion of the injected heat towards the surface is thwarted across field lines inside the crust itself. The retention of higher temperatures also imply an enhanced neutrino dissipation. The difference is not only in the energy output, but in the very shape of the hot spot. Fig. 5.17 shows the shape of the hot region during the rise phase; if in the polar case the nearly circular shape of the injection is preserved, the same spot emerges in the equatorial case as two separate lobes, that then tend to merge. Due to the envelope effect, the spot across the equator continue to manifest as two zones.

Note that the cases considered in the last examples have a quite modest luminosity variation compared to the maximum allowed before saturation. This has been done deliberately, both in order to reduce at a minimum the necessity to cure neutrino overshooting and to maximise the differences between the different cases. In fact, if the injected heat is very large, the regime of neutrino saturation is entered and all the luminosity curves get close to each other, with all the various effects studied here end hardly distinguishable.

In conclusion, the new version of the code is able to model the unfolding of heat injection events on realistic timescales, yielding a general behaviour that matches both the observations and the previous works on outbursts. In particular, 3D simulations highlight the paramount role of the magnetic field, chiefly with regards to its geometry. What is more, the cases presented here are only demonstrative of two simple situations, whereas the reality is probably more complex. In case the heat injection happens in an intermediate region, different degrees of heat retention will be present in different zones; as an example of this, Fig. 5.18 shows one of the large spots used to study neutrino saturation (namely, the second lowest curve, $H \simeq 1.6 \times 10^{40}\,\mathrm{erg}$, after $t \simeq 9\,\mathrm{d}$). Even though the energy was injected with a maximum at the geometrical centre of the patch, the region across the equator has retained a larger amount of heat (which again is not directly translated in a hot surface spot due to the effect of the envelope), while the one closer to the pole has cooled down more quickly.

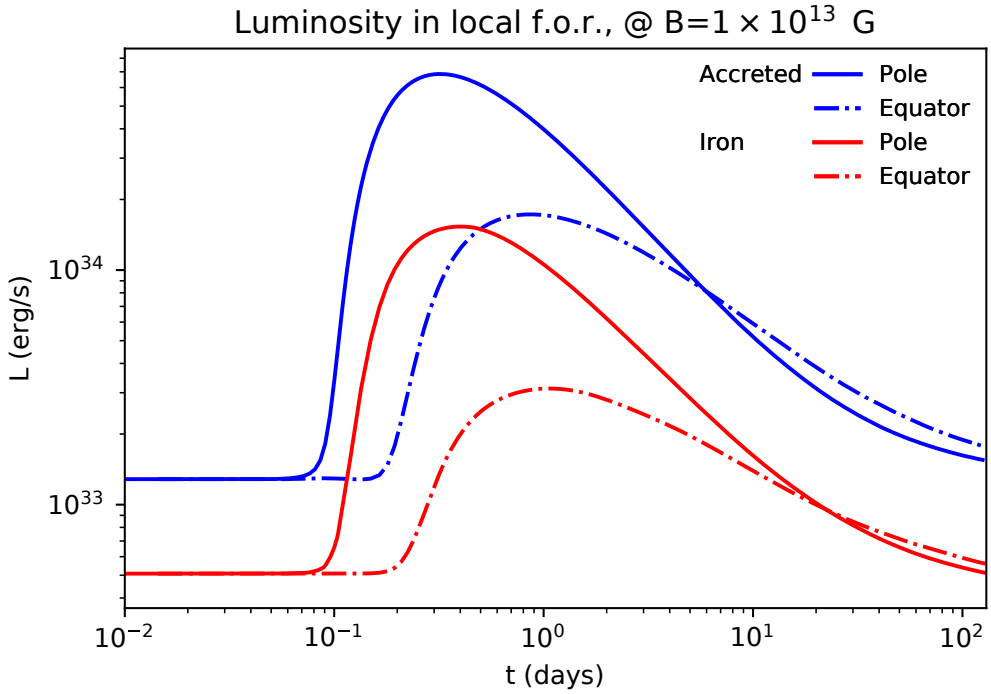

Figure 5.16: Outburst evolution for a NS with $B = 10^{13}\,\mathrm{G}$ and an injection of $H \simeq 4 \times 10^{40}\,\mathrm{erg}$ in two different positions with respect to the dipolar field: around the pole (continuous lines) and across the equator (dot-dashed lines). Two different envelope compositions are considered, a Fe-Ni one (red curves) and a light-element, accreted one (blue curves). The evolution of the background state has been subtracted out for a better comparison.

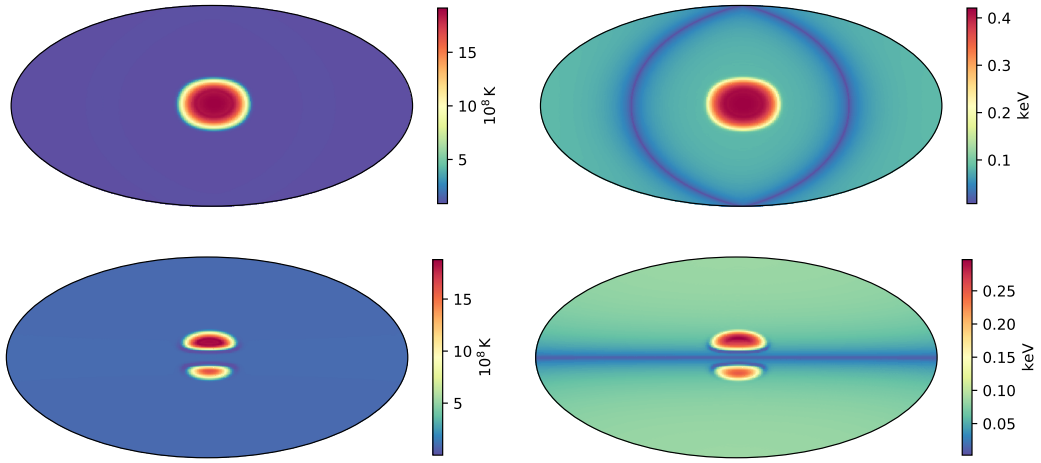

Figure 5.17: Thermal maps for the cases shown in Fig. 5.16 after $t = 9\,\mathrm{h}$ (rise phase) for the Fe-Ni envelope. The top row shows the case of polar injection (magnetic pole towards the observer), while the bottom one the equatorial injection (magnetic pole upwards); the left panels show the crustal temperature T_b, while the right ones the surface temperature T_s.

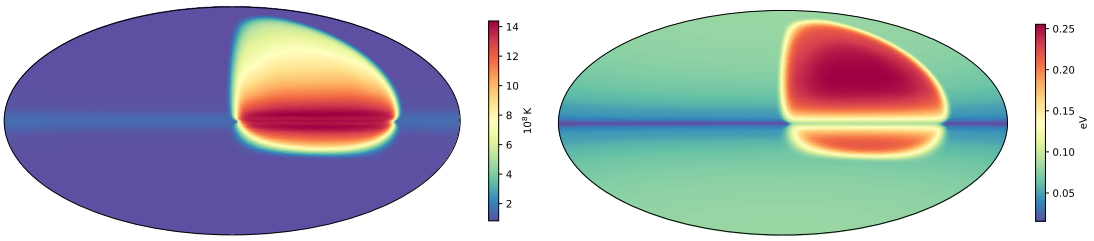

Figure 5.18: Thermal map at the crust top and surface (Fe-Ni envelope) for the second lowest curve in Fig. 5.11, after $H \simeq 1.6 \times 10^{40}\,\mathrm{erg}$, after $t \simeq 9\,\mathrm{d}$.

Other aspects that give space to further study, considering also an application to real events, are models of partially accreted envelopes and of realistic chemical stratification in the outer crust, an improved model of the conductivity that allows the relaxation time τ to be more than a constant, as well as battery effect that, as already mentioned, were not considered here due to numerical issues.

These results confirm that there is indeed a strong correlation between events of heating in the crust and the observed magnetar outbursts. As already mentioned, however, the origin of the heating process is still poorly known; even though a magnetic trigger is generally accepted, it is unclear whether this comes from inside the crust itself (though a crustal failure like the one described in Sec. 4.2). The results presented here suggest that the heating events producing outbursts should happen in the outermost layers of the crust. On the one hand, this may suggest a magnetospheric origin, with currents resulting from a catastrophic rearranging of the ultra-strong magnetic field heating the crust from outside; on the other, the low-density layers of the crust are more prone to failing due to the build-up of internal magnetic stresses. Moreover, the many parameters influencing the unfolding of the outburst come up against the comparatively small number of observations: to date, the Magnetar Outburst Online Catalogue reports only 23 events from 17 sources. Further data are then needed to allow for a proper statistical treatment against models. With new X-ray facilities line *IXPE* and *ATHENA* coming online in the near future and the revived interest in magnetar activity thanks to its association to FRBs (Mereghetti et al., 2020), it is not unreasonable to expect substantial advances of the field in the foreseeable future.

5.2.3 Beyond Dipolar Fields

In the outburst models presented thus far, the background field has been assumed to be purely dipolar, with the short time-span of the events hindering any sizeable change in its topology. Nevertheless, even with such a simple configuration the paramount role of the magnetic topology became apparent, which naturally prompts the exploration of different, more complex fields that may be present in any stage of the evolution. In this respect, there are at least two aspects to be addressed: a multipolar background field—which may be present in magnetar both as the result of PNS magnetic amplification or of the Hall cascade—and additional field components created by the heated region itself via battery effects.

Highly multipolar fields can indeed be present in a NS for a variety of reasons: they come as the imprint of a dynamo process that amplified the field in the PNS phase, or as the manifestation of the Hall effect, either in a orderly way pointing toward the Hall attractor or as the result of an eMHD instability. In order to test how such a field affects an outburst-like situation, a highly multipolar has been built in the same fashion described in Sec. 4.4. The power spectrum of the initial magnetic field is shown in Fig. 5.19, and has been modelled to mimic the one obtained by Gourgouliatos et al. (2020) studying the Hall effect. A heating term of $H \simeq 5 \times 10^{38}\,\mathrm{erg}$ has then been placed in a shallow region with $r \simeq 5\,\mathrm{km}$ at $\rho \simeq 6 \times 10^{7}\,\mathrm{g\,cm^{-3}}$. Fig. 5.20 shows the resulting spot on the surface after $\approx 21\,\mathrm{d}$, during the rise phase. The shape and dimension of the injection

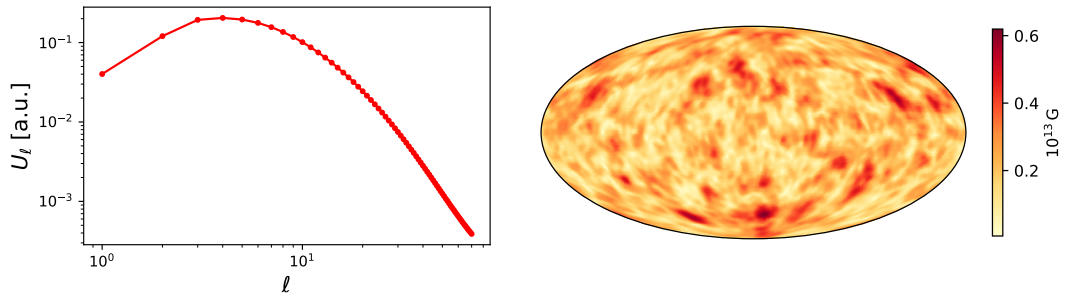

Figure 5.19: Power spectrum and surface strength of a highly multipolar field built like the one in Sec. 4.4.

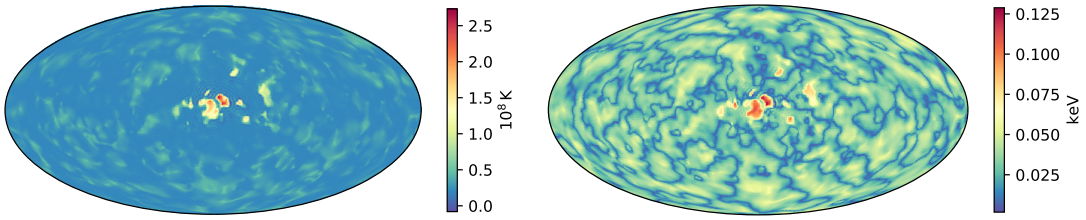

Figure 5.20: Hot-spot formed after a heat injection event in a model with the multipolar field from Fig. 5.19. The temperature maps are shown in Hammer projection both at the crust top *(left)* and on the surface, above the envelope *(right)*.

is similar to that of the previous section, but it now manifests in a number of smaller surface spots, over a surface that is made patchy itself by the magnetic field. The same phenomenology studied in the dipolar case altering the heating position is at work on a smaller scale in different zones of the hot zone, with heat finding preferential routes towards the surface where the field is in the most favourable alignment.

Hence, a small-scale field induces small-scale thermal features after the injection, amplifying thermal gradients. As already mentioned, however, these gradients are particularly problematic to treat within the framework of a spectral code, so that the evolution of this event could not the further followed, even though relatively small magnetic field strength and heat input values have been chosen.

The very same problem makes the study of battery-induced fields problematic. As already mentioned, in fact, in the last section the battery term had to be removed from the induction equation to be able to treat all the heating cases. Moreover, relatively large heated areas were studied. Taking smaller and hotter spots, while being more realistic, boosts thermal gradients, which results in numerical issues that disrupt the simulation. These are also the conditions in which the Biermann battery is able to operate efficiently. This efficiency, however, causes the formation of steep magnetic field gradients, which further complicate the numerical handling of the problem. The very presence of this issue leads to the idea that battery fields can indeed be a part of the physics of magnetar

outbursts, but their study has to be postponed to further work.

CHAPTER 6

Conclusions

This Thesis has been devoted to the study of the evolution of the magnetic field and temperature in Neutron Stars, addressing in particular how they are intertwined. This problem is described mathematically by two strongly coupled non-linear partial differential equations, which have been solved numerically within a 3D framework. In particular, the results presented here are the first self-consistent 3D simulations of magnetised NSs with realistic temperature boundary conditions (Ch. 4) and a realistic treatment of the specific heat, which is key in describing short-term activity (Ch. 5).

A multi-dimensional treatment is required to treat the magnetic field properly, considering both its strength and direction, which is not possible in 1D models (i.e. those assuming spherical symmetry). Furthermore, a 3D treatment allows one to appreciate several effects that are inhibited by symmetry assumptions that can reduce the problem to two dimensions. In particular,the addition of the third dimension allows one to appreciate:

- the differences between the thermal structure of the crust and the ensuing surface thermal maps when produced by axisymmetric or non-symmetric fields. The latter yield a larger variety of lightcurve shapes with higher pulsation, but cannot support large, long-term temperature anisotropy in the crust;

- the role played by eMHD instabilities in shaping the field and, possibly, in causing the activity of magnetars. In 2D, the appearance of instabilities is suppressed by the symmetry requirements, while strong toroidal fields in 3D have been observed to trigger them. These instabilities lead to the formation of small structures in which the magnetic field is enhanced and the temperature rises, creating the ideal conditions for the crust to fail;

- the many effects at play in the unfolding of crustal heating events, which are associated to magnetar outbursts. Hot-spot structures are inherently asymmetric and their evolution has been shown to depend strongly on the structure of the crustal magnetic field as well as on other physical conditions at the heating location.

The addition of a third dimension is therefore key in revealing new phenomenologies which can help in describing the diverse behaviours observed in neutron stars. In this work, in particular, an ideal target for comparing magnetothermal simulations with physical objects was found in the class of XINSs, which emit purely thermal radiation in the X-rays. Among them, the unique characteristics of RX J1856.5-3754 (low pulsed fraction, but a small hot structure on the surface) were related to a highly symmetrical state resembling the Hall attractor. This relation had been hinted in previous works, but only the inclusion of the thermal structure of the whole crust alongside the pattern that the magnetic field induces on the surface is able to well reproduce the observed spectral and timing parameters. On the other hand, inherently asymmetric fields yield higher pulsed fractions and a wider range of shapes of the lightcurves, as observed in other NSs.

The magnetic field geometry is also absolutely crucial not only for the activation, but for the whole subsequent unfolding of transient magnetar outbursts. In this work, a set of models of heat injection in the crust have been studied, reproducing the main characters of these events as observed in real sources. Even though only a set of representative cases has been addressed, it has been shown how the physics of outbursts is affected by many different parameters, pertaining both to the background star onto which the event unfolds and the properties of the heat source itself. It then appears clear that with a broader range of models and a larger observational statistic coming from new data (to date only ≈ 20 outbursts have been observed) magnetothermal models will be fundamental in understanding the physics of NS transient events and constraining the properties of the underlying NSs.

The advantages of a 3D treatment, however, come at a cost: the high computational demand associated with a 3D integration domain forces one to accept some rather tight constraints on the microphysical input that can be incorporated in the code. In particular, the code does not treat the whole star, but rather it considers the crust only, where the ultra-strong field resides and the Hall term is active. This approach relies on the assumption of complete magnetic flux expulsion in the early phases after the superconducting transition of the core, which is probably an oversimplification. Moreover, simplified analytical prescriptions of the density profile and of the other transport coefficients in the crust has been employed. State-of-the-art microphysical models, resulting from complex microscopic calculations, are typically made available in the form of large tables to be interpolated (e.g. the widely used results at `http://www.ioffe.ru/astro/conduct/`); such a tool hence requires the handling of large datasets, which is computationally very expensive. Therefore, their use is not feasible with the current setup, considering also that the code has been run on modern HPC facilities for rather long wall-clock times.

Still, more than dispraising one or the other approach, this indicates how 1D models and higher-dimension ones are complementary and should inform each other. In fact, some trade-offs between the large degree of microphysical refinement of symmetric models and the computational challenges posed by a higher dimension domain will always be necessary. The general lessons that different models are able to teach must hence be combined to get a whole picture of the physical processes going on in a NS, with the final

target of interpreting real-world observations.

Another critical point that is only indirectly touched in this work is the choice of the most appropriate initial conditions for the magnetic field. The general approach followed in the literature (as well as in most of the cases considered here) is to take a large-scale structure that cascades to the smaller scales via the Hall effect (whether orderly in a Hall-attractor-like fashion or via an eMHD instability). This may however not be the most realistic case, since the mechanisms behind the formation of ultra-strong magnetar fields are still uncertain, and some models require a small-scale dynamo process producing a complex magnetic field. Magnetothermal evolution simulations in the Hall era have to rely on the choice of their initial condition, but they can help putting constraints on them *a posteriori*. In fact, as it has been observed in this work, different initial conditions produce remarkably different thermal structures, from the ones produced by efficient heat trapping by very symmetric configurations (see Sec. 4.1.1) to the asymmetric maps associated to more complex but still mostly large-scale fields (see Sec. 4.3) and even to the patchy thermal structure of highly disordered fields (see Sec. 4.4).

While this work explored several possibilities for the use of 3D simulations in NS physics, there is still room for new phenomena and improvements of the model. The microphysical input in the model can be updated, with the inclusion of more detailed models of the crust chemistry and of the overall hydrostatic model, comprising the core. The core itself can be included in the integration domain, studying its thermal evolution consistently and including the effects of a core threading field. On the other side of the crust, a self consistent model of the magnetosphere could be included, which would help to address the role of multipolar field components in the spin-down evolution and the non-thermal hard emission. Moreover, the physics of magnetars outbursts still can be addressed in more depth, considering the role of battery-generated fields and attempting a systematic comparison with observational data.

To sum up, multi-dimensional numerical tools are of great benefit in our understanding of astrophysical phenomena. Technical advancements that will make it possible to use them systematically will help us to understand the known phenomena in the high-energy sky, as well as those that will be observed in the future thanks to the new efforts in the dawning field of multi-messenger astrophysics.

APPENDIX A

Neutrino processes in NS crusts

Neutrino emission plays a key role in the thermal evolution of a neutron star. As outlined in Sec. 2.1, neutrino production in the core of a NS drives the evolution of its temperature for the first $\approx 10^5$ yr and provides an invaluable tool for the exploration of its equation of state and composition. In fact, the presence of different particle species and states of matter opens different reactions, each influencing the cooling process in its own way.

Alongside this host of reactions, the condensate state of the crust allows for even more neutrino emission mechanisms. As a general rule, these become effective at rather high temperatures, $T \gtrsim 10^9$ K, hence are able to affect the long term thermal evolution only in its very early phases. It is however an observational fact that transient phenomena in magnetars are linked to re-heated zones in the crust, which enhance the X-ray flux up to several orders of magnitude (Coti Zelati et al., 2018); in this context, understanding crustal neutrino emission is critical to address the unfolding of these events. In this section, the four main contributions considered in this work are reviewed; a more thorough treatment these and other aspects of neutrino emission in NSs can be found in the comprehensive review by Yakovlev et al. (2001).

Plasmon Decay Even though it possesses an electro-weak coupling, an isolated electron cannot spontaneously emit a neutrino pair due to energy-momentum conservation. However, the interaction with other electrons may provide enough momentum to open the reaction

$$\gamma \to \nu + \bar{\nu}$$

where γ denotes the collective mode of electrons (a *plasmon*) and the neutrinos can be of any flavour. This process is active at not too high densities in the crust and high temperatures. It is actually the dominant neutrino emission process at $T \gtrsim 3 \times 10^9$ K, while it becomes negligible below some 10^8 K. Therefore, it drives the cooling in the very early NS phases and in outbursts, while it is negligible for the long term cooling.

Neutrino Bremsstrahlung As electron move across the Coulomb lattice of nuclei in the crust, they may have an electro-weak interaction with them, giving the neutrino production channel

$$e^- + N \to e^- + N + \nu + \bar{\nu}$$

where N stands for a nucleus. This process may involve both charged and neutral weak currents, so that it can emit a neutrino pair of any flavour. It is one of the main sources of neutrinos from

the crust. Contrary to the other processes considered here, it does not involve only electrons but also nuclei, so that it is sensitive to the chemistry of the crust.

Pair Annihilation While the crust can be treated to a very good approximation as a completely degenerate Fermi gas of electrons, the thermodynamic equilibrium condition implies that a small fraction of positrons is present. These positrons can annihilate with an electron, producing a neutrino pair of any flavour,

$$e^- + e^+ \to \nu + \bar{\nu}.$$

The positron fraction is higher for low-density, non degenerate plasmas at very high temperature ($T \gtrsim 10^{10}\,\mathrm{K}$), so that this neutrino production channel is mostly important in environments like supernoveæ. In degenerate plasmas it is suppressed because of the tiny fraction of positrons, but it can nevertheless happen in a hot enough NS crust.

Synchrotron Emission As electron gyrate around magnetic field lines, they can emit a curvature radiation in the form of photons. However, the weak coupling of electrons also opens the process of synchrotron emission of neutrinos,

$$e^- \xrightarrow{B} e^- + \nu + \bar{\nu}$$

which is much weaker than the electromagnetic one, and where neutrinos of any flavours may be emitted. The Feynman diagram of this process is analogous to the one of pair annihilation, but it has an added kinematic threshold linked to the presence of the magnetic field. The final emissivity turns out to depend on B^2, so that the process suppressed as $B \to 0$.

The computation of the emissivities of these processes is done analogously to what outlined in Sec. 2.1 for the core cooling mechanisms. Going through these calculations is beyond the scope of this work, but as in the aforementioned cases the integration of the finite-temperature distribution functions over the phase space brings a steep dependence on T. In this work, the practical formulæ reviewed in Yakovlev et al. (2001) where employed, which in different regimes have power-law or even exponential dependencies on T. Moreover, as a general rule crustal neutrino processes are relevant above $T \approx 2 - 3 \times 10^9\,\mathrm{K}$. The profiles of the neutrino emissivity Q_ν for a representative case as used in the present version of `PARODY` is shown in Fig. A.1, with the four contribution in Fig. A.2.

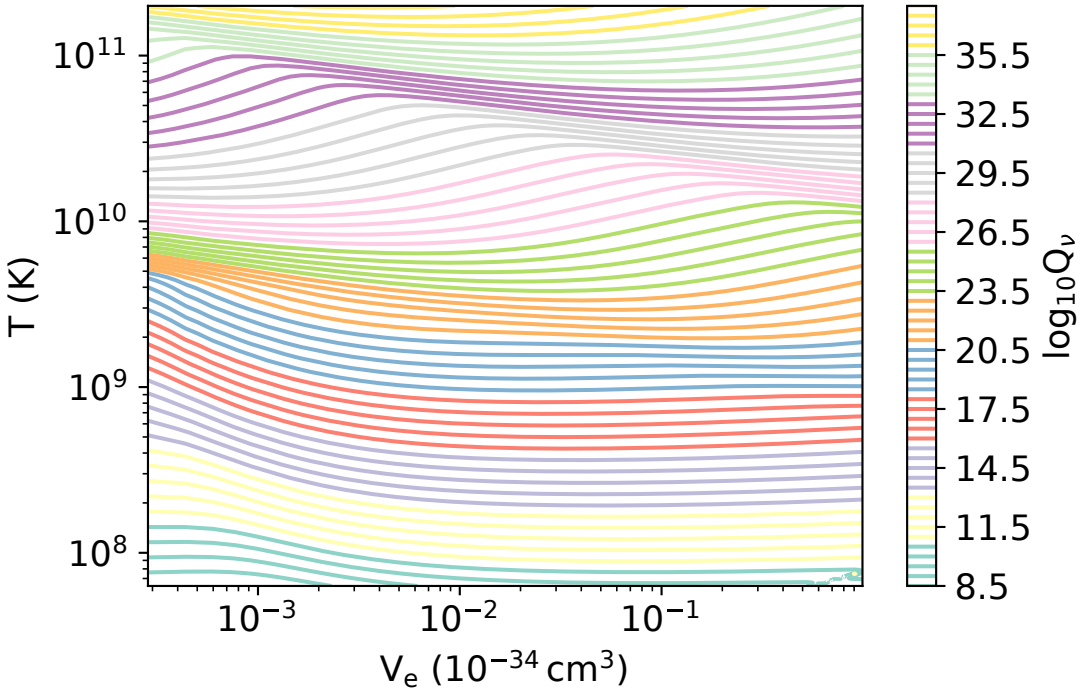

Figure A.1: Total neutrino emissivity as a function of the temperature and of the volume per electron $V_e = 1/n_e$ and for a constant $B = 10^{13}$ G.

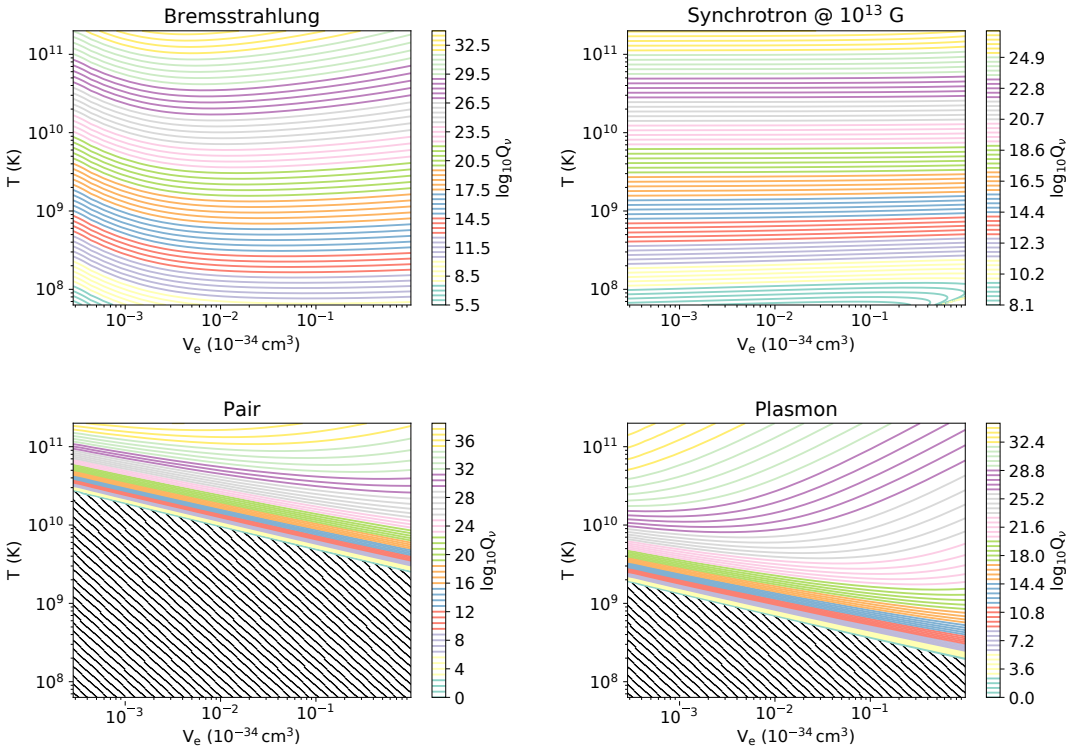

Figure A.2: The four separate contributions to neutrino emissivity. Note that two of them have a kinematic threshold.

APPENDIX B

Spherical harmonics

Spherical harmonics are special functions which are used in a wide range of applications. They form a set of orthogonal functions, from which an orthonormal basis for functions defined on a sphere can be built. Thus, they can be used as a 3D analogue of the sinusoidal functions used in the ordinary Fourier decomposition. They are defined as the eigenfunctions of the Laplace-Beltrami operator on the sphere Δ_S (i.e., the Laplace operator reduced to angular components)

$$\Delta_S = \frac{\partial}{\partial r}\left(r^2\frac{\partial}{\partial r}\right) - r^2\boldsymbol{\nabla}^2 = -\frac{1}{\sin\theta}\frac{\partial}{\partial\theta}\left(\sin\theta\frac{\partial}{\partial\theta}\right) - \frac{1}{\sin^2\theta}\frac{\partial^2}{\partial\phi^2}, \tag{B.1}$$

where $\boldsymbol{\nabla}^2$ is the ordinary Laplace operator. Then, the spherical harmonic of degree ℓ and order m satisfies

$$\Delta_S Y_\ell^m(\theta,\phi) = \ell(\ell+1)\, Y_\ell^m(\theta,\phi). \tag{B.2}$$

This is found to be given by

$$Y_\ell^m(\theta,\phi) = C_{\ell m} P_\ell^m(\cos\theta) e^{im\phi}, \tag{B.3}$$

where $C_{\ell m}$ is a normalisation coefficient and P_ℓ^m is the associated Legendre polynomial, defined as the solution of the Legendre equation

$$\frac{\mathrm{d}}{\mathrm{d}x}\left[(1-x^2)\frac{\mathrm{d}}{\mathrm{d}x}P_\ell^m(x)\right] + \left[\ell(\ell+1) - \frac{m^2}{1-x^2}\right]P_\ell^m(x) = 0. \tag{B.4}$$

Associated Legendre polynomials can be calculated through several recurrence properties, for example

$$\begin{cases} & P_0^0(x) = 1 \\ & P_1^0(x) = x \\ & P_1^1(x) = -\sqrt{1-x^2} \\ (\ell-m+1) & P_{\ell+1}^m(x) = (2\ell+1)xP_\ell^m(x) - (\ell+m)P_{\ell-1}^m(x) \quad \ell > 1 \\ \sqrt{1-x^2} & P_\ell^{m+1}(x) = (\ell-m)xP_\ell^m(x) - (\ell+m)P_{\ell-1}^m(x) \quad \ell > m > 1. \end{cases} \tag{B.5}$$

The normalisation coefficient can be chosen following several different conventions. In our case, the code uses the condition

$$\int_0^{2\pi}\int_0^{\pi} Y_\ell^m(\theta,\phi)Y_{\ell'}^{m'}(\theta,\phi)\sin\theta\,\mathrm{d}\theta\,\mathrm{d}\phi = 4\pi\delta_{\ell\ell'}\delta_{mm'} \tag{B.6}$$

where δ_{ij} is the Kronecker symbol (another popular convention is to normalise them to 1 rather than 4π); this sets

$$C_\ell^m = \sqrt{(2-\delta_{m0})(2\ell+1)\frac{(\ell-m)!}{(\ell+m)!}}. \tag{B.7}$$

As an example, the expressions for some of the first spherical harmonics are given in Tab. B.1, and visually represented in Fig. B.1.

Given a function $F(\theta,\phi)$ defined on the sphere, it is possible to write it as the series

$$F(\theta,\phi) = \sum_{\ell=0}^{+\infty}\sum_{m=0}^{\ell} f_\ell^m\, Y_\ell^m(\theta,\phi) \tag{B.8}$$

where the coefficient f_ℓ^m is given by

$$f_\ell^m = \int_0^{2\pi}\int_0^{\pi} Y_\ell^m(\theta,\phi)F(\theta,\phi)\sin\theta\,\mathrm{d}\theta\,\mathrm{d}\phi. \tag{B.9}$$

Note that we are taking the order in the interval $0 \le m \le \ell$, whereas in many cases it is taken to be $-\ell \le m \le \ell$; this is not restrictive, due to the parity relation

$$P_\ell^{-m}(x) = (-1)^m\frac{(\ell-m)!}{(\ell+m)!}\,P_\ell^m(x) \tag{B.10}$$

which allows to pass between the two forms if needed.

Spherical harmonics can be rotated in a simple fashion (e.g. Su and Coppens, 1994): if (α,β,γ) are the Euler angles describing the rotation $(\theta,\phi)\to(\theta',\phi')$, then a harmonic of degree ℓ is given by a linear combination of harmonics of the same degree,

$$Y_\ell^m(\theta',\phi') = \sum_{\mu=-\ell}^{\ell} D_{\mu m}^{(\ell)}(\alpha,\beta,\gamma)\,Y_\ell^\mu(\theta,\phi) \tag{B.11}$$

where the *Wigner matrices* are unitary matrices given by

$$D_{\mu m}^{(\ell)}(\alpha,\beta,\gamma) = e^{i\mu\alpha}d_{\mu m}^{(\ell)}(\beta)e^{-im\gamma} \tag{B.12}$$

having defined

$$d_{\mu m}^{(\ell)}(\beta) = \sqrt{\frac{(\ell+\mu)!\,(\ell+m)!}{(\ell-\mu)!\,(\ell-m)!}}(-1)^{\mu-m}\sum_k \binom{\ell+m}{k}\binom{\ell-m}{\ell-\mu-k}\left(\cos{}^{\beta}\!/_{2}\right)^{2\ell-\mu+m-2k}\left(\sin{}^{\beta}\!/_{2}\right)^{2k-m+\mu}$$
$$\max(0,m-\mu)\le k\le\min(\ell-\mu,\ell+m). \tag{B.13}$$

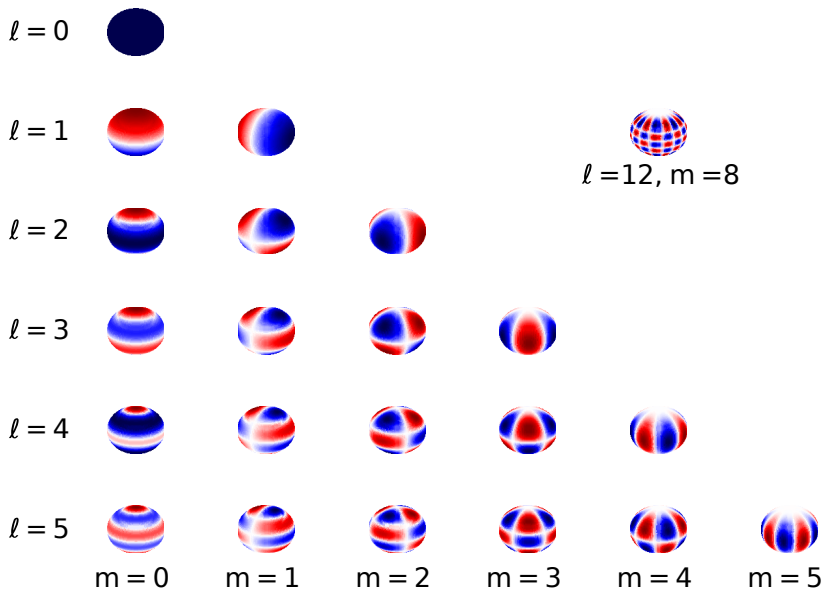

Figure B.1: Visualisation of the real part of the first spherical harmonics up to degree 5, with the addition of a higher order example ($\ell = 12$, $m = 8$). The harmonics with $m = 0$ are constant along the parallels of the sphere and are called *zonal*; those with $\ell = m$ are constant along meridians, and are called *sectorial*.

	$m = 0$	$m = 1$	$m = 2$	$m = 3$
$\ell = 0$	1			
$\ell = 1$	$\sqrt{3}\cos\theta$	$-\sqrt{3}\sin\theta\, e^{i\phi}$		
$\ell = 2$	$\frac{\sqrt{5}}{2}(3\cos^2\theta - 1)$	$-\sqrt{15}\cos\theta\sin\theta\, e^{i\phi}$	$\frac{\sqrt{15}}{2}\sin^2\theta\, e^{2i\phi}$	
$\ell = 3$	$\frac{\sqrt{7}}{2}(5\cos^3\theta - 3\cos\theta)$	$-\frac{\sqrt{42}}{4}(5\cos^2\theta - 1)\sin\theta\, e^{i\phi}$	$\frac{\sqrt{105}}{2}\sin^2\theta\cos\theta\, e^{2i\phi}$	$-\frac{\sqrt{70}}{4}\sin^3\theta\, e^{3i\phi}$

Table B.1: Expressions for the spherical harmonics up to the degree 3.

APPENDIX C

The Gauss-Legendre method

Quadrature methods, i.e. methods of numerical evaluations of integrals, come in many flavours, depending on the particular situation (whether an analytical expression for the function is at hand, the characteristics of the grid, etc.). Gaussian quadrature methods are based on the idea of evaluating the integral of a function $f(x)$ from the sum

$$\int_a^b W(x) f(x)\,\mathrm{d}x \simeq \sum_{i=1}^{n} w_i f(x_i) \tag{C.1}$$

where $W(x)$ is a known weight function and the points x_i and weights w_i are chosen to minimise the error. This expression is exact if $f(x)$ is a polynomial, so that the addition of the function $W(x)$ is critical when evaluating the integrals of function from which a polynomial can be factored out.

In particular, the `PARODY` code performs the integrals in $\mathrm{d}\theta$ such as Eq. B.5 using the so-called *Gauss-Legendre* method, for which

$$W(x) = 1 \qquad -1 < x < 1 \tag{C.2}$$

(these integration limits are just the one needed when integrating in $\mathrm{d}(\cos\theta)$, but any scaling would be possible), the grid is given by the n zeros of the n-th Legendre polynomial (Eq. B.5, see also Fig. C.1) and the weights are given by (e.g. Press et al., 1992)

$$w_i = \frac{2}{(1-x_i^2)[P_n'(x_i)^2]}. \tag{C.3}$$

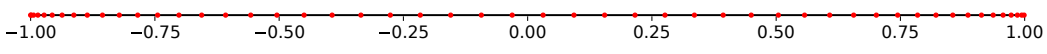

Figure C.1: Example of Gauss-Legendre grid-points for $n = 50$. Note that the points are symmetric with respect to 0.

APPENDIX D

Force-Free Fields

A plasma is in hydrostatic equilibrium when gas and magnetic pressure balance; in case gas pressure is itself negligible, the field must arrange itself in a self-balancing configuration, called a *force-free* field (Lüst and Schlüter, 1954). A field $\boldsymbol{B}$ is force free if it satisfies the relation

$$\boldsymbol{\nabla} \times \boldsymbol{B} = \alpha \boldsymbol{B} \tag{D.1}$$

for some function α which is constant along field lines. The simplest case of an overall constant α (*linear force-free field*) can be solved quite naturally in a spherical geometry by exploiting the properties of spherical harmonics with differential operators. This result was first derived by Chandrasekhar and Kendall (1957). They showed that the general solution can be written in terms of a function ψ (which got to be known as the *Chandrasekhar-Kendall function*) as

$$\boldsymbol{B} = \frac{1}{\alpha} \boldsymbol{\nabla} \times (\boldsymbol{\nabla} \times (\psi \, \hat{\boldsymbol{n}})) + \boldsymbol{\nabla} \times (\psi \, \hat{\boldsymbol{n}}) \tag{D.2}$$

where $\hat{\boldsymbol{n}}$ is a unit vector and ψ satisfies the Helmholtz equation

$$\nabla^2 \psi + \alpha^2 \psi = 0. \tag{D.3}$$

The solutions of the latter can be written in term of spherical harmonics Y_ℓ^m as

$$\psi_\ell^m = Z_\ell(\alpha r) \, Y_\ell^m; \quad Z_\ell = \left(\frac{\pi}{2 \alpha r} \right)^{1/2} \zeta_{\ell+1/2}(\alpha r) \tag{D.4}$$

where $\zeta_{\ell+1/2}$ is a linear combination of of Bessel functions $J_{\pm(\ell+1/2)}$.

Then, taking as the unit vector $\hat{n} = \hat{r}$ the field itself can be written as the sum of a poloidal and a toroidal part,

$$\boldsymbol{B}_\ell^m = \boldsymbol{P}_\ell^m + \boldsymbol{T}_\ell^m \tag{D.5}$$

where

$$\begin{aligned} \boldsymbol{P}_\ell^m &= \left[\frac{\ell(\ell+1)}{\alpha r} Z_\ell(\alpha r) \, Y_\ell^m \right] \hat{\boldsymbol{r}} + \left[\frac{1}{\alpha r} \frac{\mathrm{d}}{\mathrm{d}r} [r^2 Z_\ell(\alpha r)] \frac{\mathrm{d}}{\mathrm{d}\theta} Y_\ell^m \right] \hat{\boldsymbol{\theta}} + \left[\frac{m}{\alpha r \sin\theta} \frac{\mathrm{d}}{\mathrm{d}r} [r Z_\ell(\alpha r)] \frac{\mathrm{d}}{\mathrm{d}\phi} Y_\ell^m] \right] \hat{\boldsymbol{\phi}} \\ \boldsymbol{T}_\ell^m &= \left[\frac{m}{\sin\theta} Z_\ell(\alpha r) \frac{\mathrm{d}}{\mathrm{d}\phi} Y_\ell^m] \right] \hat{\boldsymbol{\theta}} - \left[Z_\ell(\alpha r) \frac{\mathrm{d}}{\mathrm{d}\theta} Y_\ell^m \right] \hat{\boldsymbol{\phi}}. \end{aligned} \tag{D.6}$$

Note that the sum of these two fields is force free, but they are not in general so by themselves.

Considering as an example the poloidal part of the dipole, the crust-confined field adapted to our configuration turns out to be

$$P_1^0 = B_0 \frac{R_\star^3 \alpha^2}{2\sqrt{3}} \left[y_0(\alpha R_\star)\, j_1(\alpha r) - j_0(\alpha R_\star)\, y_1(\alpha r) \right] \tag{D.7}$$

where the spherical Bessel functions of first and second kind j and y are defined as

$$j_\ell(x) = (x)^{-\ell} \left(\frac{1}{x} \frac{\mathrm{d}}{\mathrm{d}x} \right)^\ell \frac{\sin x}{x} \qquad y_\ell(x) = -(-x)^{-\ell} \left(\frac{1}{x} \frac{\mathrm{d}}{\mathrm{d}x} \right)^\ell \frac{\cos x}{x} \tag{D.8}$$

so that

$$\begin{aligned} j_0(x) &= \frac{\sin x}{x} & y_0(x) &= -\frac{\cos x}{x} \\ j_1(x) &= \frac{\sin x}{x^2} - \frac{\cos x}{x} & y_1(x) &= -\frac{\cos x}{x^2} - \frac{\sin x}{x}. \end{aligned} \tag{D.9}$$

The value of α is determined by the width of the crust, by means of the transcendent equation (Aguilera et al., 2008)

$$\tan[\alpha(r_c - R_\star)] = \alpha\, r_c \tag{D.10}$$

where r_c is the internal radius of the crust and $R_\star$ the external one.

Bibliography

Chapter 1

B. P. Abbott et al. Gravitational Waves and Gamma-Rays from a Binary Neutron Star Merger: GW170817 and GRB 170817A. ApJ, 848(2):L13, October 2017. doi: 10.3847/2041-8213/aa920c.

S. Abdollahi, F. Acero, M. Ackermann, M. Ajello, W. B. Atwood, M. Axelsson, L. Baldini, J. Ballet, G. Barbiellini, D. Bastieri, J. Becerra Gonzalez, R. Bellazzini, A. Berretta, E. Bissaldi, R. D. Blandford, E. D. Bloom, R. Bonino, E. Bottacini, T. J. Brandt, Bregeon, et al. Fermi Large Area Telescope Fourth Source Catalog. ApJS, 247(1):33, March 2020. doi: 10.3847/1538-4365/ab6bcb.

W. S. Adams. An a-type star of very low luminosity. *Publications of the Astronomical Society of the Pacific*, 26:198, oct 1914. doi: 10.1086/122337. URL `https://doi.org/10.1086/122337`.

Deborah N. Aguilera, Vincenzo Cirigliano, José A. Pons, Sanjay Reddy, and Rishi Sharma. Superfluid Heat Conduction and the Cooling of Magnetized Neutron Stars. Phys. Rev. Lett., 102(9):091101, March 2009. doi: 10.1103/PhysRevLett.102.091101.

J. Aleksić, S. Ansoldi, L.A. Antonelli, P. Antoranz, A. Babic, P. Bangale, M. Barceló, J.A. Barrio, J. Becerra González, W. Bednarek, E. Bernardini, B. Biasuzzi, A. Biland, M. Bitossi, O. Blanch, S. Bonnefoy, G. Bonnoli, F. Borracci, T. Bretz, E. Carmona, A. Carosi, R. Cecchi, P. Colin, E. Colombo, J.L. Contreras, D. Corti, J. Cortina, S. Covino, P. Da Vela, et al. The major upgrade of the magic telescopes, part ii: A performance study using observations of the crab nebula. *Astroparticle Physics*, 72:76–94, 2016. ISSN 0927-6505. doi: https://doi.org/10.1016/j.astropartphys.2015.02.005. URL `https://www.sciencedirect.com/science/article/pii/S0927650515000316`.

John Antoniadis, Paulo C. C. Freire, Norbert Wex, Thomas M. Tauris, Ryan S. Lynch, Marten H. van Kerkwijk, Michael Kramer, Cees Bassa, Vik S. Dhillon, Thomas Driebe, Jason W. T. Hessels, Victoria M. Kaspi, Vladislav I. Kondratiev, Norbert Langer, Thomas R. Marsh, Maura A. McLaughlin, Timothy T. Pennucci, Scott M. Ransom, Ingrid H. Stairs, Joeri van Leeuwen, Joris P. W. Verbiest, and David G. Whelan. A massive pulsar in a compact relativistic binary. *Science*, 340(6131):1233232, 2013. doi: 10.1126/science.1233232. URL `https://www.science.org/doi/abs/10.1126/science.1233232`.

W. Baade and F. Zwicky. Cosmic Rays from Super-novae. *Contributions from the Mount Wilson Observatory*, 3:79–83, January 1934.

C.A. Bertulani. *Nuclear Physics in a Nutshell*. In a Nutshell. Princeton University Press, 2007. ISBN 9780691125053. URL `https://books.google.it/books?id=I5nuAAAAMAAJ`.

A. J. Castro-Tirado, N. Østgaard, E. Göğüş, C. Sánchez-Gil, J. Pascual-Granado, V. Reglero, A. Mezentsev, M. Gabler, M. Marisaldi, T. Neubert, C. Budtz-Jørgensen, A. Lindanger, D. Sarria, I. Kuvvetli, P. Cerdá-Durán, J. Navarro-González, J. A. Font, B.-B. Zhang, N. Lund, et al. Very-high-frequency oscillations in the main peak of a magnetar giant flare. *Nature*, 600(7890):621–624, Dec 2021. ISSN 1476-4687. doi: 10.1038/s41586-021-04101-1. URL `https://doi.org/10.1038/s41586-021-04101-1`.

S. Chandrasekhar. The Maximum Mass of Ideal White Dwarfs. ApJ, 74:81, July 1931. doi: 10.1086/143324.

Francesco Coti Zelati, Nanda Rea, José A. Pons, Sergio Campana, and Paolo Esposito. Systematic study of magnetar outbursts. MNRAS, 474(1):961–1017, February 2018. doi: 10.1093/mnras/stx2679.

H. T. Cromartie, E. Fonseca, S. M. Ransom, P. B. Demorest, Z. Arzoumanian, H. Blumer, P. R. Brook, M. E. DeCesar, T. Dolch, J. A. Ellis, R. D. Ferdman, E. C. Ferrara, N. Garver-Daniels, P. A. Gentile, M. L. Jones, M. T. Lam, D. R. Lorimer, R. S. Lynch, M. A. McLaughlin, C. Ng, D. J. Nice, T. T. Pennucci, R. Spiewak, I. H. Stairs, K. Stovall, J. K. Swiggum, and W. W. Zhu. Relativistic shapiro delay measurements of an extremely massive millisecond pulsar. *Nature Astronomy*, 4(1):72–76, Jan 2020. ISSN 2397-3366. doi: 10.1038/s41550-019-0880-2. URL `https://doi.org/10.1038/s41550-019-0880-2`.

Davide De Grandis, Roberto Turolla, Toby S. Wood, Silvia Zane, Roberto Taverna, and Konstantinos N. Gourgouliatos. Three-dimensional Modeling of the Magnetothermal Evolution of Neutron Stars: Method and Test Cases. ApJ, 903(1):40, November 2020. doi: 10.3847/1538-4357/abb6f9.

Davide De Grandis, Roberto Taverna, Roberto Turolla, Andrea Gnarini, Sergei B. Popov, Silvia Zane, and Toby S. Wood. X-Ray Emission from Isolated Neutron Stars Revisited: 3D Magnetothermal Simulations. ApJ, 914(2):118, June 2021. doi: 10.3847/1538-4357/abfdac.

A. De Luca. Central compact objects in supernova remnants. In *Journal of Physics Conference Series*, volume 932 of *Journal of Physics Conference Series*, page 012006, December 2017. doi: 10.1088/1742-6596/932/1/012006.

R. H. Fowler. On Dense Matter. *Monthly Notices of the Royal Astronomical Society*, 87(2):114–122, 12 1926. ISSN 0035-8711. doi: 10.1093/mnras/87.2.114. URL `https://doi.org/10.1093/mnras/87.2.114`.

Keith Gendreau and Zaven Arzoumanian. Searching for a pulse. *Nature Astronomy*, 1(12):895–895, Dec 2017. ISSN 2397-3366. doi: 10.1038/s41550-017-0301-3. URL `https://doi.org/10.1038/s41550-017-0301-3`.

U. Geppert and H. J. Wiebicke. Amplification of neutron star magnetic fields by thermoelectric effects. I - General formalism. A&AS, 87(2):217–228, February 1991.

Ava Ghadimi and Marcos Santander. Searching for Sources of High Energy Neutrinos from Magnetars with IceCube. *arXiv e-prints*, art. arXiv:2107.08322, July 2021. Presented at the 37th International Cosmic Ray Conference (ICRC 2021). See `arXiv:2107.06966` for all IceCube contributions.

Riccardo Giacconi and Herbert Gursky. Observation of X-Ray Sources Outside the Solar System. Space Sci. Rev., 4(2):151–175, March 1965. doi: 10.1007/BF00173880.

T. Gold. Rotating Neutron Stars as the Origin of the Pulsating Radio Sources. Nature, 218 (5143):731–732, May 1968. doi: 10.1038/218731a0.

Konstantinos N. Gourgouliatos, Toby S. Wood, and Rainer Hollerbach. Magnetic field evolution in magnetar crusts through three-dimensional simulations. *Proceedings of the National Academy of Science*, 113(15):3944–3949, April 2016. doi: 10.1073/pnas.1522363113.

E. J. Groth. Timing of the Crab Pulsar III. The Slowing Down and the Nature of the Random Process. ApJS, 29:453–465, November 1975. doi: 10.1086/190354.

P. Haensel, A. Y. Potekhin, and D. G. Yakovlev. *Neutron Stars 1: Equation of State and Structure*, volume 326. 2007.

A. Hewish, S. J. Bell, J. D. H. Pilkington, P. F. Scott, and R. A. Collins. Observation of a Rapidly Pulsating Radio Source. Nature, 217(5130):709–713, February 1968. doi: 10.1038/217709a0.

G. Hobbs, A. Archibald, Z. Arzoumanian, D. Backer, M. Bailes, N. D. R. Bhat, M. Burgay, S. Burke-Spolaor, D. Champion, I. Cognard, W. Coles, J. Cordes, P. Demorest, G. Desvignes, R. D. Ferdman, L. Finn, P. Freire, M. Gonzalez, J. Hessels, A. Hotan, G. Janssen, F. Jenet, A. Jessner, C. Jordan, V. Kaspi, M. Kramer, V. Kondratiev, J. Lazio, K. Lazaridis, K. J. Lee, Y. Levin, A. Lommen, D. Lorimer, R. Lynch, A. Lyne, R. Manchester, M. McLaughlin, D. Nice, S. Oslowski, M. Pilia, A. Possenti, M. Purver, S. Ransom, J. Reynolds, S. Sanidas, J. Sarkissian, A. Sesana, R. Shannon, X. Siemens, I. Stairs, B. Stappers, D. Stinebring, G. Theureau, R. van Haasteren, W. van Straten, J. P. W. Verbiest, D. R. B. Yardley, and X. P. You. The International Pulsar Timing Array project: using pulsars as a gravitational wave detector. *Classical and Quantum Gravity*, 27(8):084013, April 2010. doi: 10.1088/0264-9381/27/8/084013.

Huanchen Hu, Michael Kramer, Norbert Wex, David J. Champion, and Marcel S. Kehl. Constraining the dense matter equation-of-state with radio pulsars. *Mon. Not. Roy. Astron. Soc.*, 497(3):3118–3130, 2020. doi: 10.1093/mnras/staa2107.

Alaa I. Ibrahim, Craig B. Markwardt, Jean H. Swank, Scott Ransom, Mallory Roberts, Victoria Kaspi, Peter M. Woods, Samar Safi-Harb, Solen Balman, William C. Parke, Chryssa Kouveliotou, Kevin Hurley, and Thomas Cline. Discovery of a Transient Magnetar: XTE J1810-197. ApJ, 609(1):L21–L24, July 2004. doi: 10.1086/422636.

Andrei P. Igoshev, Rainer Hollerbach, Toby Wood, and Konstantinos N. Gourgouliatos. Strong toroidal magnetic fields required by quiescent X-ray emission of magnetars. *Nature Astronomy*, October 2020. doi: 10.1038/s41550-020-01220-z.

Andrei P. Igoshev, Konstantinos N. Gourgouliatos, Rainer Hollerbach, and Toby S. Wood. 3D Magnetothermal Simulations of Tangled Crustal Magnetic Field in Central Compact Objects. ApJ, 909(2):101, March 2021. doi: 10.3847/1538-4357/abde3e.

G. L. Israel, P. Romano, V. Mangano, S. Dall'Osso, G. Chincarini, L. Stella, S. Campana, T. Belloni, G. Tagliaferri, A. J. Blustin, T. Sakamoto, K. Hurley, S. Zane, A. Moretti, D. Palmer, C. Guidorzi, D. N. Burrows, N. Gehrels, and H. A. Krimm. A Swift Gaze into the 2006 March 29 Burst Forest of SGR 1900+14. ApJ, 685(2):1114–1128, October 2008. doi: 10.1086/590486.

F. Jansen, Lumb, D., Altieri, B., Clavel, J., Ehle, M., Erd, C., Gabriel, C., Guainazzi, M., Gondoin, P., Much, R., Munoz, R., Santos, M., Schartel, N., Texier, D., and Vacanti, G.

Xmm-newton observatory* - i. the spacecraft and operations. *A&A*, 365(1):L1–L6, 2001. doi: 10.1051/0004-6361:20000036. URL https://doi.org/10.1051/0004-6361:20000036.

V. M. Kaspi. Magnetars. In Matthew Bailes, David J. Nice, and Stephen E. Thorsett, editors, *Radio Pulsars*, volume 302 of *Astronomical Society of the Pacific Conference Series*, page 151, January 2003.

Victoria M. Kaspi and Andrei M. Beloborodov. Magnetars. ARA&A, 55(1):261–301, August 2017. doi: 10.1146/annurev-astro-081915-023329.

M. Kramer, D.C. Backer, J.M. Cordes, T.J.W. Lazio, B.W. Stappers, and S. Johnston. Strong-field tests of gravity using pulsars and black holes. *New Astronomy Reviews*, 48(11):993–1002, 2004. ISSN 1387-6473. doi: https://doi.org/10.1016/j.newar.2004.09.020. URL https://www.sciencedirect.com/science/article/pii/S1387647304000909. Science with the Square Kilometre Array.

L. Landau. Origin of Stellar Energy. Nature, 141(3564):333–334, February 1938. doi: 10.1038/141333b0.

L. D. Landau. To the Stars theory. *Phys. Zs. Sowjet*, 1:285, December 1932.

Lev Davidovich Landau and E. M. Lifshitz. *Statistical physics. Pt.1.* 1969.

Lev Davidovich Landau and E. M. Lifshitz. *The classical theory of fields.* 1971.

R N Manchester. Pulsar glitches and their impact on neutron-star astrophysics, 2018.

R. N. Manchester, G. B. Hobbs, A. Teoh, and M. Hobbs. The Australia Telescope National Facility Pulsar Catalogue. AJ, 129(4):1993–2006, April 2005. doi: 10.1086/428488.

M. A. McLaughlin, A. G. Lyne, D. R. Lorimer, M. Kramer, A. J. Faulkner, R. N. Manchester, J. M. Cordes, F. Camilo, A. Possenti, I. H. Stairs, G. Hobbs, N. D'Amico, M. Burgay, and J. T. O'Brien. Transient radio bursts from rotating neutron stars. Nature, 439(7078):817–820, February 2006. doi: 10.1038/nature04440.

D. B. Melrose. Coherent emission mechanisms in astrophysical plasmas. *Reviews of Modern Plasma Physics*, 1(1):5, December 2017. doi: 10.1007/s41614-017-0007-0.

David W. Meltzer and Kip S. Thorne. Normal Modes of Radial Pulsation of Stars at the End Point of Thermonuclear Evolution. ApJ, 145:514, August 1966. doi: 10.1086/148792.

S. Mereghetti, V. Savchenko, D. Gotz, L. Ducci, C. Ferrigno, E. Bozzo, J. Borkowski, and A. Bazzano. SGR 1935+2154: INTEGRAL hard X-ray counterpart of radio burst. *GRB Coordinates Network*, 27668:1, April 2020.

J. H. Oort and Th. Walraven. Polarization and composition of the Crab nebula. Bull. Astron. Inst. Netherlands, 12:285, May 1956.

J. R. Oppenheimer and G. M. Volkoff. On Massive Neutron Cores. *Physical Review*, 55(4):374–381, February 1939. doi: 10.1103/PhysRev.55.374.

F. Pacini. Energy Emission from a Neutron Star. Nature, 216(5115):567–568, November 1967. doi: 10.1038/216567a0.

F. Pacini. Rotating Neutron Stars, Pulsars and Supernova Remnants. Nature, 219(5150):145–146, July 1968. doi: 10.1038/219145a0.

P. Padovani, F. Combes, M. Diaz Trigo, S. Ettori, E. Hatziminaoglou, P. Jonker, M. Salvato, S. Viti, C. Adami, J. Aird, D. Alexander, P. Casella, C. Ceccarelli, E. Churazov, M. Cirasuolo, E. Daddi, A. Edge, C. Feruglio, V. Mainieri, S. Markoff, A. Merloni, F. Nicastro, P. O'Brien, L. Oskinova, F. Panessa, E. Pointecouteau, A. Rau, J. Robrade, J. Schaye, F. Stoehr, L. Testi, and F. Tombesi. ESO-Athena Synergy White Paper. *arXiv e-prints*, art. arXiv:1705.06064, May 2017.

Alessandro Patruno and Anna L. Watts. Accreting Millisecond X-ray Pulsars. In Tomaso M. Belloni, Mariano Méndez, and Chengmin Zhang, editors, *Astrophysics and Space Science Library*, volume 461 of *Astrophysics and Space Science Library*, pages 143–208, January 2021. doi: 10.1007/978-3-662-62110-3_4.

E. Petroff, J. W. T. Hessels, and D. R. Lorimer. Fast radio bursts. A&A Rev., 27(1):4, May 2019. doi: 10.1007/s00159-019-0116-6.

José A. Pons and Daniele Viganò. Magnetic, thermal and rotational evolution of isolated neutron stars. *Living Reviews in Computational Astrophysics*, 5(1), Dec 2019. ISSN 2365-0524. doi: 10.1007/s41115-019-0006-7. URL `http://dx.doi.org/10.1007/s41115-019-0006-7`.

S. B. Popov, R. Turolla, and A. Possenti. A tale of two populations: rotating radio transients and X-ray dim isolated neutron stars. MNRAS, 369(1):L23–L26, June 2006. doi: 10.1111/j.1745-3933.2006.00166.x.

A. Y. Potekhin, V. F. Suleimanov, M. van Adelsberg, and K. Werner. Radiative properties of magnetic neutron stars with metallic surfaces and thin atmospheres. A&A, 546:A121, October 2012. doi: 10.1051/0004-6361/201219747.

D. G. Ravenhall, C. J. Pethick, and J. R. Wilson. Structure of matter below nuclear saturation density. *Phys. Rev. Lett.*, 50:2066–2069, Jun 1983. doi: 10.1103/PhysRevLett.50.2066. URL `https://link.aps.org/doi/10.1103/PhysRevLett.50.2066`.

Stuart L. Shapiro and Saul A. Teukolsky. *Black holes, white dwarfs, and neutron stars : the physics of compact objects*. 1983.

I. S. Shklovskii. *Akademiia Nauk SSSR Doklady*, 90:983, January 1953.

C. Thompson. Astrophysics of the Soft Gamma Repeaters and the Anomalous X-ray Pulsars. In Chryssa Kouveliotou, Joseph Ventura, and Ed van den Heuvel, editors, *The Neutron Star - Black Hole Connection*, volume 567, page 369, January 2001.

C. Thompson and R. C. Duncan. X-ray emission from neutron stars with supercritical magnetic fields: a model for the soft gamma repeaters. In M. Friedlander, N. Gehrels, and D. J. Macomb, editors, *Compton Gamma-ray Observatory*, volume 280 of *American Institute of Physics Conference Series*, pages 1085–1089, January 1993. doi: 10.1063/1.44179.

K. S. Thorne and A. N. Zytkow. Stars with degenerate neutron cores. I. Structure of equilibrium models. ApJ, 212:832–858, March 1977. doi: 10.1086/155109.

Richard C. Tolman. Static Solutions of Einstein's Field Equations for Spheres of Fluid. *Physical Review*, 55(4):364–373, February 1939. doi: 10.1103/PhysRev.55.364.

Sachiko Tsuruta and A. G. W. Cameron. Cooling and detectability of neutron stars. *Canadian Journal of Physics*, 44:1863, January 1966. doi: 10.1139/p66-156.

R. Turolla, S. Zane, and A. L. Watts. Magnetars: the physics behind observations. A review. *Reports on Progress in Physics*, 78(11):116901, November 2015. doi: 10.1088/0034-4885/78/11/116901.

Roberto Turolla. *Isolated Neutron Stars: The Challenge of Simplicity*, volume 357 of *Astrophysics and Space Science Library*, page 141. Springer, 2009. doi: 10.1007/978-3-540-76965-1_7.

V. A. Urpin and D. G. Yakovlev. Thermogalvanomagnetic Effects in White Dwarfs and Neutron Stars. Soviet Ast., 24:425, Aug 1980.

E. P. J. van den Heuvel, G. Bélanger, L. Hanlon, and E. Kuulkers. Fifteen-plus years of integral science. *New Astronomy Reviews*, 93:101633, 2021. ISSN 1387-6473. doi: https://doi.org/10.1016/j.newar.2021.101633. URL `https://www.sciencedirect.com/science/article/pii/S1387647321000208`.

Daniele Viganò. *Magnetic fields in neutron stars*. PhD thesis, University of Alicante, September 2013.

M. C. Weisskopf, B. Brinkman, C. Canizares, G. Garmire, S. Murray, and L. P. Van Speybroeck. An Overview of the Performance and Scientific Results from the Chandra X-Ray Observatory. PASP, 114(791):1–24, January 2002. doi: 10.1086/338108.

Martin C. Weisskopf, Brian Ramsey, Stephen O'Dell, Allyn Tennant, Ronald Elsner, Paolo Soffitta, Ronaldo Bellazzini, Enrico Costa, Jeffrey Kolodziejczak, Victoria Kaspi, Fabio Muleri, Herman Marshall, Giorgio Matt, and Roger Romani. The Imaging X-ray Polarimetry Explorer (IXPE). In Jan-Willem A. den Herder, Tadayuki Takahashi, and Marshall Bautz, editors, *Space Telescopes and Instrumentation 2016: Ultraviolet to Gamma Ray*, volume 9905 of *Society of Photo-Optical Instrumentation Engineers (SPIE) Conference Series*, page 990517, July 2016. doi: 10.1117/12.2235240.

John Archibald Wheeler. Superdense Stars. ARA&A, 4:393, January 1966. doi: 10.1146/annurev.aa.04.090166.002141.

T. S. Wood, R. Hollerbach, and M. Lyutikov. Density-shear instability in electron magnetohydrodynamics. *Physics of Plasmas*, 21(5):052110, May 2014. doi: 10.1063/1.4879810.

Dmitrii G. Yakovlev, Pawel Haensel, Gordon Baym, and Christopher Pethick. Lev Landau and the concept of neutron stars. *Physics Uspekhi*, 56(3):289-295, March 2013. doi: 10.3367/UFNe.0183.201303f.0307.

Chapter 2

M. V. Beznogov, A. Y. Potekhin, and D. G. Yakovlev. Diffusive heat blanketing envelopes of neutron stars. MNRAS, 459(2):1569–1579, June 2016. doi: 10.1093/mnras/stw751.

M. V. Beznogov, A. Y. Potekhin, and D. G. Yakovlev. Heat blanketing envelopes of neutron stars. Phys. Rep., 919:1–68, July 2021. doi: 10.1016/j.physrep.2021.03.004.

L. Biermann. Über den Ursprung der Magnetfelder auf Sternen und im interstellaren Raum (miteinem Anhang von A. Schlüter). *Zeitschrift Naturforschung Teil A*, 5:65, January 1950. (in German).

G. Gamow and M. Schoenberg. The Possible Role of Neutrinos in Stellar Evolution. *Physical Review*, 58(12):1117–1117, December 1940. doi: 10.1103/PhysRev.58.1117.

U. Geppert and H. J. Wiebicke. Amplification of neutron star magnetic fields by thermoelectric effects. I - General formalism. A&AS, 87(2):217–228, February 1991.

Nickolay Y. Gnedin, Andrea Ferrara, and Ellen G. Zweibel. Generation of the Primordial Magnetic Fields during Cosmological Reionization. ApJ, 539(2):505–516, August 2000. doi: 10.1086/309272.

Peter Goldreich and Andreas Reisenegger. Magnetic Field Decay in Isolated Neutron Stars. ApJ, 395:250, August 1992. doi: 10.1086/171646.

E. H. Gudmundsson, C. J. Pethick, and R. I. Epstein. Structure of neutron star envelopes. ApJ, 272:286–300, September 1983. doi: 10.1086/161292.

James M. Lattimer, C. J. Pethick, Madappa Prakash, and Pawel Haensel. Direct URCA process in neutron stars. Phys. Rev. Lett., 66(21):2701–2704, May 1991. doi: 10.1103/PhysRevLett.66.2701.

J. A. Pons and U. Geppert. Magnetic field dissipation in neutron star crusts: from magnetars to isolated neutron stars. A&A, 470(1):303–315, Jul 2007. doi: 10.1051/0004-6361:20077456.

A. Y. Potekhin and D. G. Yakovlev. Thermal structure and cooling of neutron stars with magnetized envelopes. *A&A*, 374(1):213–226, 2001. doi: 10.1051/0004-6361:20010698.

A. Y. Potekhin, J. A. Pons, and D. Page. Neutron Stars–Cooling and Transport. *Space Science Reviews*, 191:239–291, October 2015.

Christopher Prior and Konstantinos N. Gourgouliatos. Observational signatures of magnetic field structure in relativistic AGN jets. A&A, 622:A122, February 2019. doi: 10.1051/0004-6361/201834469.

Stuart L. Shapiro and Saul A. Teukolsky. *Black holes, white dwarfs, and neutron stars : the physics of compact objects*. 1983.

Sachiko Tsuruta and A. G. W. Cameron. Cooling and detectability of neutron stars. *Canadian Journal of Physics*, 44:1863, January 1966. doi: 10.1139/p66-156.

V. A. Urpin and D. G. Yakovlev. Thermogalvanomagnetic Effects in White Dwarfs and Neutron Stars. Soviet Ast., 24:425, Aug 1980.

D. G. Yakovlev, A. D. Kaminker, O. Y. Gnedin, and P. Haensel. Neutrino emission from neutron stars. Phys. Rep., 354(1-2):1–155, November 2001. doi: 10.1016/S0370-1573(00)00131-9.

J.M. Ziman. *Principles of the Theory of Solids*. Cambridge University Press, 1972. ISBN 9780521297332. URL `https://books.google.it/books?id=o4woMNO-C3sC`.

Chapter 3

P. W. Anderson and N. Itoh. Pulsar glitches and restlessness as a hard superfluidity phenomenon. *Nature*, 256(5512):25–27, Jul 1975. ISSN 1476-4687. doi: 10.1038/256025a0. URL https://doi.org/10.1038/256025a0.

Julien Aubert, Jonathan Aurnou, and Johannes Wicht. The magnetic structure of convection-driven numerical dynamos. *Geophysical Journal International*, 172(3):945–956, Mar 2008. doi: 10.1111/j.1365-246X.2007.03693.x.

C. Canuto. *Spectral Methods in Fluid Dynamics*. Computational Physics Series. Springer-Verlag, 1988. ISBN 9783540522058. URL https://books.google.it/books?id=2TbvAAAAMAAJ.

R. Ciolfi and L. Rezzolla. Twisted-torus configurations with large toroidal magnetic fields in relativistic stars. MNRAS, 435:L43–L47, August 2013. doi: 10.1093/mnrasl/slt092.

Andrew Cumming, Phil Arras, and Ellen Zweibel. Magnetic Field Evolution in Neutron Star Crusts Due to the Hall Effect and Ohmic Decay. ApJ, 609(2):999–1017, July 2004. doi: 10.1086/421324.

Davide De Grandis, Roberto Turolla, Toby S. Wood, Silvia Zane, Roberto Taverna, and Konstantinos N. Gourgouliatos. Three-dimensional Modeling of the Magnetothermal Evolution of Neutron Stars: Method and Test Cases. ApJ, 903(1):40, November 2020. doi: 10.3847/1538-4357/abb6f9.

E. Dormy. *Modelisation numerique de la dynamo terrestre*. PhD thesis, Institut de Physique du Globe de Paris, November 1997. URL http://www.math.ens.fr/~dormy/these/index.html. (in French).

Emmanuel Dormy, Philippe Cardin, and Dominique Jault. MHD flow in a slightly differentially rotating spherical shell, with conducting inner core, in a dipolar magnetic field. *Earth and Planetary Science Letters*, 160(1-2):15–30, July 1998. doi: 10.1016/S0012-821X(98)00078-8.

K. N. Gourgouliatos and José A. Pons. Nonaxisymmetric Hall instability: A key to understanding magnetars. *Physical Review Research*, 1(3):032049, December 2019. doi: 10.1103/PhysRevResearch.1.032049.

Konstantinos N. Gourgouliatos and Rainer Hollerbach. Magnetic Axis Drift and Magnetic Spot Formation in Neutron Stars with Toroidal Fields. ApJ, 852(1):21, January 2018. doi: 10.3847/1538-4357/aa9d93.

Konstantinos N. Gourgouliatos, Toby S. Wood, and Rainer Hollerbach. Magnetic field evolution in magnetar crusts through three-dimensional simulations. *Proceedings of the National Academy of Science*, 113(15):3944–3949, April 2016. doi: 10.1073/pnas.1522363113.

Konstantinos N. Gourgouliatos, Rainer Hollerbach, and Andrei P. Igoshev. Powering central compact objects with a tangled crustal magnetic field. MNRAS, 495(2):1692–1699, June 2020. doi: 10.1093/mnras/staa1295.

Wynn C. G. Ho, Nils Andersson, and Vanessa Graber. Dynamical onset of superconductivity and retention of magnetic fields in cooling neutron stars. *Physical Review C*, 96(6), Dec 2017. ISSN 2469-9993. doi: 10.1103/physrevc.96.065801. URL http://dx.doi.org/10.1103/PhysRevC.96.065801.

Rainer Hollerbach and Günther Rüdiger. Hall drift in the stratified crusts of neutron stars. MNRAS, 347(4):1273–1278, February 2004. doi: 10.1111/j.1365-2966.2004.07307.x.

Andrei P. Igoshev, Rainer Hollerbach, Toby Wood, and Konstantinos N. Gourgouliatos. Strong toroidal magnetic fields required by quiescent X-ray emission of magnetars. *Nature Astronomy*, October 2020. doi: 10.1038/s41550-020-01220-z.

S. K. Lander and K. N. Gourgouliatos. Magnetic-field evolution in a plastically failing neutron-star crust. MNRAS, 486(3):4130–4143, Jul 2019. doi: 10.1093/mnras/stz1042.

K. P. Levenfish and D. G. Yakovlev. Standard and enhanced cooling of neutron stars with superfluid cores. *Astronomy Letters*, 22(1):49–57, January 1996.

Dany Page and E. Baron. Strangeness, Condensation, Nucleon Superfluidity, and Cooling of Neutron Stars. ApJ, 354:L17, May 1990. doi: 10.1086/185712.

Dany Page, James M. Lattimer, Madappa Prakash, and Andrew W. Steiner. Minimal Cooling of Neutron Stars: A New Paradigm. ApJS, 155(2):623–650, December 2004. doi: 10.1086/424844.

Dany Page, Ulrich Geppert, and Fridolin Weber. The cooling of compact stars. Nucl. Phys. A, 777:497–530, October 2006. doi: 10.1016/j.nuclphysa.2005.09.019.

Dany Page, Madappa Prakash, James M. Lattimer, and Andrew W. Steiner. Rapid cooling of the neutron star in cassiopeia a triggered by neutron superfluidity in dense matter. *Phys. Rev. Lett.*, 106:081101, Feb 2011. doi: 10.1103/PhysRevLett.106.081101. URL `https://link.aps.org/doi/10.1103/PhysRevLett.106.081101`.

R. A. Phinney and R. Burridge. Representation of the elastic - gravitational excitation of a spherical earth model by generalized spherical harmonics. *Geophysical Journal*, 34:451–487, December 1973. doi: 10.1111/j.1365-246X.1973.tb02407.x.

J. A. Pons, J. A. Miralles, and U. Geppert. Magneto-thermal evolution of neutron stars. A&A, 496(1):207–216, Mar 2009. doi: 10.1051/0004-6361:200811229.

José A. Pons and Daniele Viganò. Magnetic, thermal and rotational evolution of isolated neutron stars. *Living Reviews in Computational Astrophysics*, 5(1), Dec 2019. ISSN 2365-0524. doi: 10.1007/s41115-019-0006-7. URL `http://dx.doi.org/10.1007/s41115-019-0006-7`.

S. B. Popov, R. Taverna, and R. Turolla. Probing the surface magnetic field structure in RX J1856.5-3754. MNRAS, 464(4):4390–4398, February 2017. doi: 10.1093/mnras/stw2681.

A. Y. Potekhin, J. A. Pons, and D. Page. Neutron Stars–Cooling and Transport. *Space Science Reviews*, 191:239–291, October 2015.

R. Taverna, R. Turolla, D. Gonzalez Caniulef, S. Zane, F. Muleri, and P. Soffitta. Polarization of neutron star surface emission: a systematic analysis. MNRAS, 454(3):3254–3266, December 2015. doi: 10.1093/mnras/stv2168.

Kip S. Thorne. Multipole expansions of gravitational radiation. *Reviews of Modern Physics*, 52 (2):299–340, April 1980. doi: 10.1103/RevModPhys.52.299.

S. Tsuruta and A. Cameron. Cooling and detectability of neutron stars. *Canadian Journal of Physics - CAN J PHYS*, 44, 08 1966a. doi: 10.1139/p66-156.

Sachiko Tsuruta and A. G. W. Cameron. Cooling and detectability of neutron stars. *Canadian Journal of Physics*, 44:1863, January 1966b. doi: 10.1139/p66-156.

D. Viganò, N. Rea, J. A. Pons, R. Perna, D. N. Aguilera, and J. A. Miralles. Unifying the observational diversity of isolated neutron stars via magneto-thermal evolution models. MNRAS, 434(1):123–141, September 2013. doi: 10.1093/mnras/stt1008.

Daniele Viganò. *Magnetic fields in neutron stars*. PhD thesis, University of Alicante, September 2013.

T. S. Wood and R. Hollerbach. Three Dimensional Simulation of the Magnetic Stress in a Neutron Star Crust. Phys. Rev. Lett., 114(19):191101, May 2015. doi: 10.1103/PhysRevLett.114.191101.

D. G. Yakovlev and V. A. Urpin. The Cooling of Neutron Stars and the Nature of Superdense Matter. *Soviet Astronomy Letters*, 7:88, February 1981.

Silvia Zane and Roberto Turolla. Unveiling the thermal and magnetic map of neutron star surfaces though their X-ray emission: method and light-curve analysis. MNRAS, 366(3):727–738, March 2006. doi: 10.1111/j.1365-2966.2005.09784.x.

Chapter 4

D. N. Aguilera, J. A. Pons, and J. A. Miralles. 2D Cooling of magnetized neutron stars. A&A, 486(1):255–271, July 2008. doi: 10.1051/0004-6361:20078786.

A. I. Chugunov and C. J. Horowitz. Breaking stress of neutron star crust. MNRAS, 407(1): L54–L58, Sep 2010. doi: 10.1111/j.1745-3933.2010.00903.x.

J. S. Clark, B. W. Ritchie, F. Najarro, N. Langer, and I. Negueruela. A VLT/FLAMES survey for massive binaries in Westerlund 1. IV. Wd1-5 - binary product and a pre-supernova companion for the magnetar CXOU J1647-45? A&A, 565:A90, May 2014. doi: 10.1051/0004-6361/201321771.

Davide De Grandis, Roberto Turolla, Toby S. Wood, Silvia Zane, Roberto Taverna, and Konstantinos N. Gourgouliatos. Three-dimensional Modeling of the Magnetothermal Evolution of Neutron Stars: Method and Test Cases. ApJ, 903(1):40, November 2020. doi: 10.3847/1538-4357/abb6f9.

Davide De Grandis, Roberto Taverna, Roberto Turolla, Andrea Gnarini, Sergei B. Popov, Silvia Zane, and Toby S. Wood. X-Ray Emission from Isolated Neutron Stars Revisited: 3D Magnetothermal Simulations. ApJ, 914(2):118, June 2021. doi: 10.3847/1538-4357/abfdac.

C. P. de Vries, J. Vink, M. Méndez, and F. Verbunt. Long-term variability in the X-ray emission of RX J0720.4-3125. A&A, 415:L31–L34, February 2004. doi: 10.1051/0004-6361:20040009.

Robert C. Duncan and Christopher Thompson. Formation of Very Strongly Magnetized Neutron Stars: Implications for Gamma-Ray Bursts. ApJ, 392:L9, June 1992. doi: 10.1086/186413.

Lilia Ferrario and Dayal Wickramasinghe. Origin and evolution of magnetars. MNRAS, 389(1): L66–L70, September 2008. doi: 10.1111/j.1745-3933.2008.00527.x.

U. Geppert, M. Küker, and D. Page. Temperature distribution in magnetized neutron star crusts. II. The effect of a strong toroidal component. A&A, 457(3):937–947, October 2006. doi: 10.1051/0004-6361:20054696.

Peter Goldreich and Andreas Reisenegger. Magnetic Field Decay in Isolated Neutron Stars. ApJ, 395:250, August 1992. doi: 10.1086/171646.

Konstantinos N. Gourgouliatos and Andrew Cumming. Hall Attractor in Axially Symmetric Magnetic Fields in Neutron Star Crusts. Phys. Rev. Lett., 112(17):171101, May 2014. doi: 10.1103/PhysRevLett.112.171101.

Konstantinos N. Gourgouliatos and Rainer Hollerbach. Magnetic Axis Drift and Magnetic Spot Formation in Neutron Stars with Toroidal Fields. ApJ, 852(1):21, January 2018. doi: 10.3847/1538-4357/aa9d93.

Konstantinos N. Gourgouliatos and José A. Pons. Nonaxisymmetric Hall instability: A key to understanding magnetars. *arXiv e-prints*, art. arXiv:2001.03335, Jan 2020.

Konstantinos N. Gourgouliatos, Rainer Hollerbach, and Andrei P. Igoshev. Powering central compact objects with a tangled crustal magnetic field. MNRAS, 495(2):1692–1699, June 2020. doi: 10.1093/mnras/staa1295.

G. Greenstein and G. J. Hartke. Pulselike character of blackbody radiation from neutron stars. ApJ, 271:283–293, August 1983. doi: 10.1086/161195.

F. Haberl, A. D. Schwope, V. Hambaryan, G. Hasinger, and C. Motch. A broad absorption feature in the X-ray spectrum of the isolated neutron star RBS1223 (1RXS J130848.6+212708). A&A, 403:L19–L23, May 2003. doi: 10.1051/0004-6361:20030450.

F. Haberl, C. Motch, V. E. Zavlin, K. Reinsch, B. T. Gänsicke, M. Cropper, A. D. Schwope, R. Turolla, and S. Zane. The isolated neutron star X-ray pulsars RX J0420.0-5022 and RX J0806.4-4123: New X-ray and optical observations. A&A, 424:635–645, September 2004. doi: 10.1051/0004-6361:20040440.

F. Haberl, R. Sturm, M. D. Filipović, W. Pietsch, and E. J. Crawford. SXP 1062, a young Be X-ray binary pulsar with long spin period. Implications for the neutron star birth spin. A&A, 537:L1, January 2012. doi: 10.1051/0004-6361/201118369.

B. Haskell. Mountains on neutron stars. *Classical and Quantum Gravity*, 25(11):114049, June 2008. doi: 10.1088/0264-9381/25/11/114049.

Wynn C. G. Ho, David L. Kaplan, Philip Chang, Matthew van Adelsberg, and Alexander Y. Potekhin. Magnetic hydrogen atmosphere models and the neutron star RX J1856.5-3754. MNRAS, 375(3):821–830, March 2007. doi: 10.1111/j.1365-2966.2006.11376.x.

C. J. Horowitz, D. K. Berry, and E. F. Brown. Phase separation in the crust of accreting neutron stars. Phys. Rev. E, 75(6):066101, June 2007. doi: 10.1103/PhysRevE.75.066101.

Andrei P. Igoshev, Rainer Hollerbach, Toby Wood, and Konstantinos N. Gourgouliatos. Strong toroidal magnetic fields required by quiescent X-ray emission of magnetars. *Nature Astronomy*, October 2020. doi: 10.1038/s41550-020-01220-z.

Andrei P. Igoshev, Konstantinos N. Gourgouliatos, Rainer Hollerbach, and Toby S. Wood. 3D Magnetothermal Simulations of Tangled Crustal Magnetic Field in Central Compact Objects. ApJ, 909(2):101, March 2021. doi: 10.3847/1538-4357/abde3e.

Keith Jahoda, Henric Krawczynski, Fabian Kislat, Herman Marshall, and Takashi Okajima. The X-ray Polarization Probe mission concept. In *Bulletin of the American Astronomical Society*, volume 51, page 181, September 2019.

P. B. Jones. Nature of Fault Planes in Solid Neutron Star Matter. ApJ, 595(1):342–345, September 2003. doi: 10.1086/377351.

Ilya A. Kondratyev, Sergey G. Moiseenko, Gennady S. Bisnovatyi-Kogan, and Maria V. Glushikhina. Three-dimensional heat transfer effects in external layers of a magnetized neutron star. MNRAS, 497(3):2883–2892, September 2020. doi: 10.1093/mnras/staa2154.

S. K. Lander. Magnetic Fields in Superconducting Neutron Stars. Phys. Rev. Lett., 110(7): 071101, February 2013. doi: 10.1103/PhysRevLett.110.071101.

S. K. Lander. Generating neutron-star magnetic fields: three dynamo phases. MNRAS, 507(1): L36–L40, October 2021. doi: 10.1093/mnrasl/slab086.

S. K. Lander and K. N. Gourgouliatos. Magnetic-field evolution in a plastically failing neutron-star crust. MNRAS, 486(3):4130–4143, Jul 2019. doi: 10.1093/mnras/stz1042.

V. M. Malofeev, O. I. Malov, and D. A. Teplykh. Radio emission from AXP and XDINS. Ap&SS, 308(1-4):211–216, April 2007. doi: 10.1007/s10509-007-9341-y.

R. P. Mignani, D. Vande Putte, M. Cropper, R. Turolla, S. Zane, L. J. Pellizza, L. A. Bignone, N. Sartore, and A. Treves. The birthplace and age of the isolated neutron star RX J1856.5-3754. MNRAS, 429(4):3517–3521, March 2013. doi: 10.1093/mnras/sts627.

R. P. Mignani, V. Testa, D. González Caniulef, R. Taverna, R. Turolla, S. Zane, and K. Wu. Evidence for vacuum birefringence from the first optical-polarimetry measurement of the isolated neutron star RX J1856.5-3754. MNRAS, 465(1):492–500, February 2017. doi: 10.1093/mnras/stw2798.

S. A. Olausen and V. M. Kaspi. The McGill Magnetar Catalog. ApJS, 212(1):6, May 2014. doi: 10.1088/0067-0049/212/1/6.

Dany Page. Thermal Radiation from Magnetized Neutron Stars. A Look at the Surface of a Neutron Star. Space Sci. Rev., 74(3-4):437–446, November 1995. doi: 10.1007/BF00751430.

Dany Page and A. Sarmiento. Surface Temperature of a Magnetized Neutron Star and Interpretation of the ROSAT Data. II. ApJ, 473:1067, December 1996. doi: 10.1086/178216.

Dany Page, Ulrich Geppert, and Manfred Küker. Cooling of neutron stars with strong toroidal magnetic fields. Ap&SS, 308(1-4):403–412, April 2007. doi: 10.1007/s10509-007-9316-z.

Rosalba Perna and Jose A. Pons. A Unified Model of the Magnetar and Radio Pulsar Bursting Phenomenology. ApJ, 727(2):L51, February 2011. doi: 10.1088/2041-8205/727/2/L51.

Rosalba Perna, Daniele Viganò, José A. Pons, and Nanda Rea. The imprint of the crustal magnetic field on the thermal spectra and pulse profiles of isolated neutron stars. MNRAS, 434(3):2362–2372, September 2013. doi: 10.1093/mnras/stt1181.

J. A. Pons and N. Rea. Modeling Magnetar Outbursts: Flux Enhancements and the Connection with Short Bursts and Glitches. ApJ, 750(1):L6, May 2012. doi: 10.1088/2041-8205/750/1/L6.

S. B. Popov, R. Taverna, and R. Turolla. Probing the surface magnetic field structure in RX J1856.5-3754. MNRAS, 464(4):4390–4398, February 2017. doi: 10.1093/mnras/stw2681.

A. Y. Potekhin and D. G. Yakovlev. Thermal structure and cooling of neutron stars with magnetized envelopes. *A&A*, 374(1):213–226, 2001. doi: 10.1051/0004-6361:20010698.

N. Rea, G. L. Israel, P. Esposito, J. A. Pons, A. Camero-Arranz, R. P. Mignani, R. Turolla, S. Zane, M. Burgay, A. Possenti, S. Campana, T. Enoto, N. Gehrels, E. Göğüş, D. Götz, C. Kouveliotou, K. Makishima, S. Mereghetti, S. R. Oates, D. M. Palmer, R. Perna, L. Stella, and A. Tiengo. A New Low Magnetic Field Magnetar: The 2011 Outburst of Swift J1822.3-1606. ApJ, 754(1):27, July 2012. doi: 10.1088/0004-637X/754/1/27.

A. Reboul-Salze, J. Guilet, R. Raynaud, and M. Bugli. A global model of the magnetorotational instability in protoneutron stars. A&A, 645:A109, January 2021. doi: 10.1051/0004-6361/202038369.

Andreas Reisenegger. Origin and evolution of neutron star magnetic fields. *arXiv e-prints*, art. astro-ph/0307133, July 2003.

Michela Rigoselli, Sandro Mereghetti, and Caterina Tresoldi. Candidate isolated neutron stars in the 4XMM-DR10 catalog of X-ray sources. MNRAS, October 2021. doi: 10.1093/mnras/stab2974.

G. Rüdiger, R. Hollerbach, and L.L. Kitchatinov. *Magnetic Processes in Astrophysics: Theory, Simulations, Experiments*. Wiley, 2013. ISBN 9783527648948. URL `https://books.google.it/books?id=M6VMAgAAQBAJ`.

N. Sartore, A. Tiengo, S. Mereghetti, A. De Luca, R. Turolla, and F. Haberl. Spectral monitoring of RX J1856.5-3754 with XMM-Newton. Analysis of EPIC-pn data. A&A, 541:A66, May 2012. doi: 10.1051/0004-6361/201118489.

A. A. Schekochihin, S. C. Cowley, W. Dorland, G. W. Hammett, G. G. Howes, E. Quataert, and T. Tatsuno. Astrophysical Gyrokinetics: Kinetic and Fluid Turbulent Cascades in Magnetized Weakly Collisional Plasmas. ApJS, 182(1):310–377, May 2009. doi: 10.1088/0067-0049/182/1/310.

Anatoly Spitkovsky. Force-free Pulsar Magnetospheres: Axisymmetric and Oblique Rotators. ApJ, 648(1):L51–L54, September 2006. doi: 10.1086/507518.

N. Tetzlaff, T. Eisenbeiss, R. Neuhäuser, and M. M. Hohle. The origin of RX J1856.5-3754 and RX J0720.4-3125 - updated using new parallax measurements. MNRAS, 417(1):617–626, October 2011. doi: 10.1111/j.1365-2966.2011.19302.x.

Andrea Tiengo and Sandro Mereghetti. XMM-Newton Discovery of 7 s Pulsations in the Isolated Neutron Star RX J1856.5-3754. ApJ, 657(2):L101–L104, March 2007. doi: 10.1086/513143.

R. Turolla, S. Zane, J. A. Pons, P. Esposito, and N. Rea. Is SGR 0418+5729 Indeed a Waning Magnetar? *ApJ*, 740:105, October 2011. doi: 10.1088/0004-637X/740/2/105.

Roberto Turolla. *Isolated Neutron Stars: The Challenge of Simplicity*, volume 357 of *Astrophysics and Space Science Library*, page 141. Springer, 2009. doi: 10.1007/978-3-540-76965-1_7.

M. H. van Kerkwijk and D. L. Kaplan. Timing the Nearby Isolated Neutron Star RX J1856.5-3754. ApJ, 673(2):L163, February 2008. doi: 10.1086/528796.

M. H. van Kerkwijk, D. L. Kaplan, M. Durant, S. R. Kulkarni, and F. Paerels. A Strong, Broad Absorption Feature in the X-Ray Spectrum of the Nearby Neutron Star RX J1605.3+3249. ApJ, 608(1):432–443, June 2004. doi: 10.1086/386299.

Daniele Viganò. *Magnetic fields in neutron stars*. PhD thesis, University of Alicante, September 2013.

F. M. Walter, T. Eisenbeiß, J. M. Lattimer, B. Kim, V. Hambaryan, and R. Neuhäuser. Revisiting the Parallax of the Isolated Neutron Star RX J185635-3754 Using HST/ACS Imaging. ApJ, 724(1):669–677, November 2010. doi: 10.1088/0004-637X/724/1/669.

Frederick M. Walter, Scott J. Wolk, and Ralph Neuhäuser. Discovery of a nearby isolated neutron star. Nature, 379(6562):233–235, January 1996. doi: 10.1038/379233a0.

L. Woltjer. X-Rays and Type I Supernova Remnants. ApJ, 140:1309–1313, October 1964. doi: 10.1086/148028.

T. S. Wood, R. Hollerbach, and M. Lyutikov. Density-shear instability in electron magneto-hydrodynamics. *Physics of Plasmas*, 21(5):052110, May 2014. doi: 10.1063/1.4879810.

S. Zane, M. Cropper, R. Turolla, L. Zampieri, M. Chieregato, J. J. Drake, and A. Treves. XMM-Newton Detection of Pulsations and a Spectral Feature in the X-Ray Emission of the Isolated Neutron Star 1RXS J214303.7+065419/RBS 1774. ApJ, 627(1):397–403, July 2005. doi: 10.1086/430138.

Silvia Zane and Roberto Turolla. Unveiling the thermal and magnetic map of neutron star surfaces though their X-ray emission: method and light-curve analysis. MNRAS, 366(3):727–738, March 2006. doi: 10.1111/j.1365-2966.2005.09784.x.

Chapter 5

M. V. Beznogov, A. Y. Potekhin, and D. G. Yakovlev. Heat blanketing envelopes of neutron stars. Phys. Rep., 919:1–68, July 2021. doi: 10.1016/j.physrep.2021.03.004.

E. A. Chaikin, A. D. Kaminker, and D. G. Yakovlev. Afterburst thermal relaxation in neutron star crusts. Ap&SS, 363(10):209, October 2018. doi: 10.1007/s10509-018-3393-z.

Francesco Coti Zelati, Nanda Rea, José A. Pons, Sergio Campana, and Paolo Esposito. Systematic study of magnetar outbursts. MNRAS, 474(1):961–1017, February 2018. doi: 10.1093/mnras/stx2679.

Davide De Grandis, Roberto Turolla, Toby S. Wood, Silvia Zane, Roberto Taverna, and Konstantinos N. Gourgouliatos. Three-dimensional Modeling of the Magnetothermal Evolution of Neutron Stars: Method and Test Cases. ApJ, 903(1):40, November 2020. doi: 10.3847/1538-4357/abb6f9.

Davide De Grandis, Roberto Turolla, Roberto Taverna, Elisa Lucchetta, Toby S. Wood, and Silvia Zane. Three-Dimensional Magneto-Thermal Simulations of Magnetar Outbursts. 2022. Submitted to ApJ.

Konstantinos N. Gourgouliatos, Rainer Hollerbach, and Andrei P. Igoshev. Powering central compact objects with a tangled crustal magnetic field. MNRAS, 495(2):1692–1699, June 2020. doi: 10.1093/mnras/staa1295.

V. Karageorgopoulos, K. N. Gourgouliatos, and I. Contopoulos. Current closure through the neutron star crust. MNRAS, 487(3):3333–3341, 06 2019. doi: 10.1093/mnras/stz1507. URL https://doi.org/10.1093/mnras/stz1507.

S. K. Lander. Magnetar Field Evolution and Crustal Plasticity. ApJ, 824(2):L21, June 2016. doi: 10.3847/2041-8205/824/2/L21.

S. Mereghetti, V. Savchenko, D. Gotz, L. Ducci, C. Ferrigno, E. Bozzo, J. Borkowski, and A. Bazzano. SGR 1935+2154: INTEGRAL hard X-ray counterpart of radio burst. *GRB Coordinates Network*, 27668:1, April 2020.

M. C. Miller et al. PSR J0030+0451 Mass and Radius from NICER Data and Implications for the Properties of Neutron Star Matter. *ApJ Lett.*, 887(1):L24, 12 2019. doi: 10.3847/2041-8213/ab50c5.

J. A. Pons and N. Rea. Modeling Magnetar Outbursts: Flux Enhancements and the Connection with Short Bursts and Glitches. ApJ, 750(1):L6, May 2012. doi: 10.1088/2041-8205/750/1/L6.

A. Y. Potekhin, J. A. Pons, and D. Page. Neutron Stars–Cooling and Transport. *Space Science Reviews*, 191:239–291, October 2015.

Andrea Tiengo, Paolo Esposito, Sandro Mereghetti, Roberto Turolla, Luciano Nobili, Fabio Gastaldello, Diego Götz, Gian Luca Israel, Nanda Rea, Luigi Stella, Silvia Zane, and Giovanni F. Bignami. Nature, 500(7462):312–314, August 2013. doi: 10.1038/nature12386.

D. G. Yakovlev, A. D. Kaminker, A. Y. Potekhin, and P. Haensel. Model of heat diffusion in the outer crust of bursting neutron stars. MNRAS, 500(4):4491–4505, January 2021. doi: 10.1093/mnras/staa3547.

Appendix A

Francesco Coti Zelati, Nanda Rea, José A. Pons, Sergio Campana, and Paolo Esposito. Systematic study of magnetar outbursts. MNRAS, 474(1):961–1017, February 2018. doi: 10.1093/mnras/stx2679.

D. G. Yakovlev, A. D. Kaminker, O. Y. Gnedin, and P. Haensel. Neutrino emission from neutron stars. Phys. Rep., 354(1-2):1–155, November 2001. doi: 10.1016/S0370-1573(00)00131-9.

Appendix B

Z. Su and P. Coppens. Rotation of real spherical harmonics. *Acta Crystallographica Section A*, 50(5):636–643, Sep 1994. doi: 10.1107/S0108767394003077. URL https://doi.org/10.1107/S0108767394003077.

Appendix C

William H. Press, Saul A. Teukolsky, William T. Vetterling, and Brian P. Flannery. *Numerical recipes in FORTRAN. The art of scientific computing*. 1992.

Appendix D

D. N. Aguilera, J. A. Pons, and J. A. Miralles. 2D Cooling of magnetized neutron stars. A&A, 486(1):255–271, July 2008. doi: 10.1051/0004-6361:20078786.

S. Chandrasekhar and P. C. Kendall. On Force-Free Magnetic Fields. ApJ, 126:457, September 1957. doi: 10.1086/146413.

R. Lüst and A. Schlüter. Kraftfreie Magnetfelder. Mit 4 Textabbildungen. ZAp, 34:263, January 1954. (in German).